Dating of groundwater with Atom Trap Trace Analysis of ^{39}Ar

Florian Ritterbusch

Issued 2013

Dissertation

submitted to the

Combined Faculties of the Natural Sciences and Mathematics

of the Ruperto-Carola-University of Heidelberg, Germany

for the degree of

Doctor of Natural Sciences

Put forward by

Florian Ritterbusch

born in: Bielefeld, Germany

Oral examination: February 05, 2014

Dating of groundwater with Atom Trap Trace Analysis of ^{39}Ar

Referees: Prof. Dr. Markus K. Oberthaler
Prof. Dr. Norbert Frank

Zusammenfassung

Das Radioisotop ^{39}Ar, mit einer Halbwerszeit von 269 a, kann zur Datierung von Wasser und Eis im Zeitbereich von 50–1000 a, in dem keine andere verlässliche Datierungsmethode besteht, verwendet werden. Aufgrund seiner extrem kleinen Häufigkeit von nur $8.23 \cdot 10^{-16}$, kann ^{39}Ar derzeit nur durch Low-Level Counting (LLC) in dem Untergrundlabor der Universität Bern gemessen werden.

Atom Trap Trace Analysis (ATTA) ist eine atom-optische Methode die zur Analyse seltener Krypton-Isotope entwickelt wurde. Im Rahmen dieser Arbeit wurde eine ATTA-Apparatur zur Einzelatomdetektion von ^{39}Ar realisiert und angewendet auf die Datierung von Grundwasserproben.

Die ^{39}Ar-Kontamination in der Apparatur, welche von der Optimierung mit angereicherten Proben stammt, konnte mit Hilfe einer Probe bestimmt werden, deren Konzentration mit LLC auf $< 5\,\%$ modern gemessen wurde. Wird die resultierende Untergrundzählrate 0.38(18) atoms/h zur Korrektur verwendet, so ergibt sich eine atmosphärische ^{39}Ar-Zählrate von 3.22(21) atoms/h.

Basierend auf kontrollierten Mischungen von atmosphärischem Argon und einer Probe mit bekannter ^{39}Ar-Konzentration von 9(5) % modern konnte die Anwendung der vorgestellten Methode auf die Datierung von Wasser validiert werden. Das Alter einer Grundwasserprobe aus dem Schwetzinger Hardt in dem Oberen Rheingraben konnte daraufhin in Übereinstimmung mit der LLC-Messung auf 51(87) a bestimmt werden. Die Messung einer Grundwasserprobe aus dem Hessischen Ried mit bis dahin unbekannter ^{39}Ar-Konzentration ergab einen vom ^{39}Ar-Untergrund der Apparatur nicht zu unterscheidenden Wert. In Übereinstimmung mit den ergänzenden Isotopen-Daten, deutet dies auf ein Grundwasser hin, das älter als 830 a ist, welches das kontaminationsbedingte Datierungslimit darstellt.

Abstract

The radioisotope ^{39}Ar, with a half-life of 269 a, can be used for the dating of water and ice in the time range of 50–1000 a, in which no other reliable dating method exists. Due to its extremely small abundance of $8.23 \cdot 10^{-16}$, ^{39}Ar can currently only be measured by Low-Level Counting (LLC) in the underground laboratory at the university of Bern.

Atom Trap Trace Analysis (ATTA) is an atom optical technique that has been developed for the analysis of rare krypton isotopes. In the course of this thesis, an apparatus for Atom Trap Trace Analsis of ^{39}Ar has been realized and applied for the dating of groundwater samples.

The ^{39}Ar contamination in the apparatus, which originates from optimization with enriched samples, could be determined with a sample whose ^{39}Ar concentration was measured to be $< 5\,\%$ modern by LLC. If the resulting ^{39}Ar background count rate

of 0.38(18) atoms/h is used for correction, the apparatus achieves an atmospheric ^{39}Ar count rate of 3.22(21) atoms/h.

Based on controlled mixtures of atmospheric argon and an argon sample with a known ^{39}Ar concentration of 9(5) % modern, the application of the presented system to the dating of water could be validated. The age of a groundwater sample from the Schwetzinger Hardt in the Upper Rhine Graben was measured to be 51(87) a in agreement with the LLC measurement. The measurement of a groundwater sample from the Hessian Ried with so far unknown ^{39}Ar concentration yielded a value undistinguishable from the contamination. In agreement with the complementary isotope data this indicates that the groundwater is older than 830 a, which is the dating limit given by the contamination.

Contents

1 Preface

When the crew of the Apollo 8 mission became the first humans to see the earth from space on the 24th of December in 1968, they had to use a special color film to catch the bright blue of the earth when taking the famous *earthrise* picture. The blue color originates from reflection of the oceans which cover 71 % of the earth's surface. While the oceans are formed by 97 % of the earth's water, only 3 % is freshwater of which almost 70 % is contained in ice caps and glaciers. Surface waters, such as lakes and rivers, only constitute less than one percent of the global freshwater, leaving groundwater with 30 % as the world's largest freshwater resource.

Only a small fraction of about 10 % of the freshwater is consumed directly for drinking and cooking. Already twice as much is used for industrial purposes, but with about 70 % by far the largest fraction is used for crop production on irrigated land [1]. Therefore, groundwater and moreover the understanding of groundwater systems is of essential importance for global water and food security.

Due to human misuse, global groundwater resources are substantially subject to depletion, salination or pollution [2]. This is especially the case for shallow groundwater systems, where the water typically has a residence time on the order of only a few years up to a few decades. The groundwater is therefore directly influenced by modern human activities, such as agriculture or industry.

As a consequence, deeper lying aquifers that transport old groundwater are of steadily increasing interest. In order to study these aquifer systems, the *age* of the water, i. e. the time between sampling and last contact with the atmosphere, provides crucial hydrological information about the groundwater system, such as origin, flow patterns or recharge rates. The ability to date water is therefore essential for groundwater management.

Apart from groundwater, information about the water age is equally important for other hydrologic systems such as oceans or glaciers. It would for example provide missing information in the understanding of circulation and mixing processes in the oceans, which are important to model the CO_2 uptake of the oceans in the context of climate change. Moreover, the age of a sample can provide the essential time information for climate records that are derived from glacier ice or groundwater.

A key role in the dating of water or ice is played by radioisotopes, which act as a chronometer by their natural radioactive decay. The time range for which a radioisotope can be applied is determined by its half-life, such that the ability to date a water sample in a given time range depends on the availability of a suitable radioisotope.

In order to date water with an age between 50–1000 a, ^{39}Ar with a half-life of 269 a is practically the only radioisotope which covers this time range. Apart from being the only radioisotope bridging the dating window, it has many other features making it an ideal environmental tracer, such as its chemical inertness or its cosmogenic origin.

However, its routine analysis in water samples is hampered by its extremely small abundance of $8.23 \cdot 10^{-16}$, which corresponds to about 8500 ^{39}Ar atoms in a liter of water. It is a common practice to stress this unimaginable number with analogies, that make it more conceivable. $8.23 \cdot 10^{-16}$ for example corresponds to

- a black corn of rice in a convoy of trucks stretching once around the earth, each loaded with 40 t of rice [3]
- the size of an amoeba compared to the size of the institute for environmental physics in Heidelberg [4]
- a Euro-cent in the USA government debts of 16 billion dollars in the year 2012 [5] .

A different quality of the extreme ^{39}Ar abundance becomes apparent in the following consideration: In the course of this project, enriched ^{39}Ar samples had to be used in order to measure the spectroscopic lines of ^{39}Ar. As little as 10 nl of argon with an ^{39}Ar abundance of around 50 % are still stored in vacuum containers in the laboratory. If that argon gas was released, the ^{39}Ar concentration in the entire physics institute would be increased by a factor of 10.

Due to the extreme rareness, ^{39}Ar has so far been routinely accessible only by Low-Level Counting (LLC) in the underground laboratory in Bern requiring a sample size of several tons of water and a measuring time of several weeks. These requirements limit the routine applicability of ^{39}Ar dating with LLC to groundwater, where degassing several tons of water from a well is typically feasible [6].

Atom Trap Trace Analysis is an atom optical technique that has been developed for rare krypton isotopes in the past decade and is now available for routine analysis [7]. The method employs the high selectivity of atomic transitions in order to distinguish the desired rare isotope from the abundant isotopes. Since it is not bound to radioactivity, it allows for a fast analysis while requiring only comparatively small sample sizes independent of the isotope's half-life.

The applicability of ATTA to ^{39}Ar has been demonstrated in a proof of principle experiment [8]. However, the achieved ^{39}Ar count rate did not allow for the dating of groundwater. The implementation of ATTA for ^{39}Ar to a level which allows the dating of water is the subject of this thesis.

2 Fundamentals

Concepts from atom optics and environmental physics form the base for dating of water with ^{39}Ar-ATTA. These concepts are briefly outlined in this chapter, whereby the main focus is placed on recent developments and features that have not been treated so far.

2.1 Dating of water with radioisotopes

The *age* of a water sample, i. e. the time between sampling and last contact with the atmosphere, can be determined by measuring the isotopic composition of the gases suspended in the water. Especially radioactive isotopes [9] can be used as a chronometer by measuring their number which after the time t has decayed from the initial amount N_0 to

$$N(t) = N_0 \cdot e^{-t/\tau} \tag{2.1}$$

where τ denotes the mean lifetime, which is related to the half-life $T_{1/2}$ by

$$\tau = \frac{T_{1/2}}{\ln(2)} \ . \tag{2.2}$$

If the inital number N_0 of a radioisotope in a water sample at its last contact with the atmosphere is known, the age t of a water sample can be determined by measuring its present number $N(t)$ from

$$t = \tau \cdot \ln \left[\frac{N_0}{N(t)} \right] \ . \tag{2.3}$$

The time range for which a radioisotope can be employed can roughly be estimated by the empirical rule of thumb $\frac{1}{5}T_{1/2}...5T_{1/2}$, leading to the dating ranges plotted in figure 2.1.

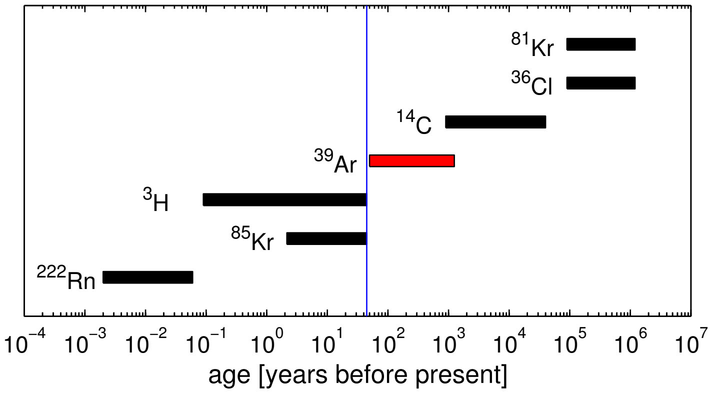

isotope	half-life
^{222}Rn	3.824 d
^{3}H	12.32 a
^{85}Kr	10.76 a
^{39}Ar	269 a
^{14}C	5730 a
^{81}Kr	232 ka
^{36}Cl	301 ka

Figure 2.1: Dating ranges for radioactive isotopes commonly employed for dating water (left) defined by the corresponding half-lives (right) (adapted from [10]).

The atmospheric concentrations of tritium and ^{85}Kr, that have half-lives of 12.32 a and 10.76 a respectively, are almost entirely anthropogenic. The tritium content in the atmosphere mainly originates from nuclear bomb tests that were carried out from 1945 until 1963, when the *limited test ban treaty* was signed. In that year, the tritium concentration shows a pronounced maximum known as the *bomb peak* (figure 2.2) which is almost three orders of magnitude higher than the present value of ~10 TU [11].

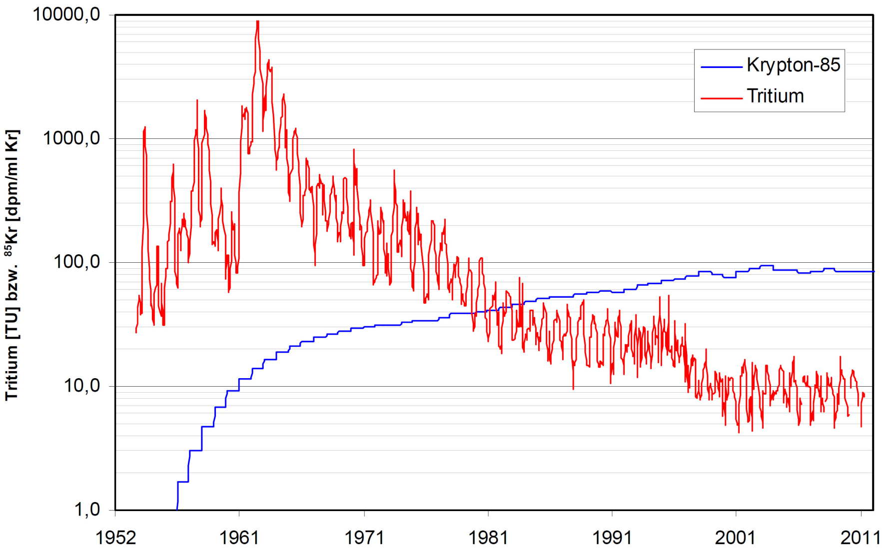

Figure 2.2: Concentration of tritium and ^{85}Kr in the atmosphere for the last 60 years. Tritium exhibits a pronounced peak in 1963 followed by a decline, while ^{85}Kr steadily increases (taken from [12]).

The ^{85}Kr concentration in the atmosphere is not limited to the bomb test era but steadily increases due to nuclear activities, such as nuclear fuel reprocessing. The present concentration is about six orders of magnitude higher than the natural abundance [13, 14, 15].

Tritium and ^{85}Kr are commonly employed for identifying young waters with an age up to ∼50 a. Due to their comparatively short half-life, they can routinely be measured by decay counting. The dating applications performed in the scope of this thesis involve tritium as an indicator for young water components.

For very old waters going up to an age of one million years, ^{81}Kr and ^{36}Cl with half-lives of 232 ka and 301 ka respectively can be employed [16, 17]. Due to their rareness and long half-life, decay counting is not feasible for these isotopes. ^{36}Cl is measured by accelerator mass spectrometry [18] while ^{81}Kr can since recently be routinely analyzed with Atom Trap Trace Analysis [7].

With a half-life of 5730 a, ^{14}C covers the time range of about 1000–40 000 a for dating of water [19]. The interpretation of ^{14}C concentrations in water samples is in general very complex, since ^{14}C is involved in a number of hydrogeochemical processes as for example the washing out of geologically old carbonates, altering the ^{14}C concentration. Nevertheless, ^{14}C is routinely measured in groundwater studies and also for the water samples investigated in this work it is employed as a monitor for old water components.

The dating gap at 50–1000 a between ^{3}H/^{85}Kr and ^{14}C is bridged by ^{39}Ar which has a half-life of 269 a. As for ^{81}Kr its atmospheric abundance is of merely cosmogenic origin and as a noble gas it is a conservative tracer not involved in hydrogeochemical processes. Although being an ideal tracer in many respects, its routine application in environmental sciences is hindered by its extremely small atmospheric abundance of $^{39}\mathrm{Ar}/\mathrm{Ar}\sim 10^{-15}$. So far, it has been routinely accessible only by Low-Level Counting (LLC) in the underground laboratory in Bern, requiring a sample size of several tons of water and a measuring time of several weeks [20], practically restricting its application to groundwater. The realization of ATTA for ^{39}Ar presented in this work aims at measuring ^{39}Ar within a day in samples of ∼1 l water and ∼1 kg of ice, which would allow for routine dating of ocean water and glacier ice.

2.2 Argon

Besides being color- and odorless, argon is a very inert noble gas, which gave rise to its name deduced from the greek word *argos* meaning *lazy* or *indolent*. It was discovered in 1894 by Lord Rayleigh and Sir William Ramsay for which the former earned the Nobel Prize for physics in 1904 [21].

Table 2.1 compiles all 24 known isotopes of argon, most of which are unstable with a half-life below 2h. Only ^{39}Ar, ^{42}Ar and ^{37}Ar have longer half-lives of 269 a, 33 a and 35 d respectively. The stable isotopes are ^{40}Ar, ^{38}Ar and ^{36}Ar, although the latter is theoretically unstable and should decay to ^{36}S by $\beta^+\beta^+$-decay, but no evidence for this decay has been observed so far. Argon is the third most common gas in the earth's atmosphere constituting 0.934 % by volume and 1.28 % by mass. With 99.6 % abundance ^{40}Ar is the prevailing argon isotope in the atmosphere. It originates from the decay of ^{40}K, which naturally occurs in the earth's crust and mantle, by electron capture or positron emission. This decay forms the base of the widespread potassium-argon dating of rocks.

Table 2.1: Compilation of argon isotopes. The isotopes relevant for dating with ^{39}Ar-ATTA are highlighted in red. Data taken from [22].

Isotope	Mass [m_u]	Nat. ab.	Nucl. spin I	$T_{1/2}$	Main decay
^{30}Ar	30.022	–	0	<20 ns	p to ^{29}Cl
^{31}Ar	31.012	–	5/2	14.4(6) ms	β^+,p to ^{30}S
^{32}Ar	31.998	–	0	98(2) ms	ec to ^{32}Cl
^{33}Ar	32.990	–	1/2	173.0(20) ms	β^+ to ^{32}Cl
^{34}Ar	33.980	–	0	844.5(34) ms	β^+ to ^{34}Cl
^{35}Ar	34.975	–	3/2	1.77 s	β^+ to ^{35}Cl
^{36}Ar	35.968	0.003365(30)	0	–	–
^{37}Ar	36.967	–	3/2	35.0 d	EC to ^{37}Cl
^{38}Ar	37.963	0.000632(5)	0	–	–
^{39}Ar	38.962	$8.23 \cdot 10^{-16}$	7/2	268 a	β^- to ^{39}K
^{40}Ar	39.962	0.996003(30)	0	–	–
^{41}Ar	40.965	–	7/2	1.82 h	β^- to ^{41}K
^{42}Ar	41.965	$< 6 \cdot 10^{-21}$	0	33 a	β^- to ^{42}K
^{43}Ar	42.966	–	–	5.4 min	β^- to ^{43}K
^{44}Ar	43.964	–	0	11.87 min	β^- to ^{44}K
^{45}Ar	44.968	–	0	21.48 s	β^- to ^{45}K
^{46}Ar	45.968	–	0	8.4 s	β^- to ^{46}K
^{47}Ar	46.972	–	3/2	1.23 s	β^- to ^{47}K
^{48}Ar	47.975	–	0	0.48 s	β^- to ^{48}K
^{49}Ar	48.981	–	3/2	170 ms	β^- to ^{49}K
^{50}Ar	49.984	–	0	85 ms	β^- to ^{50}K
^{51}Ar	50.992	–	3/2	60 ms	β^- to ^{51}K
^{52}Ar	51.997	–	0	10 ms	β^- to ^{52}K
^{53}Ar	53.005	–	–	3 ms	β^- to ^{53}K

^{36}Ar and ^{38}Ar consitute only a tiny fraction of the argon in the atmosphere with 0.34 % and 0.06 % respectively. However, the primordial argon as for example found in the sun almost exclusively consists of ^{36}Ar and ^{38}Ar, with a ratio of about 5.7:1. The presence of ^{40}Ar in the atmosphere of planets is therefore an indicator for crustal potassium [23]. The argon fraction in the atmosphere of Mars for example amounts to 1.9 % with ^{40}Ar being 1000 times more abundant than ^{36}Ar [24], whereas in the atmosphere of Venus ^{40}Ar and ^{36}Ar contribute equally to a total argon fraction of 70 ppm [25].

^{40}Ar/^{36}Ar ratios differing from the atmospheric value of 295.5 are also encountered in the lithosphere. Argon from the upper mantle can exhibit high ^{40}Ar/^{36}Ar ratios of more than 40 000 [26, 27]. As will be discussed later, the ^{39}Ar content in the upper mantle is expected to be much lower than the atmospheric value. The ^{40}Ar/^{36}Ar ratio can therefore help to identify sources of ^{39}Ar free samples.

In table 2.2 some properties of argon are compiled, which are relevant for the following considerations. Important for dating of groundwater is especially the solubility of argon in water which depends on temperature, salinity and pressure [28]. The solubility for freshwater at 10 °C, which is a typical groundwater temperature, and the solubility for typical deep sea water with a salinity of 34 ‰ at 0 °C is almost the same, amounting to about 0.4 $\mathrm{ml}_{\mathrm{argon}}/\mathrm{l}_{\mathrm{water}}$.

Table 2.2: Some properties of argon relevant for the following sections.

density at STP	1.784 g/l
liquid density	1.4 g/cm^3
melting point	83.81 K
solubility at 10 °C, no salinity, 1 bar	0.3861 $\mathrm{ml}_{\mathrm{argon}}/\mathrm{l}_{\mathrm{water}}$
solubility at 0 °C, 34 ‰ salinity, 1 bar	0.3937 $\mathrm{ml}_{\mathrm{argon}}/\mathrm{l}_{\mathrm{water}}$

2.3 Argon 39

The discovery of ^{39}Ar was first reported in 1950 in potassium salts after bombardments in nuclear reactors [29]. The atmospheric ^{39}Ar content is dominated by the spallation [30]

$$^{40}\mathrm{Ar(n,2n)}^{39}\mathrm{Ar} \tag{2.4}$$

occuring in the stratosphere through cosmic ray derived neutrons above the threshold energy of 10.1 MeV. For a possible contribution due to human activities such as bomb tests or nuclear industry, an upper limit of 5 % could be set by comparing pre-nuclear and modern samples [30]. Based on ^{14}C variations in tree rings over the last 1000 a, an upper bound of 7 % for variations in the atmospheric ^{39}Ar concentration could be estimated [31]. Apparently, the cosmic ray flux responsible for the production of ^{39}Ar did not change significantly during this time span.

In the subsurface, ^{39}Ar can be produced due to the decay of ^{39}K, which is abundant in the crustal bulk. In [32] it is calculated, that in a depth less than 2000 m.w.e.[1] the decay of ^{39}K to ^{39}Ar induced by stopped muon capture, i. e.

$$^{39}\mathrm{K}(\mu^-,\nu)^{39}\mathrm{Ar} \tag{2.5}$$

should be dominating. At greater depth, the muon flux is strongly reduced and the

$$^{39}\mathrm{K(n,p)}^{39}\mathrm{Ar} \tag{2.6}$$

---

[1] m.w.e. = meter water equivalent

reaction due to neutrons from primordial uranium and thorium dominates the ^{39}Ar production. For groundwater dating, which is typically working with aquifers not deeper than 2000 m.w.e., this implies that the $^{39}\mathrm{K}(\mu^-,\nu)^{39}$Ar reaction should be the prevalent production mechanism leading to an unwanted ^{39}Ar background. However, in granites with high uranium and thorium content where a high neutron flux is present, the $^{39}\mathrm{K}(n,p)^{39}$Ar process was measured to be the predominant ^{39}Ar production process. Groundwater sampled in the Stripa granite in Sweden, which exhibits an exceptionally high uranium and thorium content, showed ^{39}Ar concentrations up to 17 times larger than the atmospheric value [33].

In general, the amount of underground ^{39}Ar dispersed in groundwater depends on the abundance of potassium, the radioactivity and on the probability of argon to diffuse out of the rock into the water. These parameters vary from location to location and need to be analyzed individually for dating groundwater with ^{39}Ar, for example by monitoring ^{37}Ar as a measure for the neutron activity in the ground [34]. However, ^{39}Ar background is not a concern for dating ocean water.

The nucleogenic ^{39}Ar production in the subsurface undesired in groundwater studies can actually be exploited as a chronometer for fluid-rock interactions [35] as has been demonstrated in geothermal features at the Yellowstone National Park [36]. A further study involving the ^{39}K(n,p)^{39}Ar reaction aims at reconstructing the neutron dose the survivors of the atomic bombs in Hiroshima and Nagasaki were exposed to [37]. There, the ^{39}Ar content measured in samples taken from granite gravestones provided a measure for the fast neutron flux. These developments show that the use of ^{39}Ar is not restricted to groundwater studies.

The specific activity of atmospheric ^{39}Ar was measured in the underground laboratory in Bern with LLC to be [6]

$$0.107(4)\,\mathrm{dpm/l} \qquad \text{(liter argon gas STP)}\ . \tag{2.7}$$

A later measurement with a prototype detector for Dark Matter searches with liquid argon as a target yielded a value of [38]

$$1.01 \pm 0.02(\mathrm{stat}) \pm 0.08(\mathrm{syst})\mathrm{Bq/kg} \qquad \text{(kg argon)} \tag{2.8}$$

which is in very good agreement with the previously measured value. The half-life of ^{39}Ar was measured in Brookhaven by measuring its mass and activity ratio relative to ^{37}Ar in enriched samples [39]. The half-life of ^{37}Ar could be determined to 35 days by directly following its decay curve. These two pieces of information yield a half-life for ^{39}Ar of

$$T_{1/2} = 269(3)\,\mathrm{a} \tag{2.9}$$

which corresponds to a mean lifetime of $\tau = \frac{T_{1/2}}{\log(2)} = 388(4)\,\mathrm{a}$. Together with the specific activity, this yields ∼22 million ^{39}Ar atoms in a litre of atmospheric argon, corresponding to a number ratio of

$$\frac{N(^{39}\mathrm{Ar})}{N(\mathrm{Ar})} = 8.23(32) \cdot 10^{-16} \tag{2.10}$$

The mass ratio is slightly lower with

$$\frac{m_{\text{atmo}}(^{39}\text{Ar})}{m_{\text{atmo}}(\text{Ar})} = 8.03(31) \cdot 10^{-16} \ . \tag{2.11}$$

In the following, the number ratio will exclusively be used.

From the foregoing values the number of ^{39}Ar atoms in modern air, water and ice is obtained to

	number of ^{39}Ar atoms
1 l argon	$21.8 \cdot 10^6$
1 l air	200 000
1 l of water[2]	8730
1 kg of ice	$\sim$ 20 000

The argon content in natural ice is mainly concentrated in air bubbles, that have been entrapped during the transformation of snow into ice. About 0.1 l of gas per kg of ice with a composition close to atmospheric is expected [40]. The argon dissolved in water diffuses out of the matrix during formation of ice crystals and can only remain in the ice in an enclosed system, if for example a bulk of water is frozen. In this case less than 0.03 l of gas and correspondingly less than 6500 ^{39}Ar atoms per kg of ice are expected.

2.4 Detection of ^{39}Ar

The properties exploited by present detection methods to distinguish ^{39}Ar from other isotopes are its

- radioactivity
- mass
- atomic spectrum.

Since all other radioactive argon isotopes occur in negligible concentrations or with different decay modes, the radioactivity is an unambiguos feature of ^{39}Ar. It decays without γ- emission to ^{39}K through the reaction

$$^{39}\text{Ar} \rightarrow {}^{39}\text{K} + e^- + \bar{\nu}_e \tag{2.12}$$

emitting electrons with the energy spectrum shown in figure 2.3 that has a cut-off energy of 565 keV [29].

---

[2] for freshwater with 10 °C or saltwater STP with 34 ‰ salinity as given in table 2.2

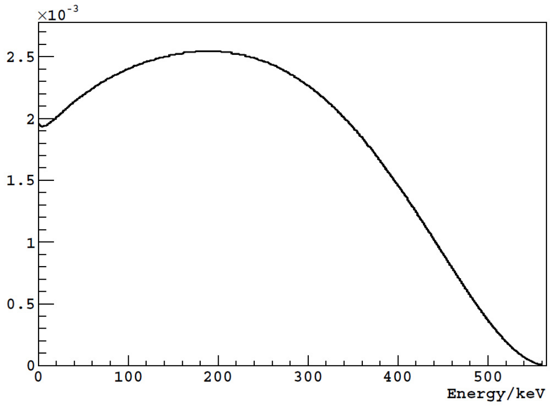

Figure 2.3: Beta spectrum of ^{39}Ar with an endpoint energy of 565 keV, from [41].

Detecting the emitted electrons from the ^{39}Ar decay and distinguishing them by their energy spectrum from background decay forms the base of Low-Level Counting (LLC) and liquid-scintillation counting.

Low-Level Counting (LLC)

Apart from a few exceptions, almost all ^{39}Ar-measurements so far were conducted in the LLC-underground laboratory in Bern, which is in routine operation since the seventies [42]. The argon extracted from groundwater is compressed into proportional gas counters in which the argon itself serves as the counting gas which is ionized by incident radiation. The produced ion-electron pairs are separated by an electric field between a thin anode wire in the center and the outer cathode. The electrons impinging on the anode wire and the ions impinging on the cathode are detected as a current (figure 2.4).

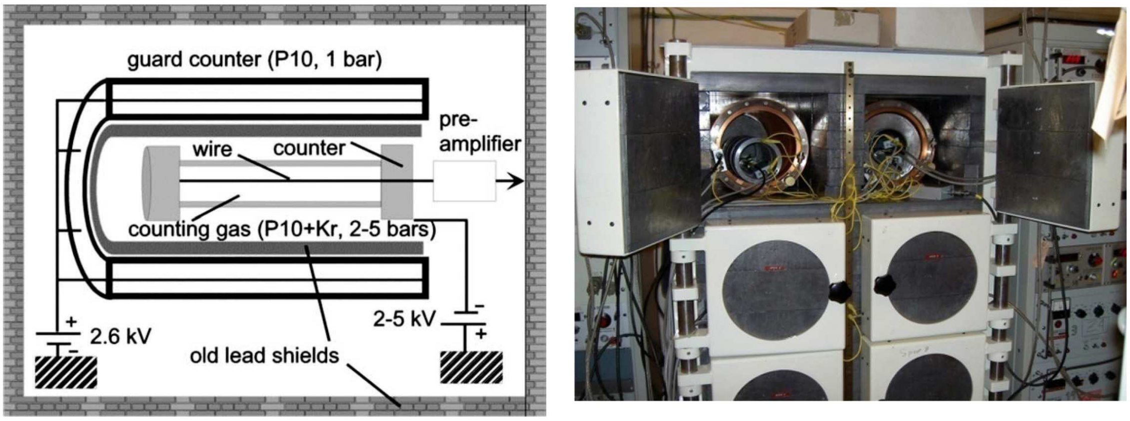

Figure 2.4: Schematic of the shielded gas proportional counter used for LLC-measurements in Bern (left, from [20]) and a real image of two counters enclosed in the lead chamber.

The number of ion-electron pairs is proportional to the energy of the incident particle, which is important for discriminating radioactive background events. An admixture of 5–10 % methane serves as a quench gas, which ensures that a pulse discharge terminates. The main difficulty in measuring the activity of ^{39}Ar lies in discriminating the large background due to cosmic rays and intrinsic radioactivity of the materials used for constructing the counting facility. Because of this, the counters are located 35 m below the surface, shielded with ^{210}Pb-depleted lead from old shipwrecks in a room constructed with special low-activity concrete, to list just a few measures that have been taken to reduce the background [43]. A background between 0.02 cpm and 0.03 cpm(=counts per minute) has been achieved as opposed to the aforementioned specific activity of ^{39}Ar of 0.1 dpm/l. This specific activity corresponds to ~6 decays in one hour for 1 l of argon gas, which is contained in about 100 l of air, 3.2 tons of water or 100 kg of ice. In practice, the amount of required argon for LLC lies between 0.5 l and 2 l and the counting time between 8 d and 60 d [20]. Especially for old waters, huge water quantities and long counting times of several weeks are necessary to statistically overcome the remaining background.

This mainly limits the applicability of ^{39}Ar dating with LLC to groundwaters, where degassing several tons of water from a well is typically feasible. However, studies have even been conducted for ice from Greenland, Antarctica and Devon Island between 1969 and 1974 where ^{39}Ar ages were compared to ages obtained from δ^{18}O [6]. Applications to ocean water have been performed in the past as long as large ocean water samples were routinely collected for ^{14}C analysis with LLC [6, 44, 45]. With the advent of AMS for ^{14}C analysis requiring only 1 l samples, oceanographic ^{39}Ar measurements practically ceased.

Accelerator Mass Spectrometry (AMS)

The efforts for measuring ^{39}Ar with AMS were undertaken at the accelerator facilitiy ATLAS at the Argonne National Laboratories near Chicago during the past two decades. Contrary to ^{14}C, for which AMS has become the standard method, mass spectrometry is not easily applied to noble gases, for they do not form negative ions. Due to this, an electron cyclotron resonance (ECR) positive ion source is employed [46].

In this source electrons are produced in a RF-plasma of a support gas confined by a defined magnetic field configuration, that together with the RF frequency fulfills the ECR condition. Due to the resonance, the electrons build up enough kinetic energy to ionize the sample gas to highly charged states, such as ^{40}Ar^{8+} and ^{39}Ar^{8+} in the case of argon.

The ion beam is accelerated by linear accelerators and transported to a magnetic spectrograph that spatially separates the ions according to their momentum/charge ratio. Since the ions do not have a single and unique but a distribution of charge states, ^{39}Ar would not be separated from its isobars of which ^{39}K is the most interfering one, due to the magnetic field alone. The magnetic spectrograph is therefore filled with a gas (5 Torr nitrogen) which effects, that the ions follow the trajectory given by the ion's mean charge, which in turn depends on the atomic number [47]. The separated and focused ion beams are subsequently detected in the focal plane with a position sensitive detector yielding data as shown in figure 2.5.

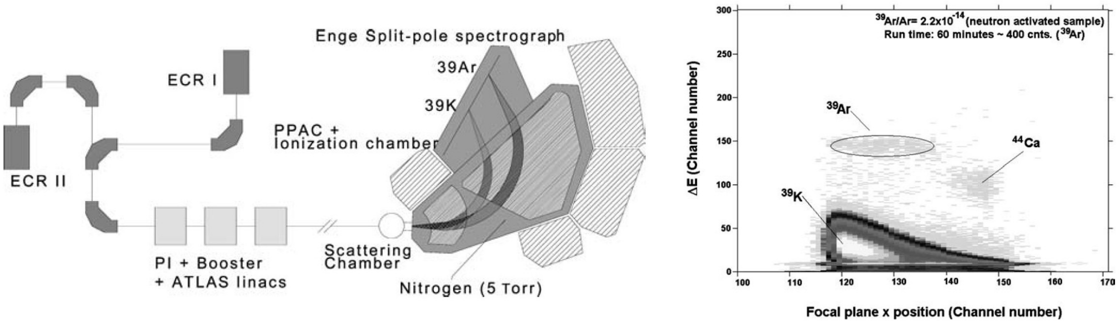

Figure 2.5: Schematic of the AMS facility for detecting ^{39}Ar (left) and a typical detection signal (right). For low ^{39}Ar concentrations the background due to ^{39}K corrupts the ^{39}Ar signal (from [20]).

First measurements for ^{39}Ar could be performed in the early nineties for enriched samples down to the natural abundance level [46]. By increasing the argon ion flux from the ECR source and reducing the ^{39}K contamination, a detection limit of $4.3 \cdot 10^{-17}$ for the ^{39}Ar concentration could be reached one decade later [48]. This allowed for the measurement of ocean samples from the South Atlantic with measuring times of 5–10 h for one sample at a consumption of ~1–2 ml argon gas per measurement, corresponding to not more than 20 l of water. The corresponding ^{39}Ar count rate was around 8 atoms/h at the natural level.

Especially the search for ^{39}Ar-free argon for dark matter detectors based on liquid argon reinforced the effort to further increase the sensitivity of the ^{39}Ar measurement below $4.3 \cdot 10^{-17}$. The main difficulty laid in the discrimination of the interfering stable isobar ^{39}K, which was mainly produced in the ECR-source due to plasma operation. Although many efforts including the use of ultra pure materials and precision cleaning of the critical components have been made, the ^{39}K background could not be reduced to a level which would have allowed a higher sensitivity for ^{39}Ar. Further measures for reducing the ^{39}K background and increasing the source output are proposed but [49] "*This development is however non-trivial and will require extensive research at an off-line ECR source not currently available at ATLAS*".

Although the sensitivity could not be increased, the reported sensitivity of $4.3 \cdot 10^{-17}$ reached so far together with a small sample size of 20 l and the comparatively short measuring time of not more than 10 h implies that AMS exhibits the best performance for ^{39}Ar measurements so far. Probably because access to the heavily scheduled accelerator facility is limited and costly, no routine ^{39}Ar measurements are performed with AMS yet.

Liquid argon scintillation

^{39}Ar has also been measured in the context of detecting a weakly interacting massive particle (WIMP), a candidate for dark matter, one of the most troubling issues in fundamental physics. The WIMP has to be an elementary particle that interacts only through the weak force and gravity. It could therefore not be seen directly and would hardly interact with normal matter. In this sense it is similar to a neutrino but much more massive (10-1000 times heavier than a proton) and therefore slower. One option to find evidence of its existence is indirect by detecting its annihilation products, which can be neutrinos or γ-rays. Direct detection involves its collision with ordinary nuclei and the detection of the recoil of the target nuclei.

Liquid argon has advantageous properties as a scintillation medium for detecting such recoils, expected to be between 10–100 keV [41]. In the context of the WARP (WIMP Argon Programme) collaboration, such a detector based on liquid argon scintillation has been developed. A prototype detector for WIMP detection was implemented with 2.3 l of liquid argon with atmospheric composition and operated for more than two years at the Laboratori Nazionali del Gran Sasso, Italy [50]. As a by-product the specific activity of ^{39}Ar could be measured, as described earlier.

The expected rates for the detection of a WIMP are as low as a few events per ton of target per year. The β decay of ^{39}Ar at the natural level represents a dramatic background due to its specific activity of ~1 Bq/kg of atmospheric argon. This is 10 orders of magnitude higher than the expected rate of WIMP induced recoils which exceeds the selectivity of the liquid argon detector for separating recoils from β and γ events. The ^{39}Ar content limits the size of the liquid argon detector, since the number of β events increases with the amount of argon, which should be high for the WIMP detection rate.

Therefore, a major search for argon depleted in ^{39}Ar has been undertaken [51]. The ^{39}Ar content of the investigated wells was analyzed by LLC in Bern [52]. Since ^{39}Ar concentrations below 5 % can not be measured with LLC, alternative options were pursued, one of them being AMS as discussed above. Since AMS could not reach a sensitivity below 5 % either, a dedicated scintillation detector with 0.56 kg liquid argon was built [51, 41]. With this detector an upper limit of $5.3 \cdot 10^{-18}$ for the ^{39}Ar concentration of underground argon from the Kinder Morgan CO_2 plant in Cortez, Colorado could be measured. Besides demonstrating the highest sensitivity for ^{39}Ar so far, a suitable source for ^{39}Ar-depleted argon was found. In consequence, a large scale production of argon from the well gas was launched with a rate of 0.5 kg/day [53, 54] for the *DarkSide-50* detector, that will operate with 50 l of liquid argon.

Of course, detecting ^{39}Ar with liquid scintillation counting for dating water is neither intended nor feasible due to the enormous amounts of argon needed. The increase in sensitivity with respect to LLC is predominantly the result of the much higher amount of argon.

Atom Trap Trace Analysis (ATTA)

The main difficulty for LLC and AMS, to distinguish ^{39}Ar from other isotopes, is almost entirely resolved when the atomic spectrum of ^{39}Ar is employed for identification. The probability that a photon resonant with ^{39}Ar is scattered by ^{40}Ar relative to the probability to be scattered by ^{39}Ar can be approximated by

$$\frac{\Gamma^2}{4\Delta f^2} \approx \frac{1}{30\,000} \tag{2.13}$$

where $\Gamma = 5.87\,\mathrm{MHz}$ denotes the natural linewidth of the atomic transition of ^{39}Ar and $\Delta f = 492.2\,\mathrm{MHz}$ the frequency difference of the corresponding transition in ^{40}Ar. This small number becomes very big when multiplied with the isotopic ratio

$$\frac{\Gamma^2}{4\Delta f^2} \cdot \frac{^{40}\mathrm{Ar}}{^{39}\mathrm{Ar}} \approx 4 \cdot 10^{10} \tag{2.14}$$

i. e. with the scattering probability for one photon ^{39}Ar can not be distinguished from ^{40}Ar. However, the relative probability that N photons are successively scattered by ^{40}Ar

$$\left(\frac{\Gamma^2}{4\Delta f^2}\right)^N \cdot \frac{^{40}\mathrm{Ar}}{^{39}\mathrm{Ar}} \tag{2.15}$$

becomes smaller than one percent already for ten photons. In a magneto-optical trap (MOT) an atom typically scatters around one million photons corresponding to a probability next to zero to mistake an ^{40}Ar with an ^{39}Ar atom. The probability becomes even lower for other elements whose atomic transitions are typically several nanometers away, i. e. Δf is on the order of THz.

Making use of this extreme selectivity by capturing the desired atom in a MOT and detecting its scattered photons is the main ingredient of Atom Trap Trace Analysis. This method was developed for rare krypton isotopes at the Argonne National Laboratories by Lu et al. with the first report in 1999 [55], where the detection of ^{85}Kr and ^{81}Kr at the natural abundance level with a magneto-optical trap was proven. Subsequent improvements led to the first application in hydrology in 2004, where one million year old groundwater could be dated in the Sahara [56]. ATTA is now available for the routine analysis of rare krypton isotopes, requiring a sample size of 5–10 µl krypton gas, which can be extracted from approximately 100–200 kg of water or 40–80 kg of ice [7]. The count rates for ^{85}Kr and ^{81}Kr are ∼20 000 and ∼1000 atoms/h respectively, leading to a net measuring time for one sample of 2–3 h. The sample size is limited by cross-sample contamination, which is still present even after a 36 h cleaning procedure between two successive measurements.

The applicability of ATTA to ^{39}Ar has been demonstrated in a proof of principle experiment [8], where twelve ^{39}Ar atoms were detected in 60 h in an atmospheric sample corresponding to a count rate of 0.22 atoms/h. The implementation of ATTA for ^{39}Ar to a level, which allows for the dating of water is the subject of this thesis.

Efforts have also been made to implement ATTA for ^{41}Ca for the purpose of dating bones and the analysis of osteoporosis [57, 58], but the necessary sensitivity of at least 10^{-14} could not be reached and according to present knowledge no further efforts are currently undertaken.

A group at the institute for peace research and security policy in Hamburg is currently developing an ATTA setup for ^{85}Kr analysis for the verification of the non-proliferation treaty [59].

Another ATTA experiment for krypton has been set up at Columbia University, New York for determining the krypton content at the ppt-level in xenon used for liquid xenon dark matter detectors [60].

According to current knowledge the fifth ATTA-group in the world is located at the Hefei national laboratory in China, where an apparatus for krypton has been set up [61].

2.5 Atomic transition spectrum of argon

As pointed out, the key ingredient for ATTA is the difference in the atomic spectrum between ^{39}Ar and the abundant argon isotopes[3]. The atomic spectrum of argon is best described with the Racah- or *jl*-coupling [62], due to its noble gas nature. The following spectroscopical considerations build on the notation and explanations given in [63], where also the Paschen-Notation, that will be mainly used, is introduced. The energy levels and the relevant transitions of ^{40}Ar are sketched in figure 2.6.

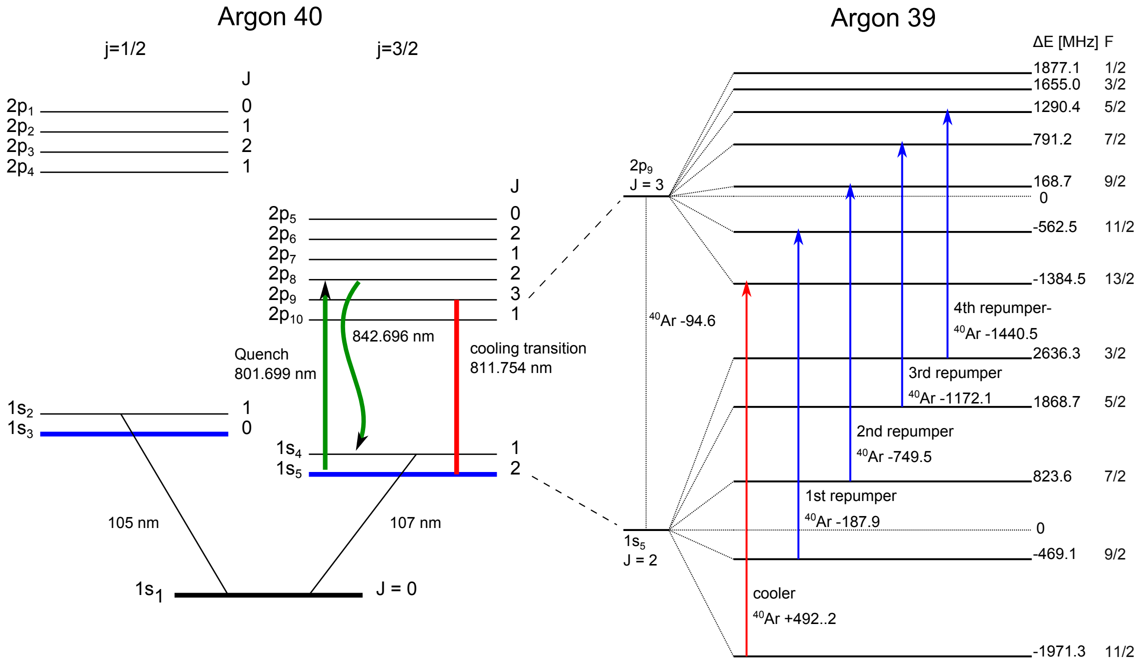

Figure 2.6: Energy spectrum of ^{40}Ar (left) and ^{39}Ar (right) with the relevant transitions (adapted from [5]).

---

[3] In the following ^{40}Ar will stand as a representative for all stable argon isotopes ^{40}Ar, ^{36}Ar and ^{38}Ar.

The energy levels are grouped according to the total angular momentum $j = L+S$ of the body. The 107 nm and 105 nm transitions from the ground state are in the XUV-range, for which neither lasers nor optics are standardly available, apart from the fact that it is absorbed by air and would have to be operated in vacuum. However, there is a cycling transition from the metastable state $1s_5$ to $2p_9$ in the near infrared at 812 nm which is a standard laser wavelength. The metastable $1s_5$ state has a lifetime of ∼38 s, which is much longer than the time scale needed for detecting an atom in a MOT being around one second.

Besides the cycling transition for laser cooling the argon atoms, there is a useful quenching transition at 802 nm for removing an argon atom from the metastable state. The atom is excited to the $2p_8$-state from where it most probably decays to the $1s_4$-state under the emission of a 843 nm photon. From the transient $1s_4$-state the atom decays to the ground state emitting a UV-photon at 107 nm.

The ^{39}Ar-levels are shifted by 95 MHz due to its different mass with respect to ^{40}Ar. In contrast to the even argon isotopes that have a zero nuclear spin, ^{39}Ar has a nuclear spin $I = 7/2$ which leads to a hyperfine splitting of a level with the total angular momentum J into $|2J + 1|$ sublevels with the new quantum number $F = |J - I| ... |J + I|$. The hyperfine splitting of the $1s_5(J = 2)$ and $2p_9(J = 3)$ levels is depicted in figure 2.6. The selection rule

$$\Delta F = 0, \pm 1 \tag{2.16}$$

implies that the transitions $F_2 = 11/2 \rightarrow F_3 = 13/2$ and $F_2 = 3/2 \rightarrow F_3 = 1/2$ are the most suitable choice for a cooling transition, since from the excited state they can only go back to the ground state. Out of these two candidates, the $F_2 = 11/2 \rightarrow F_3 = 13/2$ transition is chosen for cooling, due to the larger energy difference of the $F_3 = 13/2$ to the adjacent $F_3 = 11/2$-level, more effectively suppressing off-resonant excitations.

They nevertheless occur, but can be addressed by repumpers that bring the atoms back into the cooling cycle. Moreover, the repumpers shovel the population from all hyperfine states into the $F_2 = 11/2$-level, resulting in a higher fraction of atoms being laser cooled. Assuming that the atoms are initially distributed over all hyperfine levels weighted with their degeneracy, i. e.

$$\begin{array}{rccccc} F_2 & 3/2 & 5/2 & 7/2 & 9/2 & 11/2 \\ \text{degeneracy} & 4 & 6 & 8 & 10 & 12 \\ \text{fraction of atoms} & 10\% & 15\% & 20\% & 25\% & 30\% \end{array} \tag{2.17}$$

three times more atoms enter the cooling cycle with all four repumpers compared to no repumpers.

The energy levels of ^{39}Ar have been measured within the scope of this project by modulation-transfer spectroscopy [64]. Slightly corrected values were obtained in a later measurement by the authors of [65].

2.6 Interaction of argon with light

If an ideal two-level system with resonance frequency ω_0 is illuminated by laser light with frequency ω_l, the atom will absorb and emit photons at the rate

$$\gamma_s = \frac{\gamma}{2} \frac{s}{1 + s + \frac{4\delta^2}{\gamma^2}} \tag{2.18}$$

where $\delta = \omega_0 - \omega_l$ denotes the detuning of the laser light and

$$\gamma = 2\pi \cdot 5.87\,\mathrm{MHz} \tag{2.19}$$

the spontaneous decay rate of argon's $2p_9$-level corresponding to a life time of

$$\tau = \frac{1}{\gamma} = 27.09\,\mathrm{ns} \quad . \tag{2.20}$$

The saturation parameter

$$s = \frac{2|\Omega|^2}{\gamma^2} \tag{2.21}$$

is determined by the Rabi frequency

$$\Omega = -\frac{\mu_{eg} E_0}{\hbar} \tag{2.22}$$

which in turn is defined by the transition dipole moment

$$\mu_{eg} = e \langle e | \hat{\epsilon} \cdot \boldsymbol{r} | g \rangle \,. \tag{2.23}$$

Here, e denotes the electric charge of an electron, $|g\rangle$ the ground and $|e\rangle$ the excited state. $\hat{\epsilon}$ represents the unit polarization vector of the light and $\boldsymbol{r}$ the coordinate of the electron.

Argon exhibits fine structure such that the ground state $|g\rangle = 1s_5(J = 2)$ and the excited state $|e\rangle = 2p_9(J' = 3)$ respectively split into $|2J + 1| = 5$ and $|2J' + 1| = 7$ magnetic sublevels which are determined by the quantum numbers J and m_J. The transition dipole moment therefore becomes[4]

$$\mu_{eg} = e \langle J', m'_J | \hat{\epsilon} \cdot \mathbf{r} | J, m_J \rangle \tag{2.24}$$

written in terms of the eigenfunctions

$$|J, m_J\rangle = \sum_i C_i \,|L, m_L\rangle \,|S, m_S\rangle \tag{2.25}$$

---

[4] LS-coupling based on the total angular momentum $\boldsymbol{L} = \sum \boldsymbol{l_i}$ and the total spin $\boldsymbol{S} = \sum \boldsymbol{s_i}$ coupling to the total angular momentum $\boldsymbol{J} = \boldsymbol{L} + \boldsymbol{S}$ has been assumed here. This is contradicting the Racah-coupling employed so far, where $\boldsymbol{J} = \boldsymbol{K} + \boldsymbol{s}$ (for notation see [63]). However, it is common practice to use LS-coupling for argon when the magnetic sublevels are involved. The results obtained from that are not far from the measured values (an example follows in the next section). Therefore and because of the simplier formalism LS-coupling is also employed in this work.

with the Clebsch-Gordan coefficients

$$C_i = (-1)^{-L+S-m_J}\sqrt{2J+1}\begin{pmatrix} L & S & J \\ m_L & m_S & -m_J \end{pmatrix} \tag{2.26}$$

expressed in terms of the Wigner 3j-symbol. Evaluating (2.24) with the Clebsch-Gordan coefficients leads to the expression given in [66] which for the $1s_5 \leftrightarrow 2p_9$ transition reads

$$\mu_{eg} = (-1)^{L'+S-m'_J}\,\langle L'||e\boldsymbol{r}||L\rangle\,\sqrt{(2J+1)(2J'+1)}\begin{Bmatrix} L' & J' & S \\ J & L & 1 \end{Bmatrix}\begin{pmatrix} J & 1 & J' \\ m_J & \Delta m & -m_{J'} \end{pmatrix}$$

notated with the reduced matrix element, the Wigner 6j-symbol and $\Delta m = m_{J'} - m_J$. The transition strength is proportional to the absolute square of the transition dipole moment

$$|\mu_{eg}|^2 = \alpha \cdot (2J'+1)\begin{pmatrix} J & 1 & J' \\ m_J & \Delta m & -m_{J'} \end{pmatrix}^2 \tag{2.27}$$

where

$$\alpha := |\,\langle L'||e\boldsymbol{r}||L\rangle\,|^2(2J+1)\begin{Bmatrix} L' & J' & S \\ J & L & 1 \end{Bmatrix}^2 = \frac{1}{6}|\,\langle L'||e\boldsymbol{r}||L\rangle\,|^2 \tag{2.28}$$

is its maximum value. The transition strength will in the following be given normalized by α, i. e.

$$\text{transition strength} := \frac{|\mu_{eg}|^2}{\alpha}\ . \tag{2.29}$$

The radial term $\langle L'||e\boldsymbol{r}||L\rangle$ is the same for all magnetic substates m_J, so it cancels out when the transition strength is calculated. The transition strengths for the magnetic sublevels of the $1s_5 \leftrightarrow 2p_9$ transition in the stable argon isotopes are printed in figure 2.7.

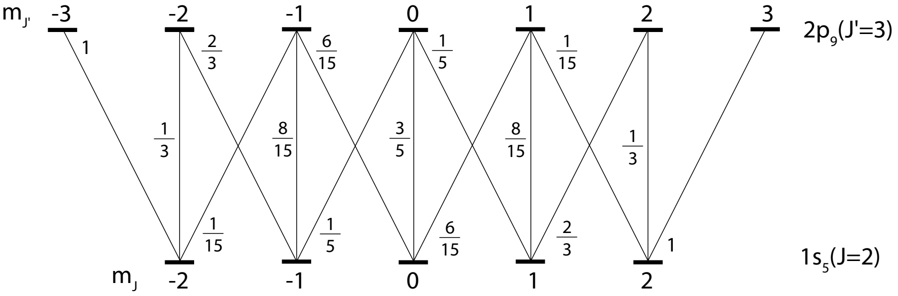

Figure 2.7: Magnetic sublevels of ^{40}Ar with the corresponding transition strengths calculated with formula (2.29).

For ^{39}Ar the transition dipole moment becomes a bit more complicated due to its hyperfine structure. The result can be derived from [66, 67] as

$$\begin{aligned}\mu_{eg} =& (-1)^{1+L'+S+J+J'+I-m_{F'}}\,\langle L'||e\boldsymbol{r}||L\rangle\,\sqrt{(2J+1)(2J'+1)(2F+1)(2F'+1)} \\ &\times \begin{Bmatrix} L' & J' & S \\ J & L & 1 \end{Bmatrix}\begin{Bmatrix} J' & F' & I \\ F & J & 1 \end{Bmatrix}\begin{pmatrix} F & 1 & F' \\ m_F & \Delta m_F & -m_{F'} \end{pmatrix}.\end{aligned} \tag{2.30}$$

The transition strength is obtained accordingly as

$$\frac{|\mu_{eg}|^2}{\alpha} = (2J'+1)(2F+1)(2F'+1)) \begin{Bmatrix} J' & F' & I \\ F & J & 1 \end{Bmatrix}^2 \begin{pmatrix} F & 1 & F' \\ m_F & \Delta m & -m_{F'} \end{pmatrix}^2 . \tag{2.31}$$

Again, the radial term $\langle L'||e\boldsymbol{r}||L\rangle$ is the same for all magnetic substates m_F and cancels out in the transition strength. The values for the chosen cooling transition $F_2 = 11/2 \leftrightarrow F_3 = 13/2$ in ^{39}Ar can be found in figure 2.8.

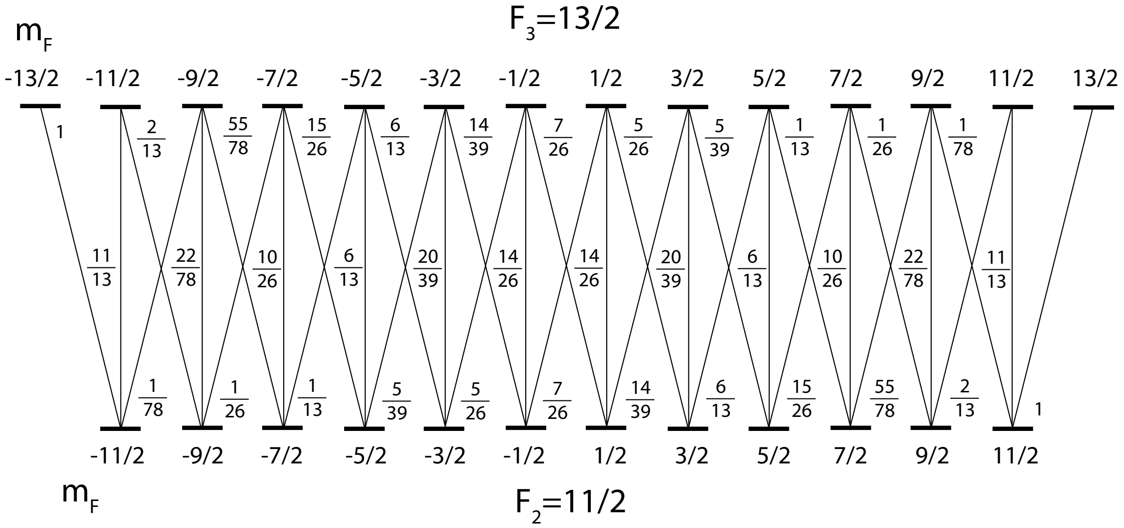

Figure 2.8: Magnetic sublevels of ^{39}Ar with the corresponding transition strengths calculated with formula (2.31).

The saturation parameter introduced in (2.21) can also be expressed in terms of intensities as

$$s = \frac{I}{I_s} \tag{2.32}$$

where

$$I = \frac{1}{2}\epsilon_0 c|\mathbf{E}|^2 \tag{2.33}$$

is the laser intensity, which is related to the absolute square of the electric field by the electric constant ϵ_0 and the speed of light c. The saturation intensity

$$I_s := \frac{\hbar c \epsilon_0 \gamma^2}{4\mu_{eg}^2} \tag{2.34}$$

contains the matrix dipole moment μ_{eg}. Its value depends on the polarization of the incoming light, recalling that light with $\sigma^\pm$ -polarization induces transitions with $\Delta m = \pm 1$ respectively while transitions with $\Delta m = 0$ are driven by linearly polarized light. For **σ^+ or σ^- - light** the atoms will be pumped to the stretched states where the transition strength becomes one. Using the relation [68]

$$\alpha = \frac{3\pi\epsilon_0\hbar c^3}{\tau\omega_0^3} \tag{2.35}$$

the saturation intensity reduces to

$$I_s^\sigma = \frac{\pi h c \gamma}{3\lambda^3} \overset{\text{argon}}{=} 14.4\,{}^{\text{W}}\!/\!{}_{\text{m}^2} \qquad \sigma^+/\sigma^- \text{ - polarization} \tag{2.36}$$

which corresponds to the value obtained for an ideal two-level system.

For π**-polarized light** (linearly polarized along the quantization axis) the situation is more complicated since all magnetic substates are involved in the scattering processes leading to an equilibrium population distribution over the sublevels with an effective transition dipole moment. Due to the given transition strength, the atoms tend to accumulate in the substates near $m = 0$. However, for a rough estimate of the effective saturation intensity, it may be assumed, that the atoms are equally distributed over all substates, leading to a mean transition strength for ^{40}Ar as well as for ^{39}Ar of around 0.5. The saturation intensity then doubles to

$$I_s^\pi = \frac{2\pi h c \gamma}{3\lambda^3} \overset{\text{argon}}{=} 28.8\,{}^{\text{W}}\!/\!{}_{\text{m}^2} \qquad \pi \text{ - polarization} \; . \tag{2.37}$$

For **isotropic polarization** (i. e. laser light with equal components of all three possible polarizations) the transition strength is independent of the distribution of the atoms among the substates. The sum of the transition strengths from a ground state sublevel m_J to the possible excited sublevels $m_{J'}$ is independent of the chosen ground state sublevel. As can be verified from figure 2.7, the sum for ^{40}Ar yields

$$\sum_{m_{J'}} \frac{|\mu_{eg}(m_J \rightarrow m_{J'})|^2}{\alpha} = \frac{2J'+1}{2J+1} = \frac{7}{5} \tag{2.38}$$

and correspondingly for ^{39}Ar

$$\sum_{m_{F'}} \frac{|\mu_{eg}(m_F \rightarrow m_{F'})|^2}{\alpha} = \frac{2F'+1}{2F+1} = \frac{7}{6} \quad . \tag{2.39}$$

Since the light has equal components of σ^+, σ^- and π polarization, the transition strength will on average be

$$\frac{|\mu_{eg}|^2}{\alpha} = \frac{1}{3} \cdot \begin{cases} {}^{7}\!/\!{}_{5} & \text{for } ^{40}\text{Ar} \\ {}^{7}\!/\!{}_{6} & \text{for } ^{39}\text{Ar} \end{cases} \tag{2.40}$$

finally leading to the saturation intensity for isotropic polarization

$$I_s^{\text{iso}} = \frac{\pi h c \gamma}{\lambda^3} \cdot \begin{cases} {}^{5}\!/\!{}_{7} = 30.86\,{}^{\text{W}}\!/\!{}_{\text{m}^2} & \text{for } ^{40}\text{Ar} \\ {}^{6}\!/\!{}_{7} = 37.03\,{}^{\text{W}}\!/\!{}_{\text{m}^2} & \text{for } ^{39}\text{Ar} \end{cases} \qquad \text{isotropic polarization} \; . \tag{2.41}$$

The calculated saturation intensities imply a slightly lower scattering rate γ_s for ^{39}Ar with respect to ^{40}Ar for light with isotropic polarization. For σ^+/σ^--polarization, the scattering rate can also be a little smaller for ^{39}Ar atoms, due to the higher number of scattered photons it needs to reach the outer states. From this, it is expected that slightly more laser power is needed for ^{39}Ar than for ^{40}Ar.

2.7 Interaction of argon with magnetic fields

For ^{40}Ar, that does not have a nuclear spin, the energy shift due to a small external field (Zeeman-regime) in z-direction is [69]

$$E_Z(J, m_J) = m_J g_J \mu_B B \tag{2.42}$$

where[5]

$$g_J = g_L \frac{J(J+1) - S(S+1) + L(L+1)}{2J(J+1)} + g_S \frac{J(J+1) + S(S+1) - L(L+1)}{2J(J+1)} \tag{2.43}$$

is the Landé-factor with the g-factors of the electron $g_L = 1$ and $g_S \approx 2$. For the $1s_5 (J = 2)$ and the $2p_9 (J = 3)$ levels the formula yields

$$g_2^c = 1.5012 \qquad g_3^c = 1.3341 \qquad \text{(calculated)} \tag{2.44}$$

which is close to the measured values [70, 71]

$$g_2 = 1.5008(2) \qquad g_3 = 1.3335(1) \qquad \text{(measured)}. \tag{2.45}$$

These measured values will be used for all subsequent calculations.
The Zeeman shift for ^{39}Ar, being different from ^{40}Ar due to its nuclear spin $I = 7/2$, is [72]

$$E_Z(F, m_F) = m_F g_F \mu_B B \tag{2.46}$$

with the g-factor

$$g_F = g_J \frac{F(F+1) - I(I+1) + J(J+1)}{2F(F+1)} + \frac{m_e}{m_p} g_I \frac{F(F+1) + I(I+1) - J(J+1)}{2F(F+1)} \tag{2.47}$$

where m_e and m_p denote the mass of the electron and the proton respectively. Due to their ratio of $m_e/m_p \approx 1/1836$ the second term in (2.47) may be neglected. The Landé-factor of the ^{39}Ar nucleus

$$g_I = \frac{\mu_I}{\mu_N I} = 0.45538 \tag{2.48}$$

is calculated from its nuclear magnetic moment [73]

$$\mu_I = -1.588(15) \mu_N \tag{2.49}$$

with the nuclear magneton μ_N.

---

[5] Again LS-coupling is employed, despite the general description of the argon spectrum in terms of Racah-coupling.

The g-factors for the cooling transition of ^{40}Ar and ^{39}Ar are included in figure 2.9, where the Zeeman splitting is illustrated.

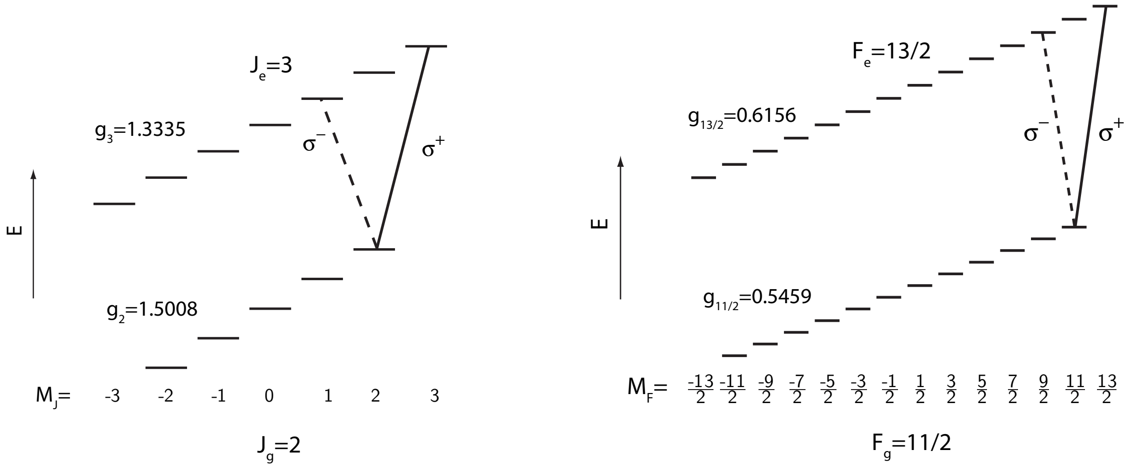

Figure 2.9: Zeeman splitting of ^{40}Ar (left) and ^{39}Ar (right) in a magnetic field.

The frequency difference between the Zeeman shifted stretched levels $(J = 2, m_J = 2) \to (J = 3, m_J = 3)$ of ^{40}Ar, addressed by σ^+-polarization, is

$$\Delta\omega_Z^+ = (3g_3 - 2g_2)\frac{\mu_B B}{\hbar} = 1 \cdot \frac{\mu_B B}{\hbar} \qquad (^{40}\mathrm{Ar}) \tag{2.50}$$

For the corresponding transition in ^{39}Ar (see figure 2.9) the frequency shift becomes

$$\Delta\omega_Z^+ = \left(\frac{13}{2}g_{13/2} - \frac{11}{2}g_{11/2}\right)\frac{\mu_B B}{\hbar} = 1 \cdot \frac{\mu_B B}{\hbar} \qquad (^{39}\mathrm{Ar}) \ . \tag{2.51}$$

This implies that in a magnetic field the stretched states of ^{39}Ar and ^{40}Ar evolve equally. Consequently, also the force [74]

$$F = \hbar k \frac{\gamma}{2} \frac{s}{1 + s + 4(\delta + \Delta\omega_Z)^2/\gamma^2} < \hbar k \frac{\gamma}{2} =: F_{\max} \tag{2.52}$$

exerted on an atom at rest in a magnetic field (obtained from the scattering rate γ_s given in (2.18)) is the same for a given detuning δ. The frequency shift $\Delta\omega_Z$ added to the resonance frequency ω_0 influences the strength of the force, which is exploited in for example the Zeeman slower or the magneto-optical trap. As $\Delta\omega_Z$ is the same for ^{39}Ar and ^{40}Ar also the force for atoms in the stretched states will be the same, but only as long as the stretched state transition alone is driven. This is not the case in the configuration depicted in figure 2.10.

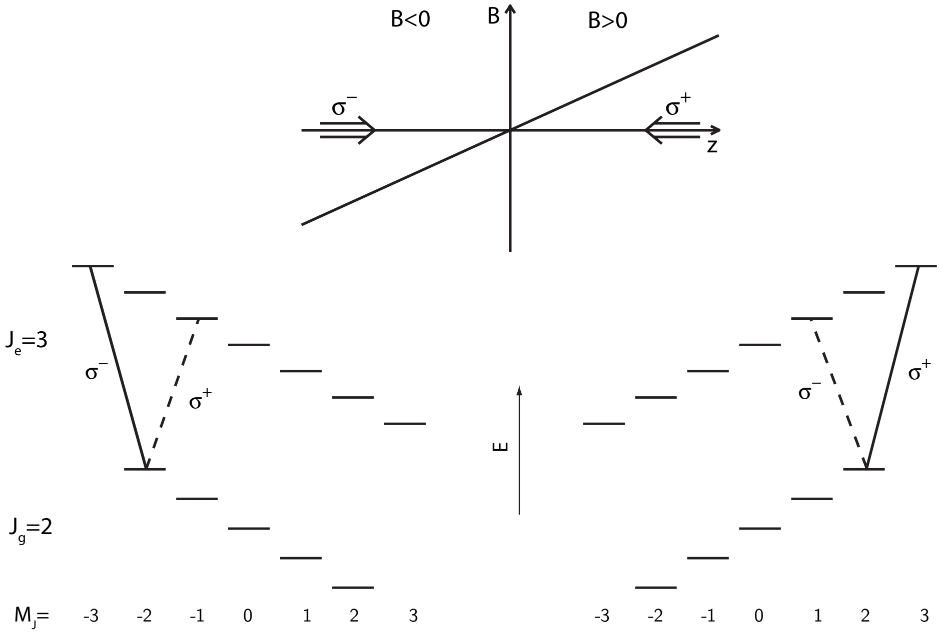

Figure 2.10: Configuration for magneto-optical laser cooling illustrated for ^{40}Ar.

The two opposing laser beams detuned by δ have σ^+/σ^- polarization and therefore induce $\Delta m = \pm 1$ transitions if they become resonant. The configuration is designed such that an atom located on the right side (positive B-field) will be resonant with the σ^+ light while on the left side (negative B-field) it will become resonant with the σ^- light. In this way, the atoms are effectively trapped in the center. However, atoms on the right side will also scatter photons from the σ^--light due to the linewidth of the atomic transition. This leads to a counterforce $\boldsymbol{F}_-$ from the σ^- light opposing the force $\boldsymbol{F}_+$ exerted by the σ^+ light. If the saturation of the laser beams is weak, the total force exerted on the atom by the two laser beams can be approximated by

$$\boldsymbol{F} = \boldsymbol{F}_+ + \boldsymbol{F}_- \tag{2.53}$$

with

$$F_+ = \hbar k \frac{\gamma}{2} \frac{s}{1 + s + 4(\delta + \Delta\omega_Z^+)^2/\gamma^2} \quad , \quad F_- = \hbar k \frac{\gamma}{2} \frac{s}{1 + s + 4(\delta + \Delta\omega_Z^-)^2/\gamma^2} \ .$$

The strength of the counterforce F_- depends on the the frequency shift $\Delta\omega_Z^-$, which is

$$\Delta\omega_Z^- = (1g_3 - 2g_2)\frac{\mu_B B}{\hbar} = -1.67 \cdot \frac{\mu_B B}{\hbar} \qquad \text{for } ^{40}\text{Ar} \tag{2.54}$$

and

$$\Delta\omega_Z^- = (9/2 g_{13/2} - 11/2 g_{11/2})\frac{\mu_B B}{\hbar} = -0.23 \cdot \frac{\mu_B B}{\hbar} \qquad \text{for } ^{39}\text{Ar} \ . \tag{2.55}$$

This implies that for a given magnetic field, the net force on ^{39}Ar will be smaller than for ^{40}Ar as illustrated in figure 2.11.

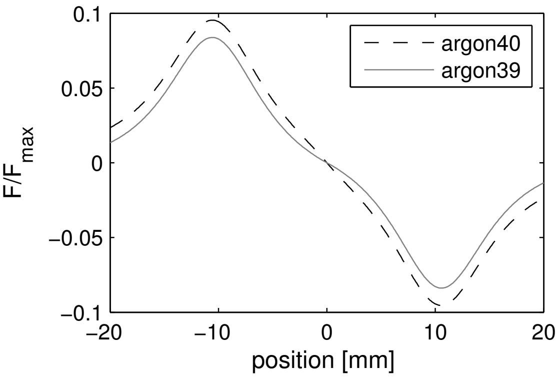

Figure 2.11: Force exerted on ^{39}Ar and ^{40}Ar atoms at rest in a magnetic field with a gradient of 4 G/cm by laser light with a detuning $\delta = \gamma$. The force for ^{39}Ar and ^{40}Ar differ due to the different Zeeman-splitting.

In the presented experiment the configuration shown in figure 2.10 is underlying the magneto-optical trap as well as the magneto-optical lens. There, the behavior of ^{39}Ar and ^{40}Ar needs to be analyzed individually and in general they do not necessarily share the same optimum parameters.

3 Experimental setup

The main parts of the apparatus for ^{39}Ar-ATTA, that has been set up in the course of this thesis, are already described in [10, 5, 75, 76, 63]. This chapter reviews the current apparatus focussing on the aspects that have not been treated yet. Particularly important for the stability of ^{39}Ar measurements was the development of diagnostic methods to monitor the efficiency of the atomic apparatus. These are described after an overview over the entire apparatus has been given. Once the atom beam diagnostics are introduced they provide the means for characterizing the different parts of the atomic beam apparatus.

3.1 Atomic beam apparatus

A schematic of the apparatus is depicted in figure 3.1. The argon atoms are leaving the liquid nitrogen cooled source and are excited to the metastable state in a RF-discharge. The divergent atom beam is subsequently collimated with transverse laser cooling in a tilted mirror setup.

After having passed the first differential pumping tube, the collimated atom beam is focussed with a magneto-optical lens (MOL). In the following differential pumping stage, the ^{40}Ar atoms are removed from the atom beam by quenching them with the 802 nm transition, discussed in section 2.5. The 843 nm light which the ^{40}Ar atoms emit upon deexciting to the ground state, is imaged onto a photodiode as a measure for the metastable atom flux.

Subsequently, the atom beam is longitudinally slowed down in the Zeeman slower from initially $\sim 280\,\mathrm{m/s}$ down to about $50\,\mathrm{m/s}$. A second frequency in the ZSL laser beam, named *Booster*, forms an additional slowing stage with the rising slope of the

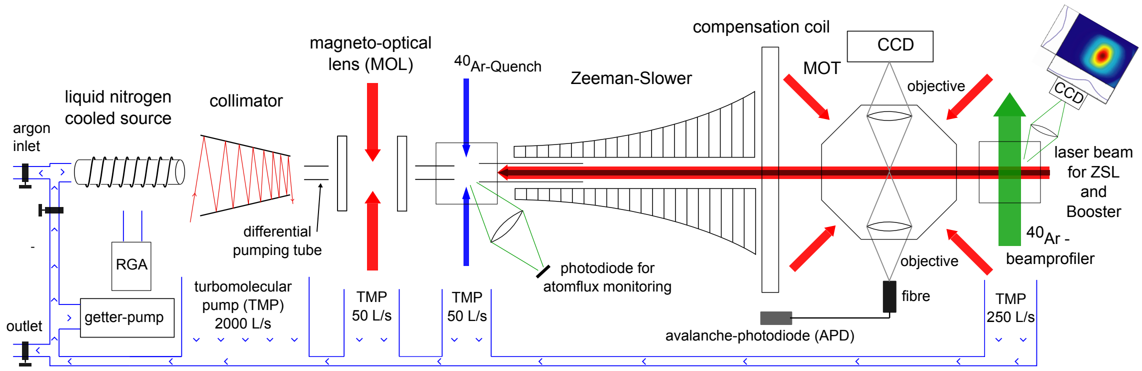

Figure 3.1: Schematic of the atomic beam apparatus, including vacuum features.

MOT magnetic field, where the atoms are slowed down to the capture velocity of the MOT (∼10 m/s). Finally, the atoms are captured in the MOT where their scattering light is imaged onto a CCD-camera on one side, and onto a fibre connected to an avalanche photodiode (APD) on the opposite side. In the chamber behind the MOT, an imaging facility is installed for profiling the ^{40}Ar-beam allowing for precise alignment of the collimator and the MOL.

The different elements of the apparatus will be treated in the following starting with the atom beam diagnostics, which provide the means for characterizing the source and the atom optical components. Figure 3.1 is purposed to provide orientation throughout the entire chapter.

3.2 Atom flux monitoring

^{39}Ar measurements rely on a stable apparatus and on monitoring devices, that can unambiguously identify whether a part of the apparatus is not working at the assigned efficiency. The purpose of the atom flux monitoring is to deliver a signal proportional to the atom flux during an entire ^{39}Ar measurement to assure that the source is operating on the specified performance.

The implementation of the atom flux monitoring exploits the ^{40}Ar-quenching transition discussed in section 2.5 and for clarity illustrated in figure 3.2. During ^{39}Ar measurements the abundant ^{40}Ar atoms are quenched behind the MOL (see figure 3.1) in order to reduce the background of the single atom signal of ^{39}Ar.

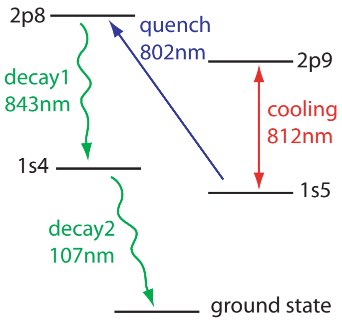

Figure 3.2: Schematic of the relevant transitions for the atom flux monitoring.

^{40}Ar atoms in the metastable $1s_5$ state absorb a photon at 801.699 nm and subsequently decay to the $1s_4$ state under the emission of a photon at 842.696 nm. From the transient $1s_4$ state (∼2 ns lifetime) the atoms decay to the ground state emitting a UV photon at 106.666 nm or 11.7 eV respectively.

This quenching mechanism is very efficient, less than a permil of the ^{40}Ar atoms survive in the metastable level, as observed in the MOT fluorescence. Moreover, the relation between emitted photons and number of atoms is very simple: one atom emits one 843 nm photon and one 107 nm photon, i. e. the number of scattered photons is directly proportional to the atom flux.

The quench light is generated by a seperate diode laser which is stabilized onto the quench transition in ^{40}Ar (see section 3.11).

The first implementation consisted of a Faraday Cup around the atom beam detecting the 107 nm UV photons in the vacuum. This realization had problematic side effects, which is why in the second and final implementation the 843 nm photons are exploited. The two realizations will be described in the following.

Detection of the 107 nm-photons with a Faraday Cup

In a first attempt, it has been tried to detect the UV-photons directly with the Faraday-Cup photographed in figure 3.3. The cathode consists of a stainless steel cylinder with an entrance hole for the quench light on the side. When a UV photon hits the surface of the cylinder an electron is released by the photoeffect with the quantum efficiency QE and accelerated to the positively charged wires leading to a net current proportional to the atom flux. Depending on type and surface preparation, the work function of stainless steel lies around 5 eV [77], which is well below the energy of the UV-photon being 11.7 eV.

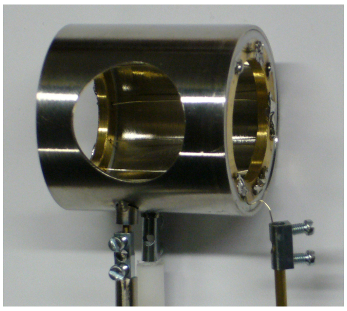

Figure 3.3: Picture of the Faraday Cup used in vacuum for the detection of the 107 nm photons. A UV photon impinging on the stainless steel cylinder releases an electron which then propagates to the positively charged ($\sim$ 10 V) wires leading to a current, that is measured with a picoamperemeter.

A strong signal from the metastable ^{40}Ar atoms of $I_{\mathrm{FC}} \approx 1\,\mathrm{nA}$ was obtained, which was accompanied by a huge background from ions and electrons. This background could be eliminated with a plate capacitor operating at $\pm 1.2\,\mathrm{kV}$ right behind the collimator mirrors. Due to its geometry the Faraday Cup collected a fraction of about $\eta \approx 0.5$ of the photons emitted by the atoms. Together with the solid angle $\Omega_{\mathrm{quench}} \approx 10^{-3}\,\mathrm{sr}$ of the detection region this yields an atom flux density of

$$\frac{^{40}\mathrm{Ar}^*}{\Omega_{\mathrm{quench}}} = \frac{I_{\mathrm{FC}}/e}{\eta \cdot \mathrm{QE} \cdot \Omega_{\mathrm{quench}}} = \frac{1.25 \cdot 10^{13}}{\mathrm{QE}} \frac{\mathrm{atoms}}{\mathrm{s\ sr}} \tag{3.1}$$

where $e = 1.6 \cdot 10^{-19}\,\mathrm{C}$ is the charge of the electron. Unfortunately, no value could be found for the quantum efficiency QE, i. e. for the efficiency of a 107 nm photon to release an electron from a stainless steel surface. Assuming that it is well below the best materials available for photomultipliers [78, 79], one may estimate the quantum efficiency QE to be 1–10 %. The atom flux density would then be $10^{14} - 10^{15}$ $\frac{\text{atoms}}{\text{s sr}}$, which is in the same range as the $5.7 \cdot 10^{14} \frac{\text{atoms}}{\text{s sr}}$ that have been measured for an earlier version of the source [10]. There, the metastable atom flux has been measured directly with a Faraday Cup behind the MOT, assuming an efficiency of 0.15 (based on [80]) for a metastable atom to release an electron from the surface of the stainless steel cup. However, the uncertainty of the quantum efficiency in equation (3.1) precludes a reliable absolute measurement of the atom flux in this configuration.

After one week of operation, the collimator did not work anymore because the mirrors where coated with brown dust, especially close to the high-voltage deflector. This effect might have to do with the dielectric coating of the mirrors that have a weak electric conductivity. Due to the destructive side effect of the Fararaday cup measurements, this method was not pursued. Instead of detecting the 107 nm UV photons it has therefore been changed to detect the 843 nm IR photons.

Detection of the 843 nm-photons with a photodiode

The benefit of detecting the UV photons with a Faraday Cup was the simple implementation inside the vacuum that allowed to collect a big fraction of the emitted UV photons. In order to achieve a large solid angle for the detection of the IR photons, the imaging system illustrated in figure 3.4 was implemented. The photon-collecting part of the objective is inside the vacuum at 45 mm distance from the center of the fluorescence region, leading to a fraction around $\eta = 0.1$ of the entire photon flux being collected. Stray light suppression, especially of the powerful laser beam for the Zeeman slower, is achieved by enclosing the objective in tubes, painted with high absorptivity vacuum paint. Additionally, a 840 nm-bandpass filter suppresses the 812 nm light from the Zeeman slower by several orders of magnitude while still transmitting $\eta_T = 0.9$ of the 843 nm light. Still, a background of 10 % from the Zeeman slower light contributes to the signal. However, since the power of the Zeeman slower light is stabilized this background is constant, so that it does not add noticable fluctuations to the atom flux signal.

For typical parameters, the measured current is $I = 200\,\text{pA}$ through the $1\,\text{cm}^2$ large photodiode, which has an experimentally determined quantum efficiency of QE = 0.7. From this an atom flux density of

$$\frac{{}^{40}\text{Ar}^*}{\Omega_\text{quench}} = \frac{I/e}{\eta \cdot \eta_\text{T} \cdot \text{QE} \cdot \Omega_\text{quench}} \approx 2 \cdot 10^{14}\,\frac{\text{atoms}}{\text{s sr}} \tag{3.2}$$

can be calculated. The main uncertainty in this value results from the difficulty in precisely calculating the fraction of collected photons η. However, the result agrees with all absolute atom flux measurements so far in yielding a value between $10^{14} - 10^{15} \frac{\text{atoms}}{\text{s sr}}$.

The signal on the photodiode saturates as the intensity of the quench light increases, which indicates that all atoms are quenched. A power far in the saturation regime is chosen to prevent that power fluctuations corrupt the signal.

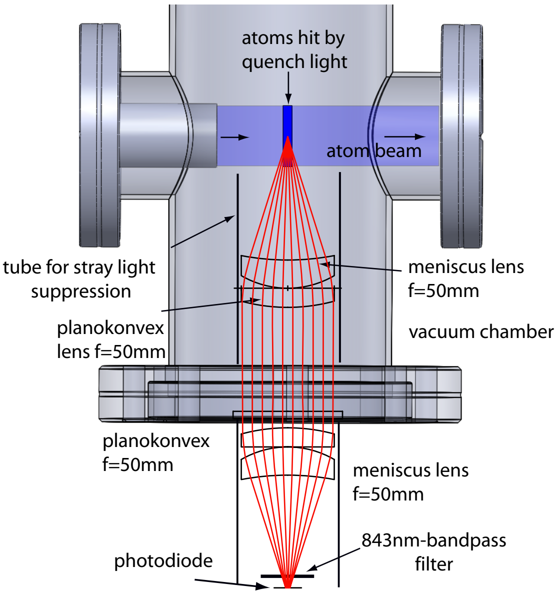

Figure 3.4: Schematic of the atom flux monitoring. The atoms are illuminated by a beam of quench light, narrowed to 5 mm in order to compress the fluorescing region for higher light yield. The 843 nm-photons emitted by the deexciting atoms are collected by a pair of lenses inside the vacuum chamber and are imaged onto a 1 cm^2 photodiode with 70 % quantum efficiency outside of the vacuum chamber. The optics are enclosed in black tubes for stray light suppression. An optical bandpass filter additionally reduces background from the 812 nm Zeeman slower light.

The atom flux signal is constantly recorded during ^{39}Ar measurements and has so far been constant within 10 % during ^{39}Ar measurements as well as from one measurement to another.

3.3 Atom beam profiler

Besides monitoring the metastable flux during ^{39}Ar measurements, the atom flux monitoring in principle also provides a signal for optimizing source, collimator and MOL parameters. However, the atom flux monitoring integrates over the entire flux very close to the latter atom optical stages and therefore neither yields spatial information nor high sensitivity. A much more precise adjustment can be achieved with an atom beam imaging far away behind the MOT, that also features spatial resolution over the cross section of the atom beam. Such an imaging, named *atom* *beam profiler* in the following, has been implemented for ^{40}Ar as illustrated in figure 3.5 and described in more detail in [5].

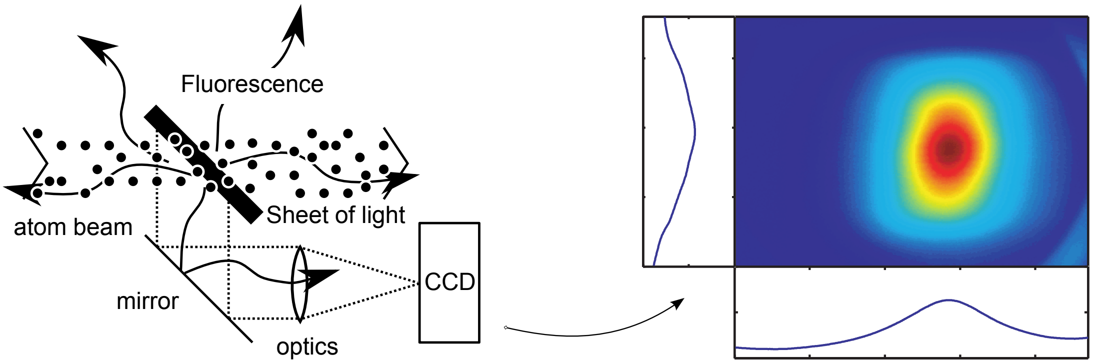

Figure 3.5: Schematic of the atom beam profiler. Left) A sheet of light with a homogenous intensity profile crosses the atom beam at 45°. The fluorescence light is guided with a mirror also tilted by 45° to an objective that images the light onto a CCD-camera. In this way the atom beam is imaged while maintaining its aspect ratio. The power of the light sheet is stabilized to prevent power fluctuations from altering the signal (adapted from [5]). Right) Exemplary image of the collimated and focussed atom beam.

The atom beam profiler is very sensitive to changes in the atom flux, in that it can resolve changes on the percent-level. Moreover, it allows for a very precise positioning of the atom beam due to its spatial resolution.

The atom beam profiler is used for optimization purposes as well as for controlling whether source, collimator and MOL operate at the assigned efficiency before and after ^{39}Ar measurements. However, it does not provide information about the Zeeman slower or the MOT. This is taken care of by the *MOT loading rate* described in the following.

3.4 MOT loading rate

A measure not only for the atom flux but also for the performance of the Zeeman slower and the MOT is the fluorescence of the trapped atoms. If the imaging system captures the fraction η of all photons scattered with the rate γ_s by N atoms trapped in the MOT, then the number of photons per second detected by the camera with quantum efficency QE is

$$\dot{N}_{\mathrm{ph}} = \mathrm{QE} \cdot \eta \cdot \gamma_s \cdot N \ . \tag{3.3}$$

The scattering rate γ_s of a single atom in the MOT depends on parameters such as detuning, magnetic field gradient and saturation of the laser beams (see section 2.6).

If these parameters are kept fixed, the fluorescence signal on the camera depends only on the number of atoms in the MOT. This number in turn depends on the loading rate R, on the mean time between collisions with background atoms τ (later called lifetime of the MOT) and on collisions among metastable atoms characterized by the time constant τ_m. These effects can be approximated by the differential equation [81]

$$\dot{N} = R - \frac{1}{\tau}N - \frac{1}{\tau_m}N^2 \tag{3.4}$$

which has the steady-state solution for $\dot{N} = 0$

$$N(t) \xrightarrow{t\to\infty} N_\infty = \frac{\sqrt{\tau_m^2 + 4R\tau^2\tau_m} - \tau_m}{2\tau} \quad . \tag{3.5}$$

Collisions among metastable atoms in the MOT can be neglected for small atom numbers N. In that case the solution of (3.4) is

$$N(t) = \tau R\left(1 - e^{-t/\tau}\right) + N_0 e^{-t/\tau} \xrightarrow{t\to\infty} R\tau \quad . \tag{3.6}$$

This implies that if collisions between metastable atoms in the MOT can be neglected, the steady state fluorescence $\dot{N}_{\mathrm{ph}}$ of the MOT is proportional to the loading rate R.

However, this is not even the case for the less abundant ^{38}Ar as will become apparent later. Therefore, differential equation (3.4) has to be solved for the general case yielding

$$N(t) = \frac{\tau_m}{2}\left[-\frac{1}{\tau} + \tanh\left(\frac{1}{2}t\sqrt{\frac{4R}{\tau_m} + \frac{1}{\tau^2}} + \operatorname{atanh}\left(\frac{\tau_m}{\sqrt{4R\tau^2 + \tau_m}}\right)\right) \cdot \sqrt{\frac{4R}{\tau_m} + \frac{1}{\tau^2}}\right] \tag{3.7}$$

for $N(0) = 0$. For short times t, this equation can be approximated by

$$N(t) = R \cdot t \tag{3.8}$$

i. e. the number of atoms and thereby the number of detected photons is proportional to the loading rate. Experimentally realizing a short loading time bears the difficulty of preparing an empty MOT at a defined instant of time, such that the MOT is loaded from zero onwards. If only the MOT-beams were shuttered, atoms realeased from the MOT would simply be recaptured. A much more thorough and sustainable emptying of the MOT can be realized with the 802 nm quenching transition. The quench light for ^{38}Ar is derived from the ^{40}Ar-quench light with an AOM operating at 220 MHz, which is the frequency difference between ^{40}Ar and ^{38}Ar. A microcontroller pulses the AOM and generates a corresponding trigger for the camera, as illustrated in figure 3.6.

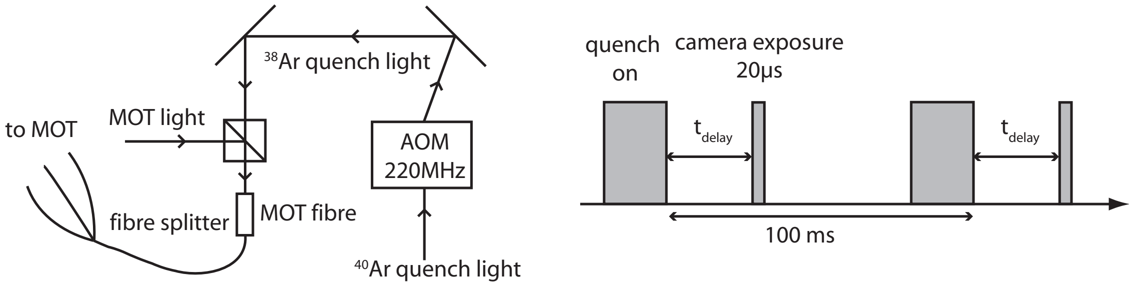

Figure 3.6: Schematic of the experimental implementation for measuring the MOT loading rate. Left) The quench light for ^{38}Ar is derived from the ^{40}Ar-quench light with an AOM operating at 220 MHz and subsequently overlapped with the MOT light. The AOM allows for fast switching of the ^{38}Ar-quench light. Right) Trigger scheme for controlling the AOM and the camera. The MOT beams are constantly on and not switched.

In order to verify equation (3.7) and to obtain an appropriate value for the delay, the fluorescence versus delay has been measured (figure 3.7). The measured curve exhibits the behavior predicted by equation (3.4) if a time-offset of 3.3 ms is included.

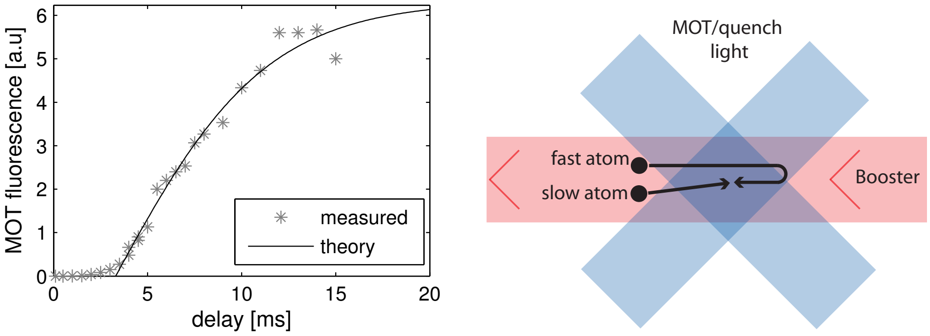

Figure 3.7: Loading dynamics of the MOT. Left) Measured ^{38}Ar MOT fluorescence vs. delay between quenching and camera exposure. The solution of eq. (3.4) can be reasonably fitted to the curve if a time-offset of 3.3 ms is included. Right) Sketch of the loading dynamics due to the Booster.

This offset and the slow increase in the beginning can be explained as a combination of the velocity distribution of the atom beam behind the Zeeman slower and the special loading dynamics of the MOT due to the Booster (figure 3.7) :

Behind the Zeeman slower the velocity distribution of the atoms can be approximated by a Maxwell-Boltzmann distribution with a most probable velocity of about $50\,^{\mathrm{m}}/_{\mathrm{s}}$ whereas the capture velocity of the MOT is only around $10\,^{\mathrm{m}}/_{\mathrm{s}}$. Atoms faster than that are slowed down at the rear end of the MOT by the Booster and subsequently captured by the MOT beams. The time for this process of slowing down and returning to the MOT center is on the order of a few milliseconds. Atoms slower

than the MOT capture velocity can be trapped in the MOT directly.
Another contribution to the small increase in the first few milliseconds originates from atoms that survive the quench and are already near the MOT center when the quench is turned off.

Apart from the initial phase, the dependence of the ^{38}Ar MOT fluorescence can be described by the solution of (3.4) showing an approximately linear behavior between 5 ms and 7 ms. A delay of 6 ms is therefore chosen for measurements of the loading rate. Work is in progress to continuously record the entire loading curve for evaluation of the loading rate, expected to yield more robust values.

Instead of measuring the fluorescence after the delay time, one could also shine in the quench light again and measure the emitting 843 nm photons as implemented in the atom flux monitoring. This method has the advantage of being insensitive to factors altering the single atom signal, such as changes in laser power, frequency or magnetic field. A loading rate measurement based on detecting the emitted quench light was realized in [7].

After having introduced the diagnostic tools for analyzing the metastable atom beam, its creation and manipulation will be described in the following. The presented diagnostics will thereby be used for characterization.

3.5 Metastable beam source

As discussed in section 2.5, argon has to be excited from the ground state to the metastable $1s_5$ level in order to make it accessible to laser cooling. Different excitation mechanisms and techniques are described in [82, 10, 63]. There, the main excitation mechanism was identified to be the direct excitation of a ground state argon atom by electron impact:

$$\mathrm{Ar} + \mathrm{e}^- \quad \rightarrow \quad \mathrm{Ar}^* + \mathrm{e}^- \quad .$$

The energy of the electron for this process has to be at least 11.724 eV, which corresponds to an electronic velocity of about $2 \cdot 10^6 \mathrm{m/s}$. Thermal argon atoms only have a kinetic energy of about 0.03 eV, so no excitations can occur as a result of thermal collisions. Due to the same argument no deexcitations are caused by ground state argon atoms, since their energy is too small to excite the metastable atom anywere else.

According to [10] the dominating loss process in the source tube is diffusive loss to the wall, i. e. atoms that collide with the wall of the source are deexcited. Due to this effect, mainly metastable atoms produced at the end of the source tube survive. Right behind the exit of the source tube, electron impact associated processes dominate the loss rate. Although electrons are also responsible for metastable losses, the production is still on the positive side, such that a high electron density is desired. Figure 3.8 shows a calculated profile of $\rho_{\mathrm{exc+surv}}$, which is the metastable production density multiplied by the probability to survive until the end of the source. The profile is plotted for a plasma that terminates at the exit of the source tube as well as for a plasma that reaches further into the vacuum. The excitation efficiency η is higher for the latter situation.

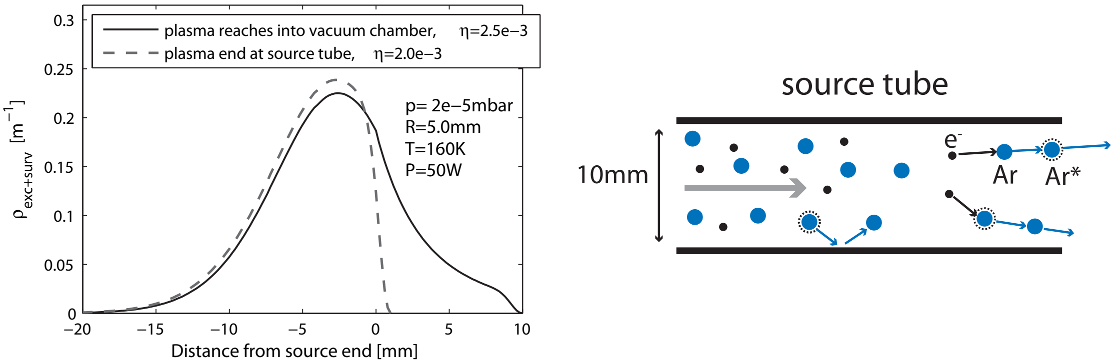

Figure 3.8: Production of metastables in the source tube. Left) Profile of the metastable production density multiplied by the probability to survive until the end of the source for the current experimental values, which are a RF power of 50 W, a pressure in the chamber of $2 \cdot 10^{-5}$mbar and a temperature of 160 K derived from measurements of the longitudinal velocity distribution. A plasma reaching into the vacuum chamber yields a higher metastable density (calculated with the model developed in [10]). Right) Sketch of the dominant production and loss mechanisms in the source tube.

Experimentally, a higher plasma density at the exit of the source even reaching into the vacuum has been achieved by placing the source ∼3 cm before the end of the RF-coil (figure 3.10). This change in the source geometry was accompanied by an enhancement in atom flux of 2-3 in comparison to the coil ending at the end of the source tube. Such a big increase cannot be entirely explained by the employed model. Possibly, the plasma also changed to a different operation mode in the new geometry.

With the metastable production model the dependence of the excitation efficiency on temperature can also be calculated (figure 3.9). Two competing mechanisms enter into the calculation: The diffusive loss rate increases with temperature, i. e. the faster the atoms the more likely they will hit the wall of the source tube and deexcite. On the other hand, if the temperature decreases also the electron temperature decreases, which leads to a lower metastable production rate. From these mechanisms an optimum temperature of ∼190 K emerges. The model moreover predicts, that the excitation efficiency doubles if the temperature is decreased from 450 K to 160 K, as is the case in the present setup if the source is cooled with liquid nitrogen. This calculated increase in excitation efficiency conforms to the experimentally found factor of ∼2.6 [83].

It is interesting to notice that the increase in metastable flux due to liquid nitrogen cooling is mainly caused by the increase in excitation efficiency and not by

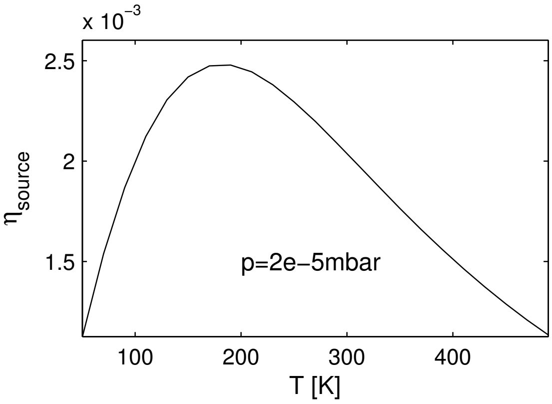

Figure 3.9: Excitation efficiency vs. temperature of the source for the current experimental parameters. Calculated with the model developed in [10].

the collimator or the Zeeman slower. The effect that for lower temperatures the excitation efficiency decreases again has not so far been observed experimentally. Perhaps because such low temperatures have not been reached yet.

A picture of the current source design is shown in figure 3.10. The source coil is wound from 1 mm x 4 mm isolated copper wire with a total length of $\lambda/2$=1.2 m, corresponding to the 130 MHz the RF-discharge is currently operated on. The coil has 10 windings at a diameter of ~35 mm and a length of ~45 mm.

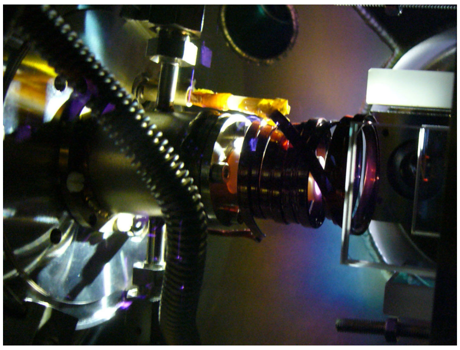

Figure 3.10: Picture of the current source design with liquid nitrogen cooling. The ceramic source tube terminates a few centimetres before the end of the coil, leading to a plasma that reaches further out into the vacuum. The tube is fitted into a stainless steel tin which is liquid nitrogen cooled. The coil is directly followed by the collimation mirrors.

As stated above, no deexcitations can occur due to collisions with ground state atoms. However, outside the source tube a collision with a ground state atom can kick out the metastable atom from the beam. Although still metastable it is lost and will be deexcited when hitting the vacuum chamber.
Collisions with background atoms occur when the mean free path λ becomes comparable to the dimensions of the geometrical restrictions. If $\dot{N}_0$ metastables leave

the source tube per second then after the distance z only

$$\dot{N}(z) = \dot{N}_0 e^{-\frac{z}{\lambda}} \tag{3.9}$$

atoms remain due to collisions with background atoms. The mean free path can be calculated as

$$\lambda(p) = \frac{1}{\sigma_{\mathrm{mg}} n(p)} = \frac{k\ T}{\sigma_{\mathrm{mg}}\ p} \tag{3.10}$$

for a particle density n at a pressure p and a temperature T. The cross section for collisions between metastable and ground state argon has been computed in [10] to[1]

$$\sigma_{\mathrm{mg}} \approx 300\,\mathrm{\mathring{A}}^2 \quad . \tag{3.11}$$

The metastable atoms leaving the source have a temperature around 160 K deduced from the longitudinal velocity distribution. The background gas instead should be thermalized with the vacuum chamber on about 300 K. In the mean free path, the density of the obstacle particles enter, therefore $T_{\mathrm{chamber}} = 300\,\mathrm{K}$ is used leading to

$$\lambda(p) = \frac{1}{\sigma_{\mathrm{mg}} n(p)} = \frac{13.9 \mu m}{p/\mathrm{mbar}} \ . \tag{3.12}$$

For a pumping speed $S = 2000\,\mathrm{l/s}$, the number of metastable atoms leaving the source tube per second is

$$\dot{N}_0 = \frac{S \cdot p}{k T_{\mathrm{chamber}}} \cdot \eta_{exc}(p) \tag{3.13}$$

which contains the pressure dependent excitation efficiency, that can be calculated with the model employed above (left of figure 3.11). The metastable flow (3.13) then follows as plotted in figure 3.11 together with the signals measured 50 cm further downstream by the atom flux monitoring and 270 cm away from the source by the atom beam profiler.

---

[1] A differing value of $\sigma_{mg}^{\mathrm{MOT}} = 1198(211)\,\mathrm{\mathring{A}}^2$ has been measured in this experiment [10].

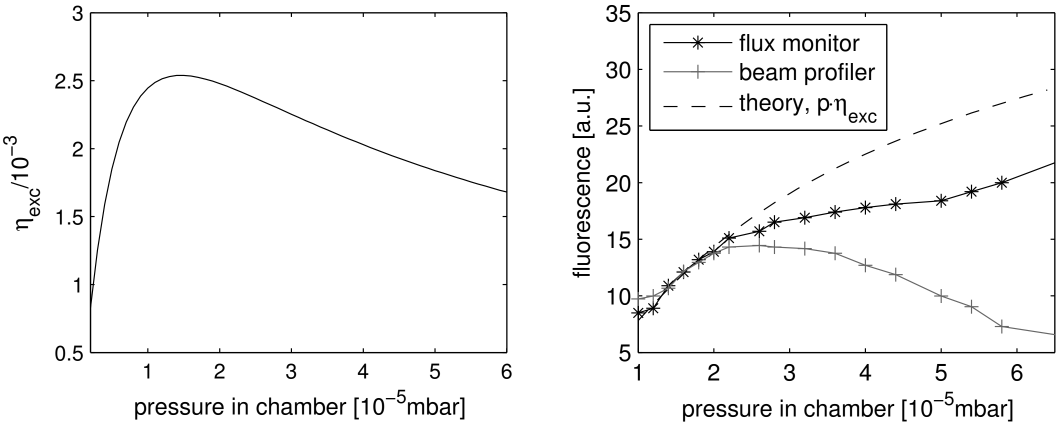

Figure 3.11: Pressure dependence of the excitation efficiency (left) calculated with the model developed in [10]. The resulting metastable flow according to expression (3.13) is plotted together with the signal from the atom flux monitor and the atom beam profiler on the right. The theory curve and the signal from the atom beam profiler are scaled such that the curves coincide for low pressures.

Although from mean free path considerations, collisions due to background gas should no longer play a role behind the main chamber, the atom flux steadily increases while the atom beam profiler already shows a decline. This indicates a contribution from collisions among atoms in the beam, where the density is expected to be higher than in the background gas. On the long way to the MOT, these collisions seem to be a significant loss mechanism for pressures in the chamber higher than $2 \cdot 10^{-5}$ mbar.

3.6 Atomic velocity distributions

The probability density that an atom leaves the source tube with the radial velocity v_r and the longitudinal velocity v_z is denoted by $f(v_r, v_z)$, which is cylindrically normed by the integral[2]

$$\int_0^\infty \int_0^\infty f(v_r, v_z) v_r dv_r dv_z = 1 \ . \tag{3.14}$$

$f(v_r, v_z)$ describes the atom density in a volume directly behind the source. It is the relevant distribution if the fluorescence of a volume illuminated by laser light resonant to atoms with velocity (v_r, v_z) is detected as is the case for the atom beam profiler.

If it is not the atom density in the fluorescence volume which is of interest, but the number of atoms that pass the volume per unit of time, then a different velocity

---

[2] The spherical integration is already contained in the velocity distribution $f(v_r, v_z)$.

distribution has to be used. The probability that an atom with velocity (v_r, v_z) passes the source exit is given by the distribution

$$f_{\text{flux}}(v_r, v_z) = \frac{1}{\bar{v}} f(v_r, v_z) v_z \tag{3.15}$$

which shall be named *flux distribution* in the following. $f_{\text{flux}}(v_r, v_z)$ is observed when the atoms are detected with for example a Faraday Cup or a multi-channel-plate (MCP), where it is not the density in an illuminated volume but the number of atoms passing per unit of time which is the relevant quantity. In the atom flux monitoring one photon is emitted for each metastable ^{40}Ar atom entering the volume. Therefore $f_{\text{flux}}(v_r, v_z)$ has to be used to evaluate the measured signal. Similarly, for the loading rate of the MOT $f_{\text{flux}}(v_r, v_z)$ is also the relevant distribution. However, since the Zeeman slower can only slow down atoms up to its capture velocity $v_{\text{zsl}} = 600\,{}^{\text{m}}\!/\!_{\text{s}}$, the distribution for the MOT loading rate becomes

$$f_{\text{mot}}(v_r, v_z) = f_{\text{flux}}(v_r, v_z)\Theta(v_{\text{zsl}} - v_z) \tag{3.16}$$

where Θ is the Heaviside function, that is zero for $v_z > v_{\text{zsl}}$.

Most of the following considerations will be representatively made with the velocity distribution $f(v_r, v_z)$, because the atom beam profiler experimentally yields the most stable and precise values. All the obtained characteristics remain qualitatively the same for $f_{\text{flux}}(v_r, v_z)$ and $f_{\text{mot}}(v_r, v_z)$. Where a distinct behaviour occurs and for explicit analysis of the atom flux monitoring and the MOT loading rate, the corresponding velocity distributions will be employed.

The longitudinal velocity distribution $f_z(v_z)$ was measured to be well approximated by a 3D-Maxwell Boltzmann distribution [83]

$$f_z(v_z) = \int_0^\infty f(v_r, v_z) v_r dv_r = \frac{4}{\sqrt{\pi}} \frac{v_z^2}{\hat{v}^3} e^{-\frac{v_z^2}{\hat{v}^2}} \tag{3.17}$$

where the most probable longitudinal velocity $\hat{v}$ for the liquid nitrogen cooled source resulted in being

$$\hat{v} = 243\,{}^{\text{m}}\!/\!_{\text{s}} \ . \tag{3.18}$$

The radial velocity distribution $f_r(v_r)$ can be approximated by a Gaussian distribution

$$f_r(v_r) = \int_0^\infty f(v_r, v_z) dv_z = \frac{1}{\sigma_r^2} e^{-\frac{v_r^2}{2\sigma_r^2}} \tag{3.19}$$

where the radial root mean square velocity σ_r was measured to be

$$\sigma_r \approx 85\,{}^{\text{m}}\!/\!_{\text{s}} \quad . \tag{3.20}$$

Assuming that the longitudinal and the radial velocity are independent of each other, the total velocity distribution becomes

$$f(v_r, v_z) \overset{\text{assumption}}{=} f_r(v_r) \cdot f_z(v_z) = \frac{4}{\sqrt{\pi}\sigma_r^2} \frac{v_z^2}{\hat{v}^3} e^{-\frac{v_r^2}{2\hat{\sigma v}^2}} e^{-\frac{v_z^2}{\hat{v}^2}} \ . \tag{3.21}$$

The longitudinal part of the introduced velocity distributions is plotted in figure 3.12. The plot implies that the atom flux monitor and the MOT loading rate evaluate higher velocities stronger than the the atom beam profiler.

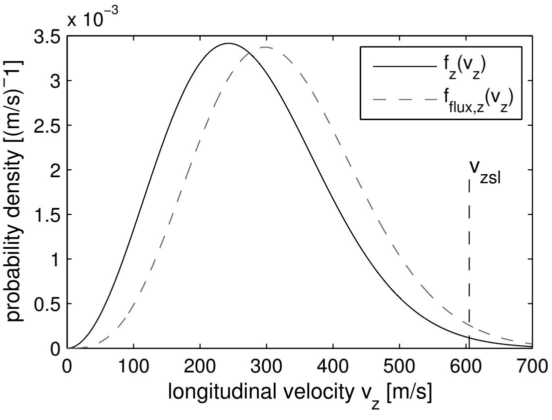

Figure 3.12: Plot of the longitudinal part of the introduced velocity distributions. $f_{\text{flux}}(v_r, v_z)$ is weighted towards higher longitudinal velocities as compared to $f(v_r, v_z)$. $f_{\text{mot}}(v_r, v_z)$ is the same as $f_{\text{flux}}(v_r, v_z)$ but drops to zero for $v_z > v_{\text{zsl}}$.

Using the geometric numbers provided in figure 3.13, the fraction of atoms emerging from the source tube that reaches the MOT calculates to

$$\int_0^\infty \int_0^{\frac{r_{\text{mot}}}{z_{\text{mot}}} v_z} f(v_r, v_z) v_r dv_r dv_z \approx 2 \cdot 10^{-4} \ . \tag{3.22}$$

In other words, only twenty out of a million atoms reach the MOT due to the initial divergence of the atom beam. This motivates a strong need for collimating the atom beam, which is the subject of the following section.

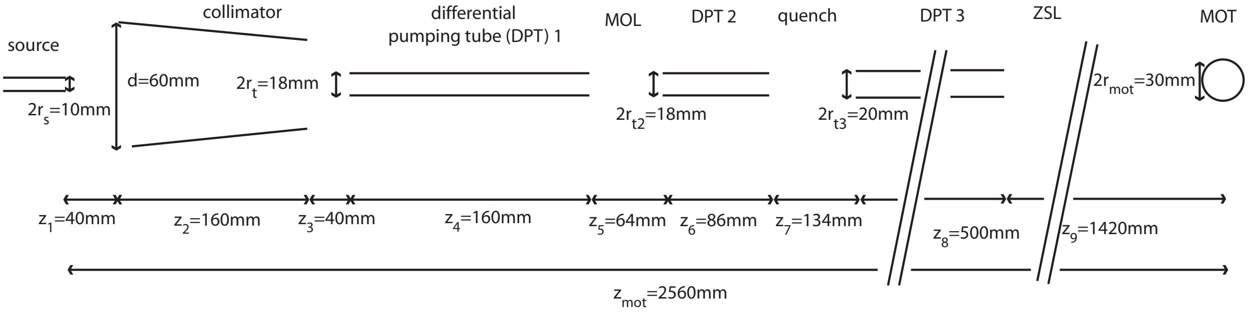

Figure 3.13: Geometry of the apparatus, roughly to scale.

3.7 Collimator

The purpose of the collimator is to guide all atoms that are leaving the source tube to the MOT, such that they can be detected. The collimator implemented in the experiment has been treated in [63]. This section aims at reevaluating the performance of the collimator with the present experimental parameters and at deriving analytical expressions for its optimum conditions.

3.7.1 Ideal collimation

In the following, an ideal collimation with a constant acceleration a is considered to obtain general limitations on the collimation process. The maximum radial velocity for which atoms are collimated[3] and reach the MOT is obtained by solving the following set of equations (see figure 3.13)

$$(i) \quad v_r - a \cdot t_2 = 0 \qquad (ii) \quad v_r(t_1 + t_2) - \frac{1}{2} a t_2^2 = r_t \tag{3.23}$$

where $t_1 = z_1/v_z$ and $t_2 = z_2/v_z$ denote the travel time of the atom for the distances z_1 and z_2 respectively. Solving (3.23) yields the maximum radial velocity for which atoms are collimated and reach the MOT

$$v_{\mathrm{rc}} = \frac{\sqrt{2ar_t} \cdot z_2}{\sqrt{z_2^2 + 2z_1 z_2}} \qquad v_{\mathrm{zc}} = \frac{a z_2}{v_{\mathrm{rc}}} = \sqrt{\frac{a}{2r_t}} \sqrt{z_2^2 + 2z_1 z_2} \tag{3.24}$$

where v_{zc} denotes the corresponding maximum longitudinal velocity. Atoms that are radially faster than v_{rc} would need a longitudinal velocity smaller than v_{zc} to be entirely collimated, leading to a final transverse displacement bigger than r_t. For atoms that are longitudinally faster than v_{zc}, the maximum radial velocity that can be collimated is smaller than v_{rc} and decreases for higher longitudinal velocities. The maximum radial velocity that can be collimated and reaches the MOT as a function of the longitudinal velocity is then obtained similarly to (3.23) as

$$v_{\mathrm{rmax}}(v_z) = \begin{cases} \sqrt{2ar_t + \frac{a^2 z_1^2}{v_z^2}} - \frac{a z_1}{v_z} & v_z \leq v_{\mathrm{zc}} \\ \frac{a\ z_2}{v_z} & v_z > v_{\mathrm{zc}} \end{cases} \tag{3.25}$$

which is plotted in figure 3.14 for $a = a_{\mathrm{max}}/2$. The decrease of v_{rmax} below v_{zc} is due to the distance z_1 between source and collimator. Accounting for atoms that are not entirely collimated within the collimator but still reach the MOT despite their remaining transverse velocity, only moderately increases v_{rmax} (gray dashed line on the right in figure 3.14).

---

[3] i. e. atoms whose transverse velocity is decelerated down to zero.

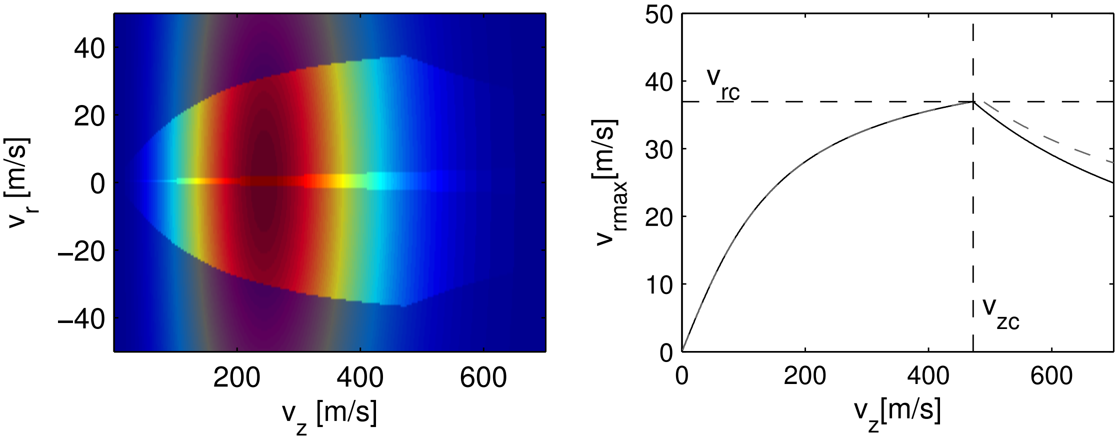

Figure 3.14: Captured velocities calculated for $a = a_{\max}/2$. Left) The captured velocity fraction is plotted in bright colors on top of the velocity distribution $f(v_r, v_z)$. The bright stripe in the center corresponds to the fraction captured without collimation. Right) Maximum radial velocity vs. longitudinal velocity. The radial velocity v_{rc} and the corresponding longitudinal velocity v_{zc} form a pronounced maximum. If atoms are included that are not entirely collimated in the collimator but nevertheless reach the MOT, the gray dashed line defines the maximum radial velocity.

For the current radius of the differential pumping tube $r_t = 9\,\text{mm}$ and the maximum acceleration $a_{\max} = 2.33 \cdot 10^5\,\text{m/s}^2$ the maximum radial velocity that can be collimated and the corresponding longitudinal velocity are obtained to

$$v_{\text{rc}} = 52\,{}^{\text{m}}\!/\!{}_{\text{s}} \qquad v_{\text{zc}} = 668\,{}^{\text{m}}\!/\!{}_{\text{s}}\ . \tag{3.26}$$

Assuming that all velocities up to $v_{\text{rmax}}(v_z)$ are captured, the fraction of atoms that reaches the MOT becomes

$$\int_0^\infty \int_0^{v_{\text{rmax}}(v_z)} f(v_r, v_z) v_r dv_r dv_z \approx 9\,\%\ . \tag{3.27}$$

This means that within the given setup even with optimum collimation only one tenth of the atoms reaches the MOT. If the distance between source tube and collimator could be brought to zero (i. e. $z_1 = 0$) the fraction could be increased to 25%. However, in the current source design it is difficult to reduce the distance. Moving the source tube further towards the collimator will probably come at the cost of excitation efficiency, due to the effects described in section 3.5. Increasing the diameter of the first pumping tube r_t would also result in a higher fraction of atoms reaching the MOT. However, it was already increased by ~50% during a reassembly of the vacuum system. Further increasing it would require a more involved redesign of the vacuum setup in order to maintain a sufficiently low pressure in the MOT chamber.

Liquid nitrogen cooling of the source has reduced the most probable longitudinal velocity of the atoms from 514 m/s down to 243 m/s whereas the transverse velocity stayed constant at ∼85 m/s [83]. With the cooled source the MOT loading rate roughly doubled. The considerations of section 3.5 indicate that this increase results from an enhancement in the excitation efficiency.

In figure 3.15 it is calculated according to expression (3.27) how for an ideal collimation the fraction of detected atoms depends on the most probable longitudinal velocity.

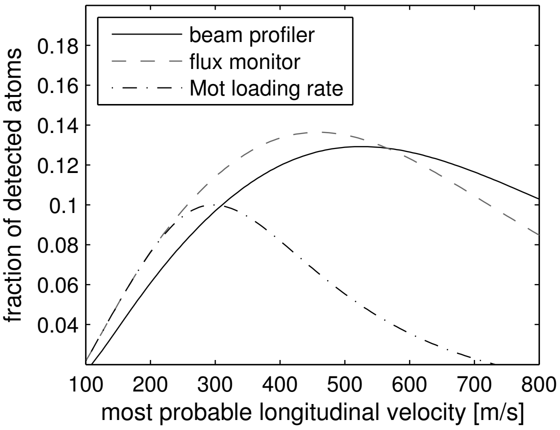

Figure 3.15: Fraction of detected atoms vs. most probable longitudinal velocity calculated according to expression (3.27). f, f_{flux} and f_{mot} correspond to the expected signals from atom beam profiler, atom flux monitoring and MOT loading rate respectively. The transverse velocity distribution is kept fixed which reflects the experimental findings.

Interestingly, an optimum around $\hat{v} = 500$ m/s is expected to be observed for the atom beam profiler and the atom flux monitoring, which is twice the most probable longitudinal velocity of 243 m/s for a liquid nitrogen cooled source. The MOT loading rate instead shows an optimum around $\hat{v} = 300$ m/s, since for velocity distributions shifted towards higher velocities the fraction of atoms that is not captured by the Zeeman slower prevails.

The plotted curves do not include the temperature dependent excitation efficiency (section 3.5), which doubled when going from $\hat{v} = 514$ m/s to $\hat{v} = 243$ m/s [83]. The capture velocity of the Zeeman slower has also been kept fixed, although in practice it could be tuned to higher velocities. However, this would come at the cost of a decrease in capture efficiency [5].

In summary, the curves in figure 3.15 indicate that the observed increase in the signal of the atom beam profiler due to liquid nitrogen cooling is not the result of a higher collimation efficiency, which actually decreases when going to liquid nitrogen temperatures. This decrease in collimation efficiency seems to be outweighed by the increase in excitation and Zeeman slowing efficiency.

3.7.2 Collimation with changing laser angle

The question remains, how the condition of a constant acceleration underlying the ideal collimation described so far can be implemented experimentally. One option would be to use highly saturated laser beams with a detuning chosen such that the power-broadened linewidth covers the ~50 m/s radial velocity range. Assuming homegenuous 20 mm x 150 mm rectangular laser beams, a power of ~1 W would be needed for each laser beam. This is quite a demanding requirement, considering that the laser light is transported through fibres with additional loss processes in front of and behind such that in total more than 4 W of laser power would have to be generated.
A less laser power consumptive method exploits the fact that the Doppler-shift

$$\omega_D = -\vec{k}\cdot\vec{v} = -k\left[v_z\sin(\beta) - v_r\cos(\beta)\right] \approx -k(v_z\beta - v_r) \qquad (3.28)$$

depends on the angle between the atom trajectory with velocity vector $\vec{v}$ and the laser beam with wave vector $\vec{k}$ (figure 3.16). The angle β between the laser beam and the radial axis can be adjusted, such that a large velocity range of atoms stays in resonance during the collimation process (figure 3.16).

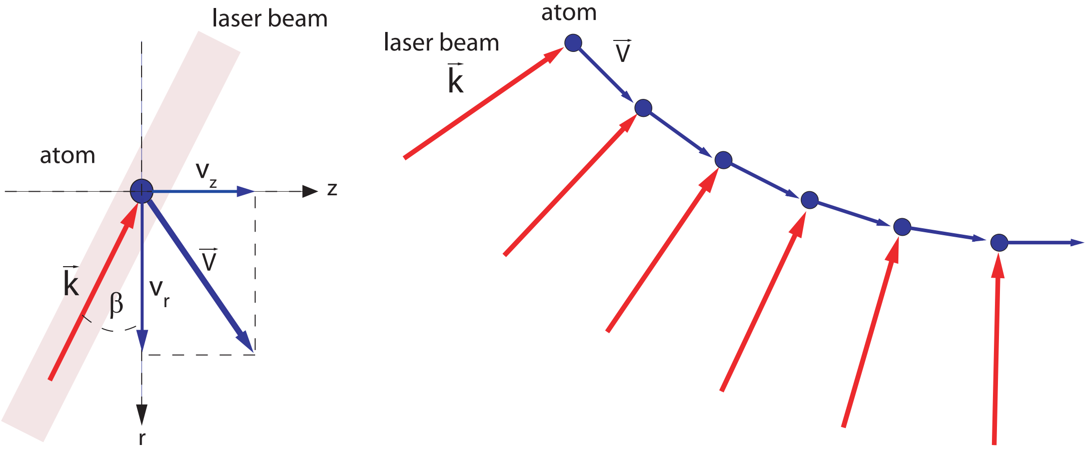

Figure 3.16: Collimation with changing laser angle. The changing Doppler-shift is compensated by a corresponding change in the laser angle β.

If the laser with angular frequency ω_l is detuned from the atomic resonance frequency ω_0 by δ, then the atom is off-resonant by

$$\Delta = \omega_0 - \omega_l = -\omega_D + \delta \approx -k(v_z\beta - v_r) + \delta\ . \qquad (3.29)$$

An atom with inital velocity (v_r, v_z) is resonant during the entire collimation along the z-direction if

$$\Delta = -\omega_D + \delta = k\left[v_r - at - v_z\beta(z)\right] + \delta \overset{!}{=} 0 \qquad (3.30)$$

where $t = z/v_z$ is the travel time for the longitudinal distance z and a the constant acceleration. The longitudinal velocity v_z can be regarded as constant since β is very small. Solving this equation for the angle yields

$$\beta_{\text{ideal}}(z) = \underbrace{\frac{\delta}{v_z k} + \frac{v_r}{v_z}}_{=:\beta_0} - \frac{a}{v_z^2}\, z = \beta_0 - \frac{a}{v_z^2}\, z \ . \tag{3.31}$$

The following considerations aim at deriving expressions for the best choice of the detuning δ and the laser angle β_0.
It seems reasonable to choose them such that atoms with velocity $(v_{\text{rc}}, v_{\text{zc}})$ are collimated down to zero. In that case equation (3.31) yields

$$\beta_0 = \frac{\delta}{k v_{\text{zc}}} + \frac{v_{\text{rc}}}{v_{zc}} \ . \tag{3.32}$$

A further constraint on β_0 and δ can be imposed if one requires, that the laser beam is not resonant with atoms that are moving in the other direction, i. e.

$$v_r = \beta_0 \cdot v_z - \frac{\delta}{k} \overset{!}{>} 0 \quad . \tag{3.33}$$

If it were resonant, the atoms would be accelerated in the wrong direction and thus be decollimated. Rearranging the upper equation for positive β_0 yields

$$v_z > \frac{\delta}{k\beta_0} =: v_{\text{zmin}} \ . \tag{3.34}$$

This implies that for positive detuning δ, atoms with a longitudinal velocity smaller than v_{zmin} are decollimated. Therefore, positive detunings are not a good choice.
For a negative detuning, the laser angle would at some point become negative. As will be discussed later, this situation is not easy to implement experimentally without destroying the collimation efficiency. The following considerations are therefore restricted to positive laser angles, i. e. $\beta(z) \geq 0$. In this case the only solution to (3.32) is

$$\delta_{\text{c}} = 2\pi \cdot 0\,\text{MHz} \qquad \text{and} \qquad \beta_{\text{c}} = \frac{v_{\text{rc}}}{v_{\text{zc}}} = \frac{2 r_t z_2}{z_2^2 + 2 z_1 z_2} \ . \tag{3.35}$$

In figure 3.17 the resonant atoms are shown with and without including the linewidth of the atomic transition. From this it becomes clear that adapting the laser angle alone is not sufficient to capture the entire fraction of atoms that can potentially be captured. Although without including the linewidth atoms with velocity $(v_{\text{rc}}, v_{\text{zc}})$ are slowed down to zero, a significant fraction is not resonant. With a broadened linewidth of $\gamma' = 4\gamma$, which corresponds to a saturation of $s \approx 15$, almost the entire range of velocities can be slowed down to zero.

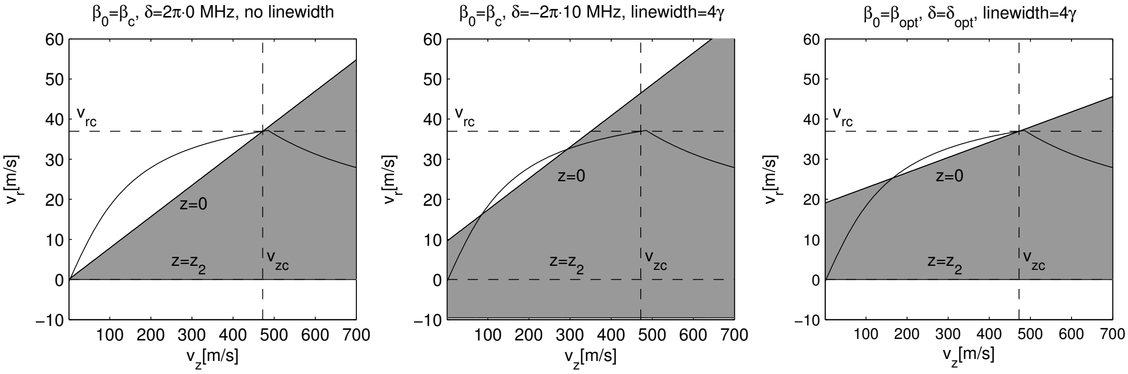

Figure 3.17: Resonant velocities in a changing laser angle scheme with (middle and right plot) and without (left plot) taking into account the linewidth of the atomic transition. Only atoms that have a velocity within the grey shaded area below the curve can reach the MOT. The upper line of the gray area corresponds to the velocities resonant at $z = 0$ while the bottom line corresponds to velocites resonant at $z = z_2$. All plots are calculated for $a = a_{\max}/2$.

However, due to the broadened linewidth atoms moving in the other direction also get into resonance and are thus accelerated in the wrong direction. To a certain extent this can be compensated for by the counterpropagating laser beam which collimates the atoms going in the other direction. Nevertheless, to avoid this effect, the detuning can be chosen, such that only atoms moving towards the laser beam are resonant. This implies that the detuning will differ from the detuning $\delta_c = 2\pi \cdot 0\,\mathrm{MHz}$, which means that the atoms with velocity $(v_{\mathrm{rc}}, v_{\mathrm{zc}})$ will not be perfectly in resonance during the collimation process.

The off-resonance Δ along the z-axis can be further optimized if β_0 is also compromised. The off-resonance over the collimation distance is minimal if

$$\Delta(z=0) = -\Delta(z=z_2) \overset{!}{=} \frac{\gamma'}{2} \tag{3.36}$$

i. e. if atoms with velocity $(v_{\mathrm{rc}}, v_{\mathrm{zc}})$ are equally off-resonant at $z = 0$ and $z = z_2$ by half the broadened linewidth. From this the optimum angle β_{opt} and the optimum detuning δ_{opt} accounting for the broadened linewidth γ' follow as

$$\beta_{\mathrm{opt}} = \frac{a z_2}{v_{\mathrm{zc}}^2} - \frac{\gamma'}{v_{\mathrm{zc}} k} \quad , \quad \delta_{\mathrm{opt}} = k \cdot \left(\frac{\beta_0}{2} \cdot v_{\mathrm{zc}} - v_{\mathrm{rc}} + \frac{a z_2}{2 v_z} \right) \quad . \tag{3.37}$$

In the case of high saturation with a broadened linewidth

$$\gamma' = \frac{k a z_2}{v_{\mathrm{zc}}} \tag{3.38}$$

the optimum laser angle actually becomes zero, reflecting that with sufficient laser power there is no benefit from a changing laser angle scheme.

The expressions for optimum laser angle and detuning, that have been analytically derived for a general collimation scheme with changing laser angles, will later also be confirmed by a numerical simulation that implements the chosen experimental realization with tilted mirrors.

3.7.3 Approximation with tilted mirrors

An experimental realization of the ideal collimation with changing laser angle has to implement or at least approximate the ideal angle curve (3.31) while maintaining a constant acceleration. The different experimental methods for implementing the changing laser angle are for example discussed in [63, 84, 85]. The method employed in this experiment uses tilted mirrors as illustrated in figure 3.18 and described in [63].

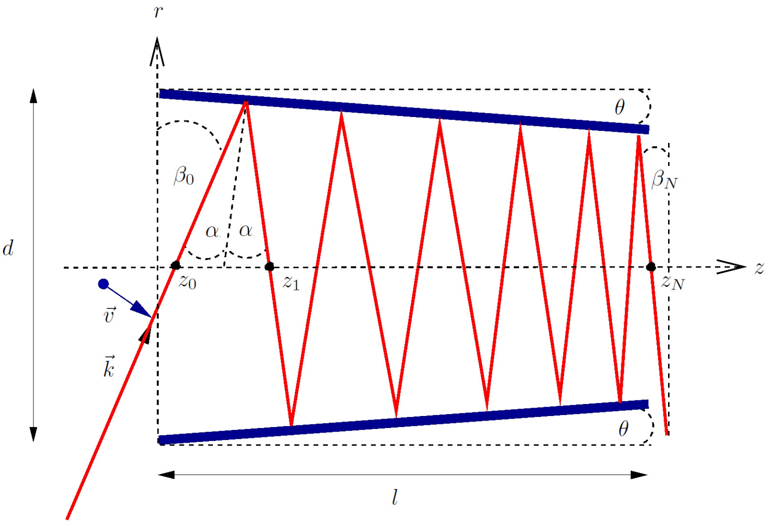

Figure 3.18: Geometry of the collimation with tilted mirrors (from [63]). The entry angle of the laser beam β_0 and the mirror angle θ are critical parameters that need to be optimized.

The laser beam enters the pair of mirrors with an initial angle β_0 which is then gradually decreased with each reflection on the mirrors which are slightly tilted by the angle θ. After n reflections the laser angle can be calculated as[4]

$$\beta_n = \beta_0 - 2n\theta = \sqrt{\frac{4\theta}{d}(z_0 - z_n) + \beta_0^2} \tag{3.39}$$

where z_n denotes the intersection points between the laser beam and the z-axis. If the number of reflections is very high, the intersection points lie very close to each

---

[4] there is an error in the formula given in [63]

other and the transition $z_n \to z$ to a continuous z can be made. This procedure yields

$$\beta_{\text{tilted}}(z) = \sqrt{\frac{4\theta}{d}(z_0 - z) + \beta_0^2} \approx \sqrt{-\frac{4\theta}{d}z + \beta_0^2} = \beta_0\sqrt{1 - \frac{z}{z_{\text{cool}}}} \tag{3.40}$$

where

$$z_{\text{cool}} := \frac{d\beta_0^2}{4\theta} \tag{3.41}$$

denotes the distance at which the laser angle has decreased to zero. If one requires that this happens at the end of the collimator, such that the laser beam does not turn back, i. e.

$$\beta(l) \overset{!}{=} 0 \tag{3.42}$$

then the optimum mirror angle results as

$$\theta_{\text{opt}} = \frac{d\beta_0^2}{4(l - z_0)} \approx \frac{d\beta_0^2}{4l} \ . \tag{3.43}$$

If the laser beam turned around, its wave vector would be inverted, such that it would become resonant with atoms propagating in the wrong direction, which would effectively decollimate them. For the following considerations laser angle and mirror angle are therefore chosen such that the upper conditions are satisfied.

If the distance between the laser beam center and the mirror is chosen to equal the beam waist radius R, then the minimum entry angle for the laser beam before it is chopped can be calculated as

$$\beta_{\min} = \arctan\left(\frac{R}{d}\right) \ . \tag{3.44}$$

This implies, that steeper laser angles can be realized if the distance d between the mirrors is increased.

The optimum laser angle β_{opt} given in equation (3.37) is smaller than $\beta_{\min}$ for typical powers used in the experiment. For the tilted mirror setup the optimum laser angle will therefore be $\beta_{\min}$, also because this corresponds to the highest laser beam density in the collimator. In figure 3.19 the angle curve $\beta_{\text{tilted}}(z)$ of the tilted mirror setup is compared to the ideal curve $\beta_{\text{ideal}}(z)$ (given in equation 3.31) for $\beta_0 = \beta_{\min}$.

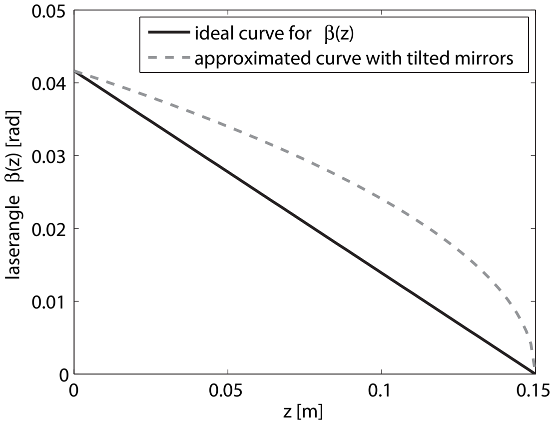

Figure 3.19: Approximation of the ideal angle curve $\beta_{\text{ideal}}(z)$ with the curve $\beta_{\text{tilted}}(z)$ produced by the tilted mirrors.

The tilted mirror setup approximates the ideal angle curve only very roughly due to its square root dependence on z. The starting and final angle of $\beta_{\text{tilted}}(z)$ coincide with the ideal angles $\beta_{\text{ideal}}(z)$, but in between one has to compensate for the deviation in angle with sufficient line-broadening to ensure resonance. One could actually think of bending the mirrors in order to better approximate the ideal curve.

In order to check whether the foregoing considerations and derived expressions for optimum performance on the ideal angle collimation also apply to the approximation with tilted mirrors, simulations are performed. The implemention of the simulation is described in [63], where some basic features have already been simulated, for example that θ_{opt} is in fact the best choice for the mirror angle.

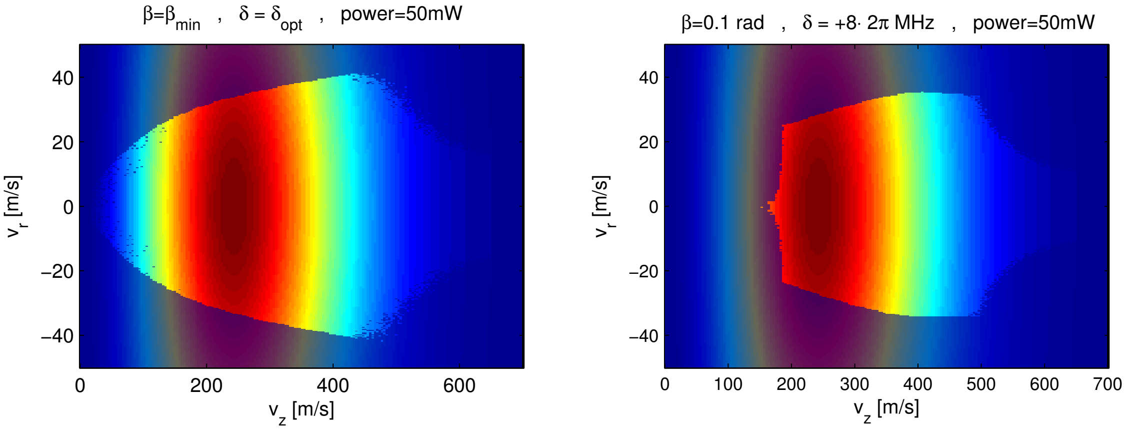

Figure 3.20: Simulated captured velocities. Left) For optimum β_0, δ and θ the simulation reproduces the shape of figure 3.14 that has been calculated for the ideal collimation. Right) If the detuning is positive, longitudinally slow atoms are decollimated as predicted.

In figure 3.20 the captured velocities are simulated for different conditions. The behaviour as derived for the ideal collimation is well reproduced for sufficient laser power and also the decollimation of longitudinally slow atoms for positive detunings becomes manifest.
The simulation furthermore confirms that the optimum detuning in the tilted mirror setup can be described by formula (3.37) including the dependence on β_0 (figure 3.21). The optimum laser angle is also confirmed to be given by β_{min}, if the optimum mirror angle θ_{opt} is chosen as is done for all simulations.

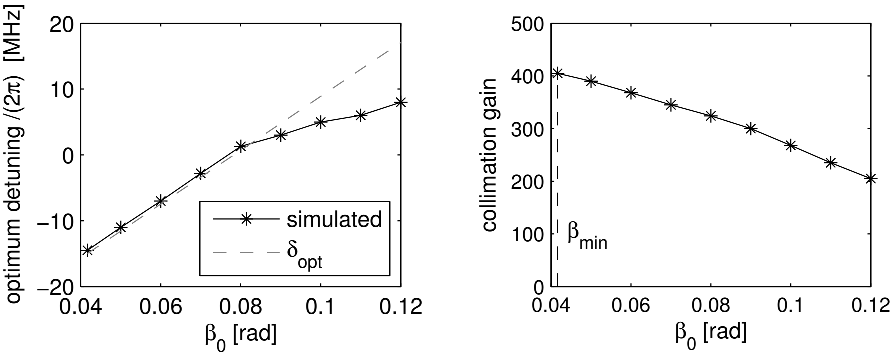

Figure 3.21: Simulated optimum values for collimating with tilted mirrors at a laser power of 50 mW per beam and a reflectivity of $r = 1$. Left) The analytically derived dependence for the optimum detuning δ_{opt} on β_0 is reproduced by the simulation for not too large β_0, where the tilted setup is close to the ideal collimation due to the high density of laser beams. Right) The collimation gain increases towards the minimum laser angle β_{min}.

So far the measurements have been performed with a reflectivity of the mirrors of $r = 1$. The reflectivity of the mirrors is specified by the manufacturer to be bigger than 99.7%. However, the reflectivity drops over time due to bombardment with ions from the source. The maximum collimation gain versus reflectivity is plotted in figure 3.22, which shows that a loss in reflectivity can be compensated by increasing the laser power.

The current collimator has been adjusted to the atom beam profiler. Its experimentally obtained optimum detuning lies at $\delta = +5 \cdot 2\pi\,\mathrm{MHz}$. According to figure 3.21 this corresponds to a laser angle $\beta_0 \approx 0.1\,\mathrm{rad}$. This indicates that decreasing the laser angle β_0 could increase the fraction of captured atoms by a factor of almost two.

A detail that for simplicity has been left out so far is the finite dimension of the source tube of 10 mm. Including this aspect into the simulation only yields a slight decrease in the fraction of atoms reaching the MOT. All findings based on a point-like source remain qualitatively and in approximation also quantitatively the same for a source with finite apperture, as long as it is smaller than r_t.

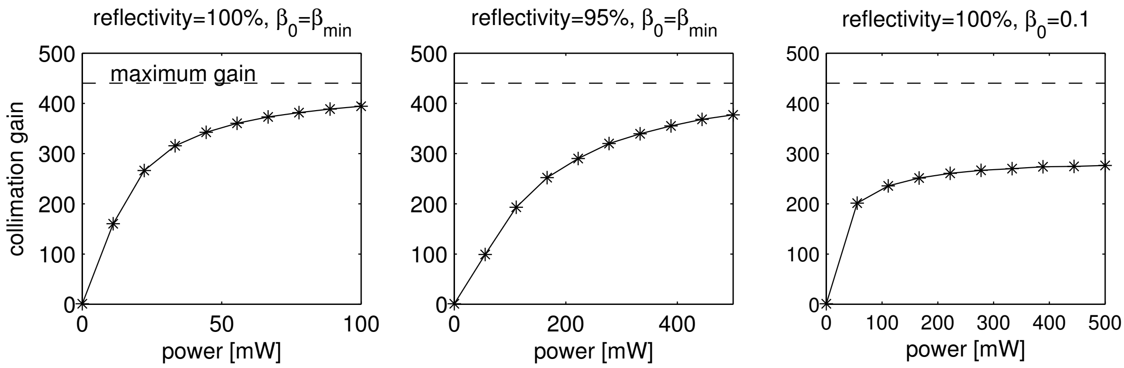

Figure 3.22: Collimation gain vs. laser power for a reflectivity of 100% (left and right) and 95% (middle). In the middle and left plot the laser angle is $\beta_0 = \beta_{\min}$ whereas in the right plot $\beta_0 = 0.1\,\mathrm{rad}$, which is probably the current value in the experiment.

Typical atom trajectories for optimum parameters together with the final beam and velocity profile are depicted in figure 3.23. The final velocity spread of the collimation process is dominated by the Doppler-cooling limit.

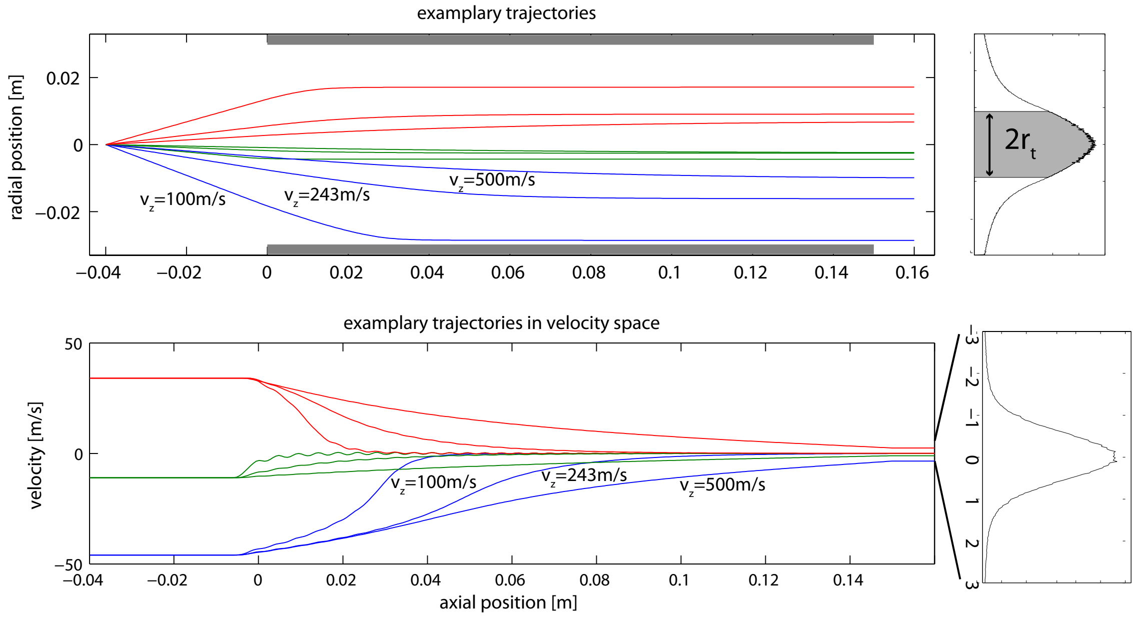

Figure 3.23: Typical atom trajectories in the collimator together with the final beam and velocity profile. Trajectories with the same initial transverse velocity have the same color in the upper and the lower plot. Each initial transverse velocity is plotted for the three longitudinal velocities $v_z{=}100\,\mathrm{m/s}$, $243\,\mathrm{m/s}$ and $500\,\mathrm{m/s}$. The final atom beam profile is constrained by the radius r_t of the differential pumping tube. This particular simulation includes the finite size of the source.

The minimum rms-velocity [85]

$$v_D = \sqrt{\frac{\hbar\gamma'}{2m}} \tag{3.45}$$

that can be achieved in the collimator scheme[5] is determined by the power-broadened linewidth γ'. For typical laser powers the Doppler limit is around 0.5 m/s.

Prior to a redesign of the vacuum system, the atom beam profile behind the collimator has been measured by fluorescence imaging (figure 3.24). The measurement is in good agreement with the simulation. With a diameter of 9 mm for the first differential pumping tube, about 70% of the beam profile are not chopped.

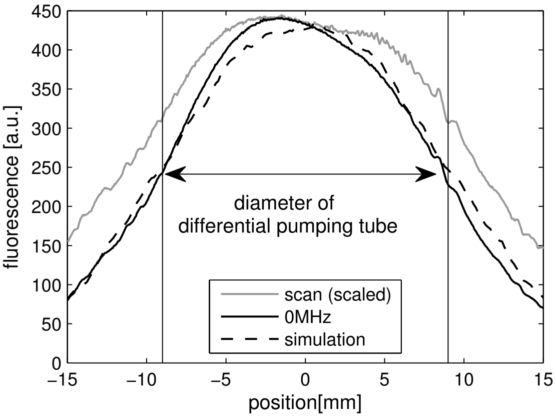

Figure 3.24: Measured and simulated beam profile behind the collimator. The beam profile was measured with laser light transversely illuminating the atom beam and imaged from the front. The fluorescence for resonant as well as for scanning light is shown. Taking into account that the fluorescence image is power broadened, the simulation agrees with the measured atom beam profile.

In table 3.1 the measured, simulated and analytically calculated collimation gain is listed for the different detection methods. The simulated collimation gain is systematically lower than the gain obtained for an ideal collimation due to the non-optimum laser angle β_0 used. The measured collimation gain is systematically lower than the simulated one, which can be the result of uncertainties in the experimental parameters that enter into the simulation, such as the assumptions made for the velocity distribution. The fact that the measured MOT loading rate shows a similar collimation gain as the atom beam profiler is also reflected in the simulation as well as for the ideal collimation.

---

[5] The simulation does not include the random nature of the spontaneous emission, which underlies the Doppler limit. It is accounted for by adding random velocities from a Gaussian velocity distribution with a rms-velocity of v_D onto the final velocity.

Table 3.1: Comparison of the measured, simulated and ideal collimation gain for different detection methods. The ideal collimation is calculated with an acceleration of a_{max}. For the simulation, $\delta = +2\pi \cdot 5\,\text{MHz}$ and the reconstructed value of $\beta_0 = 0.1\,\text{rad}$ have been used.

	atom flux	atom beam profiler	MOT loading rate	^{39}Ar count rate
ideal	38	367	348	
simulated	25	204	206	
measured	19	130	126	87

The collimation enhancement of the ^{39}Ar count rate was determined with an enriched sample, where the ^{39}Ar count rates printed in table 3.2 were measured. As already indicated in [75, 5], the 1st repumper has a significantly smaller effect than expected, probably because it is partly replaced by the Zeeman slower laser beam which is only 66MHz away. Additionally, a fraction of the atoms is lost from the cooling cycle due to the missing 2nd repumper.

Table 3.2: Measured ^{39}Ar count rates in an enriched sample for different sideband coverage in the collimator.

	atoms	atoms/min	factor	theoretical factor
no collimation	18/20min	0.9		
no RP	384/4min	96	107	
1st RP	465/4min	116	1.22	1.83
1st and 2nd RP	781/4min	195	1.70	1.36
1st - 3rd RP	911/4min	228	1.17	1.2
1st-4th RP	934/4min	229	1.03	1.11

The 2nd repumper has a significantly stronger effect than expected merely from pumping sublevels, very likely due to its repumping effect. The increase due to the 3rd repumper is very close to the value expected from addressing the atoms in the $F_g = 5/2$ state. This indicates that a 3rd repumper is not needed for repumping as would be theoretically expected [75, 10]. A significant effect of the 4th repumper is not visible in the measurement and has therefore been removed from the optical setup.

For ^{40}Ar a 10% increase in the atom flux was observed for π-light with respect to an equal superposition σ^+ and σ^- light. This can be explained by the lower saturation intensity for π-light with respect to a mixture of σ^+ and σ^- light, as discussed in section 2.6. To compensate for the slightly higher saturation intensity of ^{39}Ar with respect to ^{40}Ar a laser power well in the saturation regime is chosen.

If the effect due to hyperfine pumping is accounted for, the collimator achieves only a factor of 87 for ^{39}Ar while it should yield the factor of around 130 measured for the MOT loading rate of ^{38}Ar. The foregoing considerations leave inefficient repumping as a main reason for the lower collimation efficiency of ^{39}Ar. A feature that certainly needs further investigation with enriched samples.

3.8 Magneto-optical lens (MOL)

Although behind the collimator the atoms are in principal collimated, a fraction of the atom beam does not reach the MOT due to the remaining transverse velocity spread. This spread becomes particularly detrimental considering that the atoms are longitudinally slowed down in the Zeeman slower, such that the divergence of the atom beam dramatically increases towards the end of the Zeeman slower.

One benefit of the magneto-optical lens is a reduction in the transverse velocity spread, due to the transverse cooling with a low-intensity, red detuned laser beam. The other benefit is that the atom beam is focussed into the MOT, meaning that atoms that are off the beam axis obtain a net velocity towards the center, such that their diffusion out of the beam is less likely.

The simple experimental implementation consists of two coils in Anti-Helmholtz configuration along the beam axis. In this orientation the magnetic field gradient is the same in the directions perpendicular to the atom beam. The MOL-coils have the dimensions shown in figure 3.25 and roughly fulfill the condition $d = \sqrt{3} \cdot r$ for a constant gradient in the center.

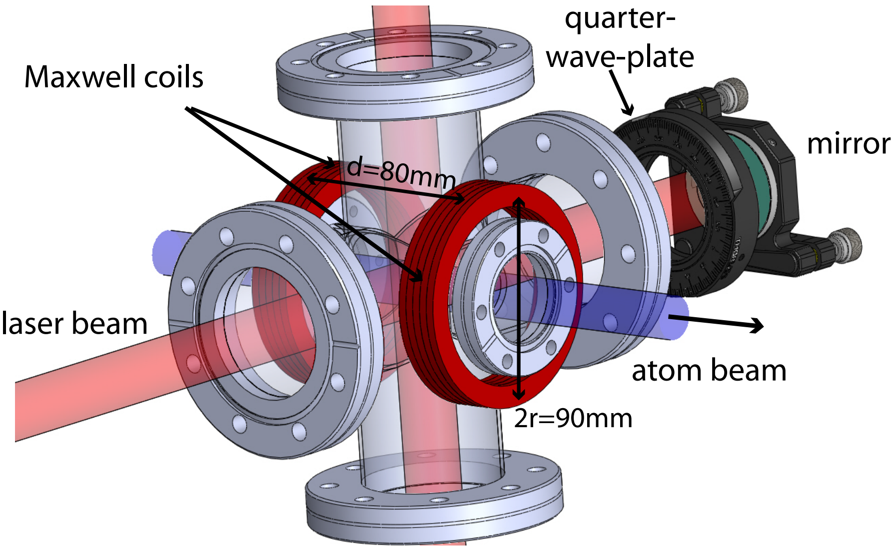

Figure 3.25: Schematic of the MOL setup. The coils, each having 100 windings, in Anti-Helmholtz (or Maxwell) configuration roughly fulfill the condition $d = \sqrt{3} \cdot r$ for a constant gradient in the center. The magnetic field gradient is the same for the directions perpendicular to the beam axis whereas along the beam axis the gradient is twice as strong.

One may think that the Anti-Helmholtz coils, usually employed for a 3D-MOT, are not the best choice in this case, since the magnetic field may not be homogenous over the extension of the MOL-beams, especially because the strongest gradient is along the beam axis. However, the radial component of the magnetic field is rather constant over the extension of the laser beam (25 mm diameter) even in the outer regions of the atom beam (figure 3.26).

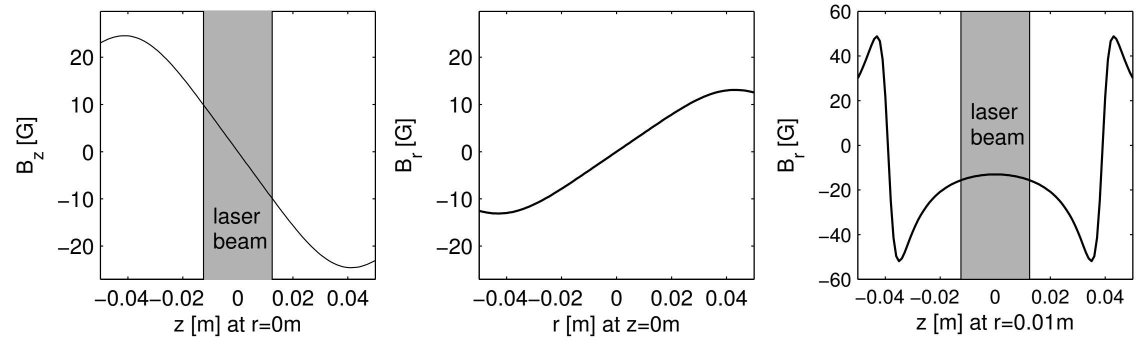

Figure 3.26: Calculated magnetic field of the MOL. Left) z-component of the magnetic field $B_z(z)$ at $r = 0\,\mathrm{mm}$. Middle) Radial component $B_r(r)$ at $z = 0\,\mathrm{mm}$. Right) $B_r(z)$ at $r = 0.01\,\mathrm{m}$, which corresponds to the outer region of the atom beam.

In order to obtain the main features of the MOL, it is simulated in extension to the simulation of the collimator. There, ^{39}Ar could be treated like the stable isotopes. In the MOL, ^{39}Ar behaves differently from the stable isotopes due to the different effective detuning the ^{39}Ar atoms experience in a magnetic field (see section 2.7). In figure 3.27 the fraction of detected atoms is plotted versus the B-field current.

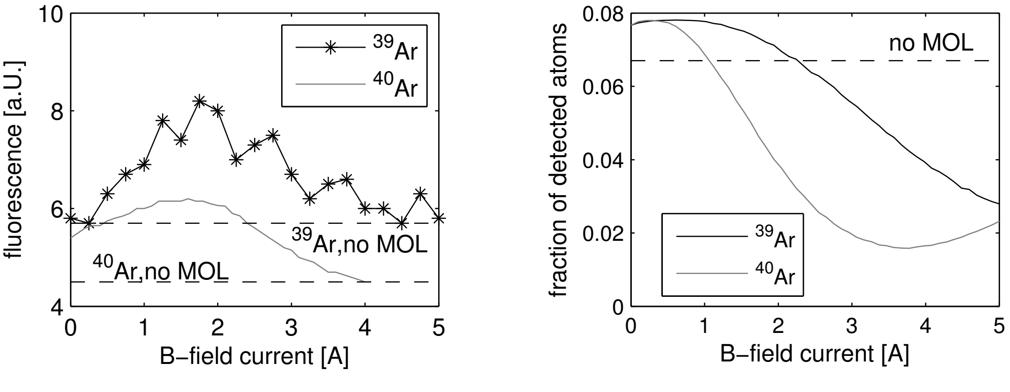

Figure 3.27: Measured (left) and simulated (right) dependence of the fraction of detected atoms on the B-field current for ^{39}Ar and for ^{40}Ar. The measured values for ^{39}Ar were obtained from the MOT-fluorescence of an enriched sample. The values for ^{40}Ar were measured with the atom beam profiler.

The optimum current for the MOL was experimentally found to be around 2 A for ^{39}Ar and slightly lower at 1.8 A for ^{40}Ar which corresponds to a magnetic field gradient in the radial direction of about 4 G/cm. These values deviate from the simulated optimum values of 0.6 A for ^{39}Ar and 0.3 A for ^{40}Ar. A reason for this discrepancy may be magnetic shielding due to the stainless steel vacuum chamber, around which the magnetic coils of the MOL are wrapped.

The magnetic field current results in being less critical for ^{39}Ar than for ^{40}Ar. This can be explained by the different Zeeman-splittings as discussed in section 2.7. In ^{40}Ar the Zeeman-shift for the transition addressed by the counterpropagating laser beam is bigger than for ^{39}Ar. Beyond a certain magnetic field it becomes resonant, such that longitudinally slow atoms are defocussed (left of figure 3.28).

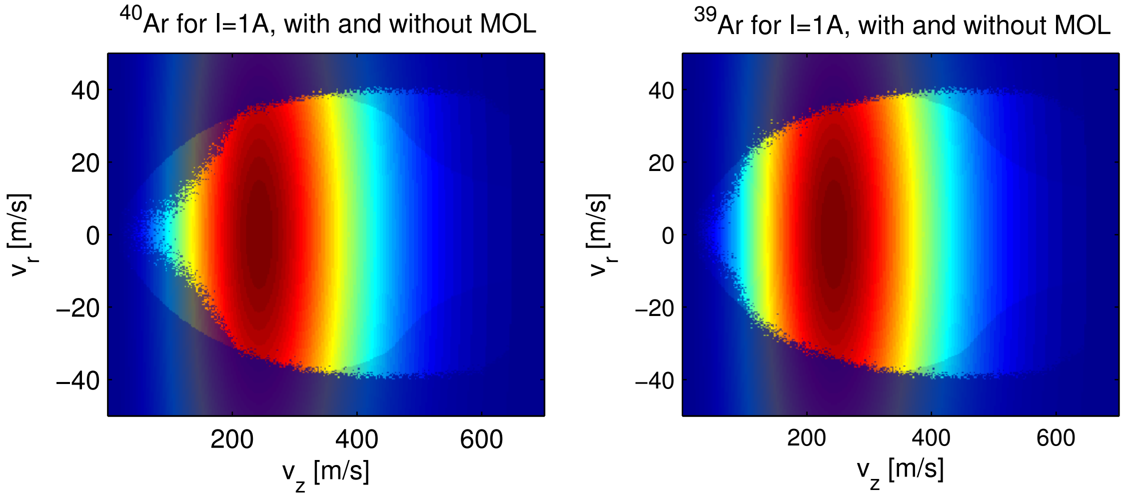

Figure 3.28: Simulated captured velocities for ^{40}Ar (left) and ^{39}Ar (right) with a B-field current of $I = 1$ A. The captured velocities with and without MOL are plotted on top of each other for comparison. The MOL additionally captures atoms with a high longitudinal velocity that have not been entirely collimated in the collimator. Longitudinally slow ^{40}Ar atoms are defocussed because the magnetic field is beyond its optimum. This effect is less severe for ^{39}Ar.

In figure 3.27 it becomes apparent, that the main benefit from the MOL does not result from the focussing of the atom beam but from the reduction of the transverse velocity spread after the collimator. The additional fraction of atoms that reaches the MOT due to the MOL is visible in figure 3.28, where the simulated captured velocities with and without MOL are plotted for comparison. An additional effect is that the transverse velocity spread behind the MOL is smaller than behind the collimator, due to the lower saturation of the MOL-light (figure 3.29).

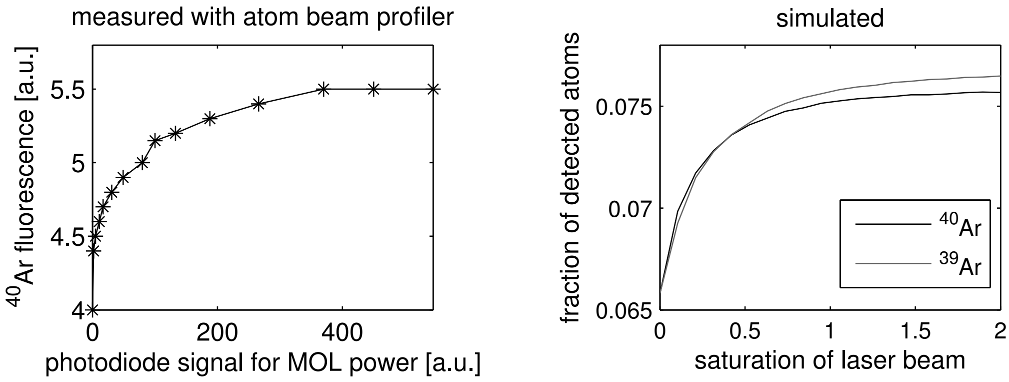

Figure 3.29: Simulated (left) and measured (right) dependence of the fraction of detected atoms on the saturation of the laser beams.

The dependence of the fraction of detected atoms on the MOL detuning is depicted in figure 3.30. For a detuning close to zero, the MOL defocusses the atom beam which is reflected in the simulation as well as in the measurement. The measurement and the simulation also agree in yielding an optimum detuning around −8 MHz. For far detuned laser light, the MOL does not have any effect. Experimentally, the MOL light is diverged from the MOT light, which is detuned by −8.2 MHz.

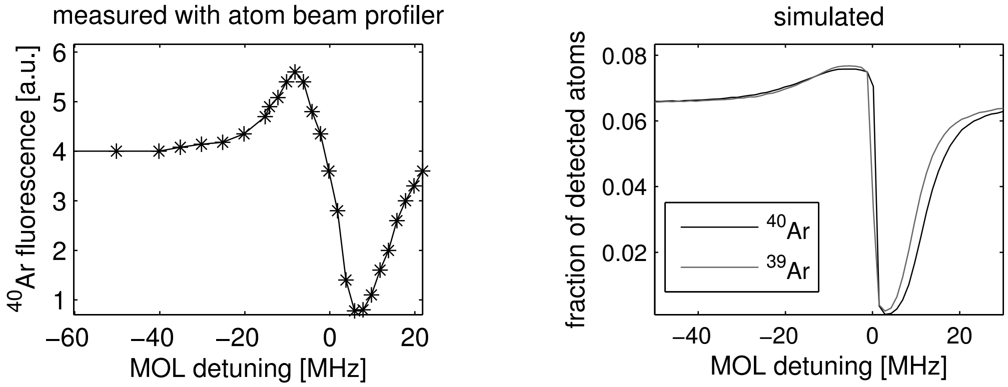

Figure 3.30: Measured (left) and simulated (right) dependence of the fraction of detected atoms on the MOL detuning.

For the experimentally chosen parameters some exemplary trajectories are shown in figure 3.31 for ^{39}Ar and ^{40}Ar. The different Zeeman-splitting of ^{39}Ar and ^{40}Ar as discussed in section 2.7 becomes manifest in the different trajectories.

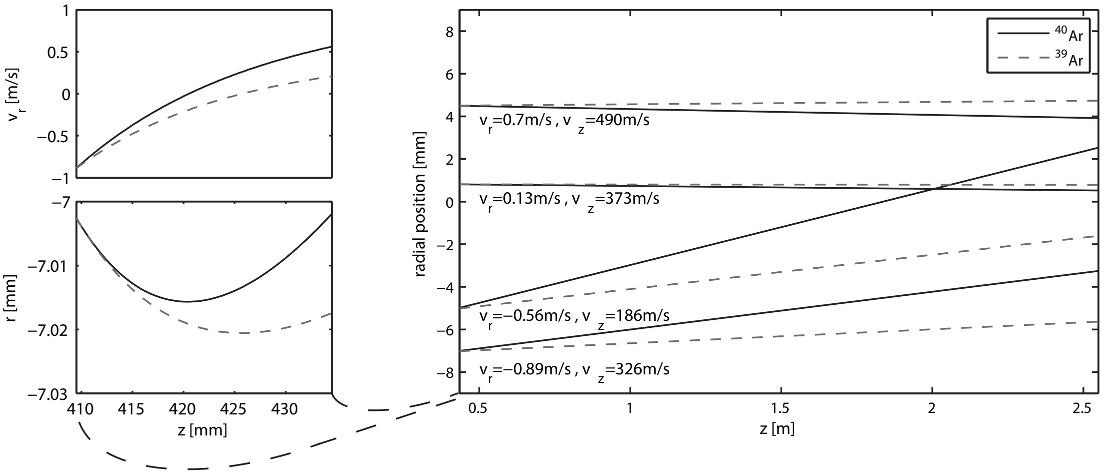

Figure 3.31: Exemplary MOL-trajectories for ^{39}Ar and ^{40}Ar. The trajectories of ^{39}Ar and ^{40}Ar differ due to the different Zeeman-splitting. The insets on the left magnify the MOL region where the actual focussing of the trajectories takes place.

The simulated beam profiles as seen by the atom beam profiler with and without MOL agree with the measured beam profiles (figure 3.32). The focussing effect of the MOL becomes visible in both measurement and simulation.

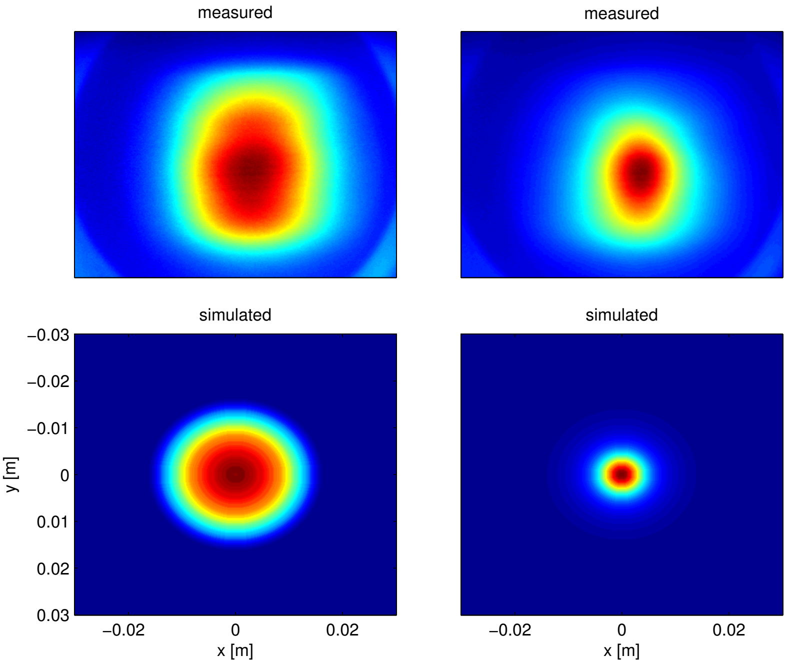

Figure 3.32: Simulated (bottom) and measured (top) beam profiles with and without the MOL. The measured atom beam profiles were recorded with the atom beam profiler.

3.9 Zeeman slower

The collimated and focussed atom beam is longitudinally slowed down to the capture velocity of the MOT by a Zeeman slower[6]. It is based on compensating the changing Doppler shift with the Zeeman shift, which raises the question of whether ^{39}Ar has to be treated differently than ^{40}Ar. Since for the implemented increasing field slower only the $m_F = -11/2 \rightarrow m_F = -13/2$ and $m_J = -2 \rightarrow m_J = -3$ transitions are driven in ^{39}Ar and ^{40}Ar respectively, the same behaviour is expected due to the reasons described in section 2.7.

Once the atom has reached the stretched state, ^{39}Ar can not undergo off-resonant excitations to the $F = 11/2$ state due to the selection rule $\Delta m_F = 0, \pm 1$. Therefore, no repumpers should be necessary which could be confirmed experimentally with enriched samples.

A difference between ^{39}Ar and ^{40}Ar might occur when the Zeeman regime of small magnetic fields is left as is the case at the end of the Zeeman slower. The results in [76] indicate that this effect should not be severe for the magnetic fields occurring in the present Zeeman slower.

A peculiar ingredient of the implemented Zeeman slower is an additional light beam of certain frequency overlapped with the slower beam, for some reason named *Booster*. It forms a second Zeeman slower with the rising slope of the MOT magnetic field (figure 3.33).

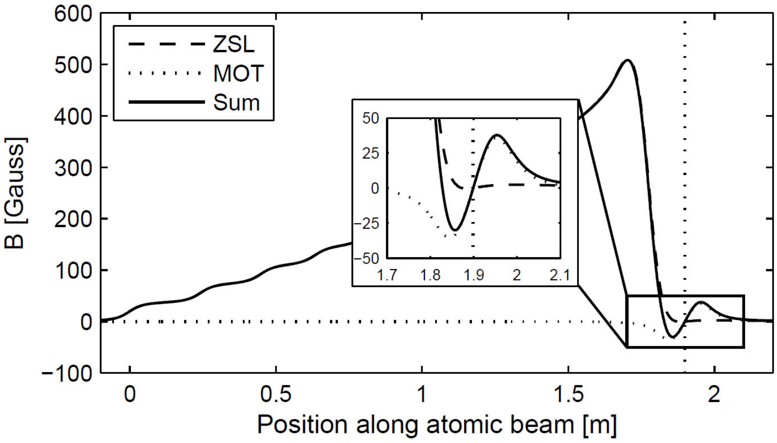

Figure 3.33: Calculated magnetic field of the Zeeman slower and the MOT. The Booster forms a second Zeeman slowing stage with the rising slope of the MOT magnetic field (from [10]).

In this way, the final longitudinal atom velocity of the Zeeman slower can be adjusted higher than the capture velocity of the MOT, which crucially reduces the final divergence of the atom beam at the end of the Zeeman slower. This transverse

---

[6] The Zeeman-slower employed in the experiment is treated in [10] and [75], where the design is described and simulations are performed

broadening of the atom beam due to the Zeeman slowing becomes visible when the atom beam profile is recorded with and without Zeeman slower light (figure 3.34).

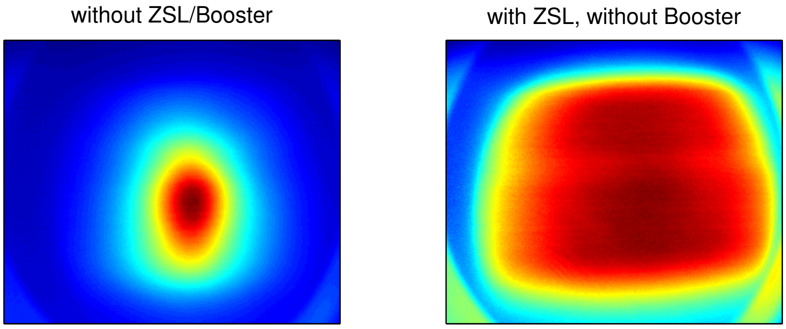

Figure 3.34: Atom beam profiles with and without Zeeman slower light, while the Booster is switched off. The atom beam significantly broadens.

The parameters of the Zeeman slower, such as detunings and magnetic fields, have been optimized with the MOT fluorescence of ^{38}Ar and ^{39}Ar in an enriched sample [5]. As expected, their behaviour in the Zeeman slower is similar and common optima were found for B-field and detuning. The Booster parameters resulted to be slightly different for ^{39}Ar than for ^{40}Ar which is expected since the MOT is involved (see section 2.7).
The implemented magnetic coil geometries leading to the B-field shown in figure 3.33 are depicted in the photograph 3.35.

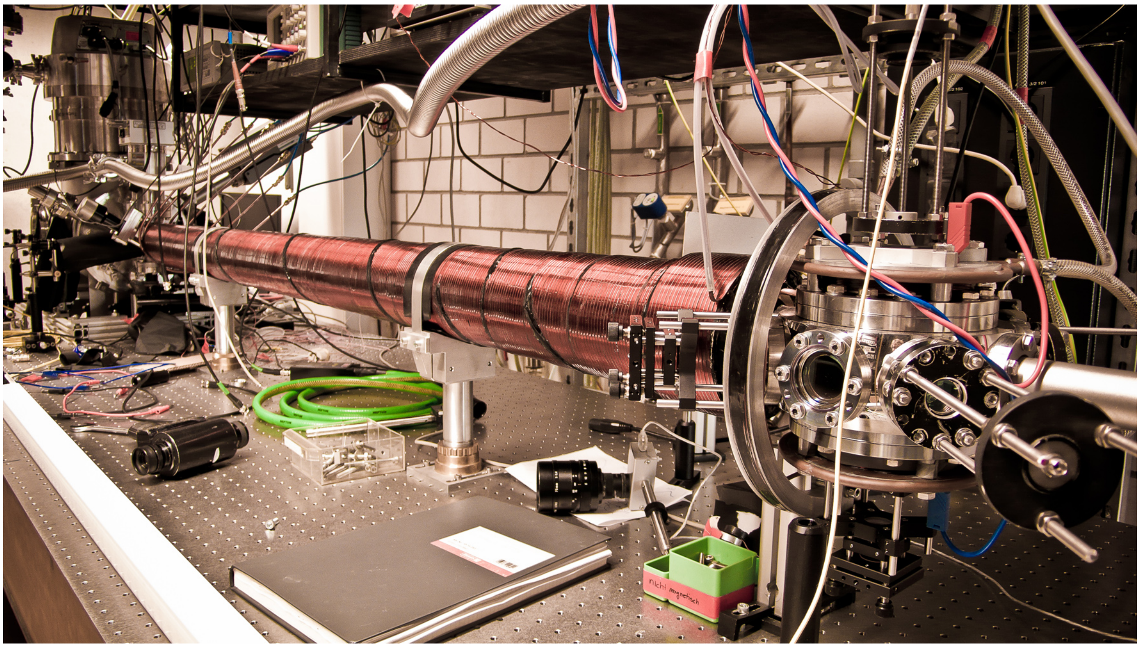

Figure 3.35: Picture of the Zeeman slower together with the adjacent compensation coil and the MOT (from [75]).

3.10 MOT

Once the atoms are decelerated down to the capture velocity of the MOT by the Booster, the atoms are pushed towards the MOT center by the position dependent force exerted by the combination of laser beams and magnetic field[7].

The more red-detuned the MOT beams, the higher the capture velocity, i. e. the more atoms are captured. But the more red detuned, the smaller the scattering rate of atoms in the MOT, i. e. the smaller the single atom signal. Broadening the linewidth by increasing the power of the MOT beams helps, but the background signal due to stray light thereby also increases. The competing interest between loading rate and single atom signal also becomes manifest for the magnetic field. A strong gradient confines the atoms to a smaller region and brings the atoms closer to resonance as soon as they move away from the center. But the weaker the gradient, the more atoms can be captured at the outskirts of the MOT region, especially along the beam axis, where the atoms are slowed down in the outer region of the MOT by the Booster. In this context, it is of relevance that the vertical magnetic field gradient is twice as big as in the horizontal plane, due to the coil geometry visible in figure 3.36 and 3.35.

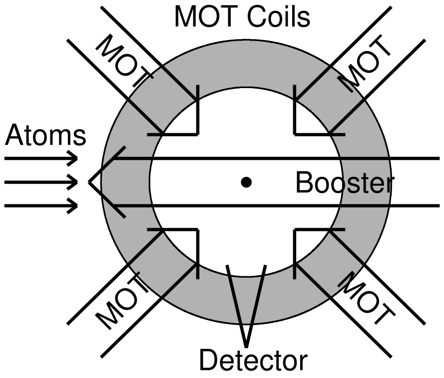

Figure 3.36: Schematic of the MOT setup (from [10]). The MOT beams in the horizontal plane cross the atom beam at an angle of 45°. The vertical MOT beam enters orthogonally to the plane of projection. The magnetic field gradient along the coil axis in the vertical direction is twice as big as in the horizontal plane.

A compromise for these parameters has to be sought, which should be different for ^{39}Ar than for the stable argon isotopes, due its hyperfine nature. Therefore, the ^{39}Ar loading rate in the MOT has been measured for different detunings and magnetic field currents (figure 3.37).

---

[7] Details of the implemented MOT are described in [10] and [75], where simulations are also featured.

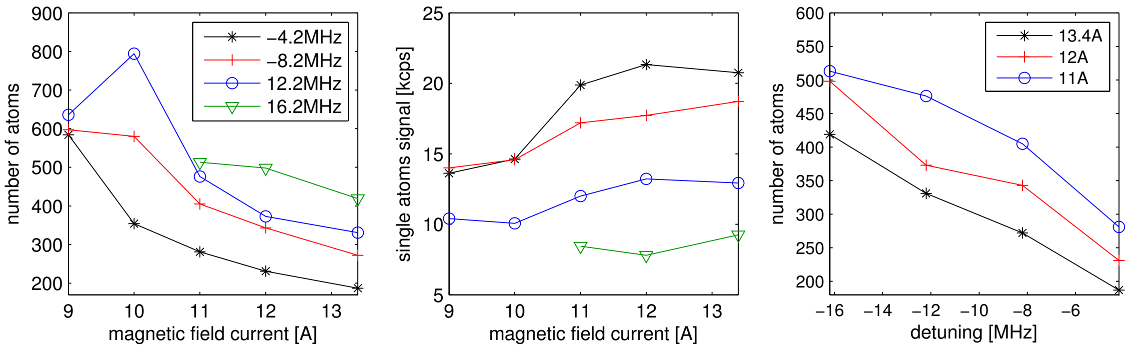

Figure 3.37: Number of ^{39}Ar-atoms in 2 min counted in the MOT (left, right) and single atom signal (middle) for different magnetic field currents and detunings, measured with an enriched sample. The legend of the left plot also applies to the middle plot.

The competing interests of a high loading rate and a high single atom signal are reproduced by the measurements. As a compromise, a current of 11 A and a detuning of −8.2 MHz have been chosen.

The observed trend is also reflected in the calculated acceleration in one dimension as a function of position and velocity, plotted in figure 3.38.

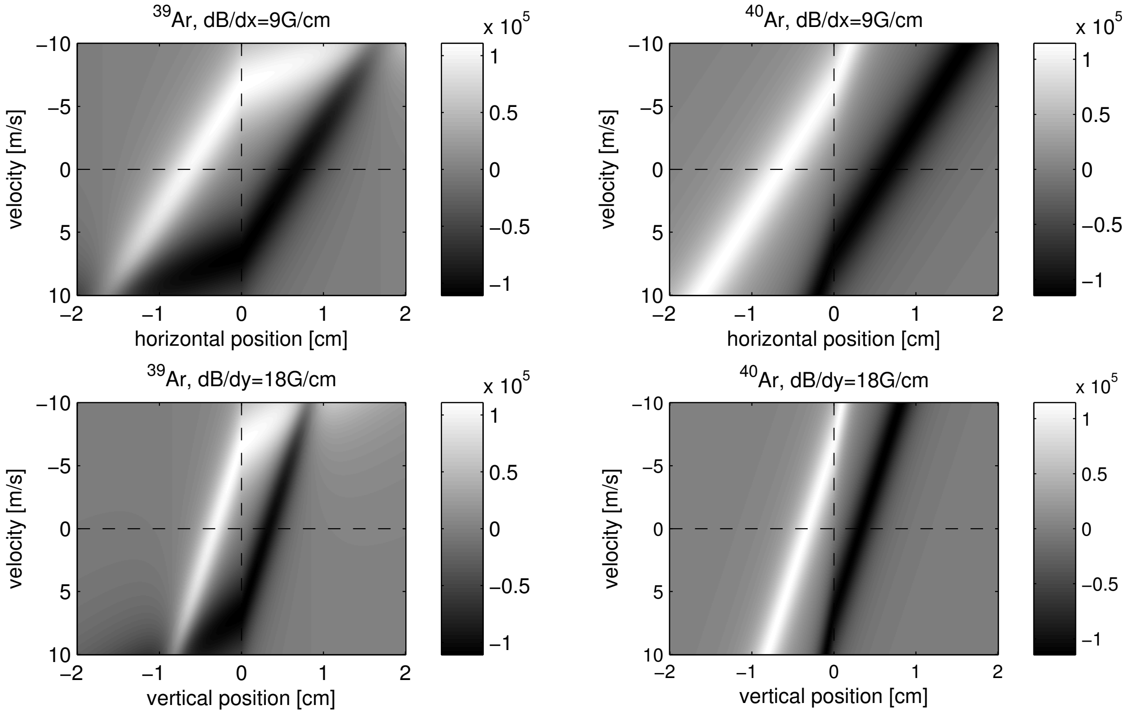

Figure 3.38: Calculated acceleration vs. velocity and position for ^{39}Ar (left) and ^{40}Ar (right). The radial and axial dimension have magnetic field gradients of 9 G/cm (top) and 18 G/cm (bottom) respectively.

The plots reveal, that ^{39}Ar shows a different behaviour from ^{40}Ar in that the MOT does not fulfill its trapping function for atoms that are not in the center and have a velocity of a few meters per second. These are not only not trapped but even worse pushed away. Especially for the vertical dimension, the region in which atoms are captured is confined to the inner centimetre. For the horizontal dimension the capture region is bigger, due to the smaller magnetic field gradient.

The dependence of the capture radius, which is defined here as the position where the acceleration has dropped to almost zero for atoms with zero velocity, on magnetic field gradient and detuning is plotted in figure 3.39.

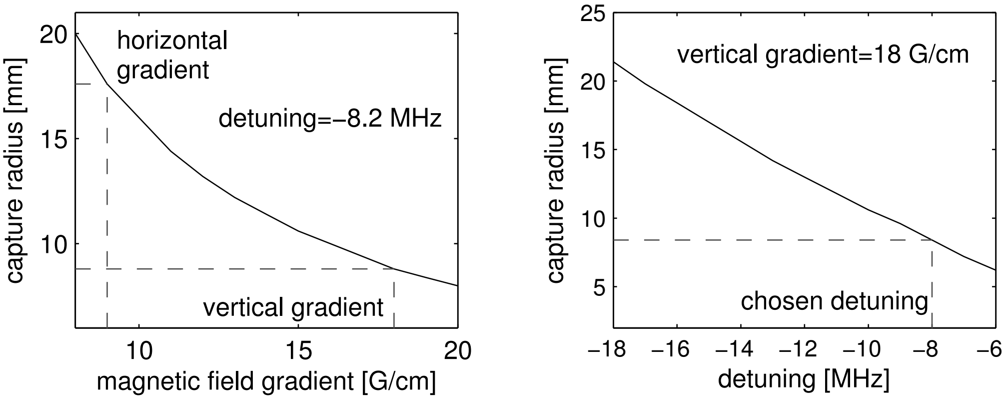

Figure 3.39: Calculated capture radius vs. magnetic field (left) and MOT-detuning (right) for ^{39}Ar.

Figure 3.34 indicates that the slowed atomic beam extends over the entire MOT-region given by the diameter of the laser beams of 32 mm. In principle a capture radius as big as the laser beam radius is desired. For the current experimental parameters expecially the vertical magnetic field axis, which has twice the gradient of the horizontal plane, restricts the capture radius to only 8 mm. The increase in capture radius, which is accompanied by an increase in loading rate, by lowering the magnetic field and going to more negative detuning agrees with the measurements in figure 3.37.

These findings indicate that there is still room for improvement in the capture efficiency of the MOT. A second further red-detuned frequency has been tried out in the MOT to capture atoms in the outer regions as well. Due to technical limitations this method could not be systematically investigated further, but the attempts that have been made indicate an improvement. Changing the geometry of the magnetic coils such that the magnetic field gradient is more homogenous for the dimensions perpendicular to the beam axis, for example with compensation coils, is expected to increase the capture radius of the MOT.

3.11 Laser system

The laser light comprising all the different frequencies necessary for the atom optical components described so far is generated with the laser system schematically illustrated in figure 3.40. A home built external cavity diode laser (ECDL) is frequency-stabilized onto an ^{40}Ar-spectroscopy and serves as a frequency standard for two high power (1 W and 0.5 W) slave lasers, which are formed by commercial MOPA systems. The slave lasers are offset-locked onto the master-laser and are used to generate the cooling and repumper frequencies respectively.

The frequency shifts for the collimator, ZSL and MOT are generated with AOM's in double-pass configuration to allow for frequency tuning. The mating frequencies are overlapped into a fibre and seed home built tapered amplifiers (TA's) for collimator, ZSL and MOT.

The seed light which has a power of several mW is amplified by the TA's up to several hundred mW. The output light is coupled into fibres that guide the light to the corresponding atom optical component at the apparatus, which is placed on a seperate table.

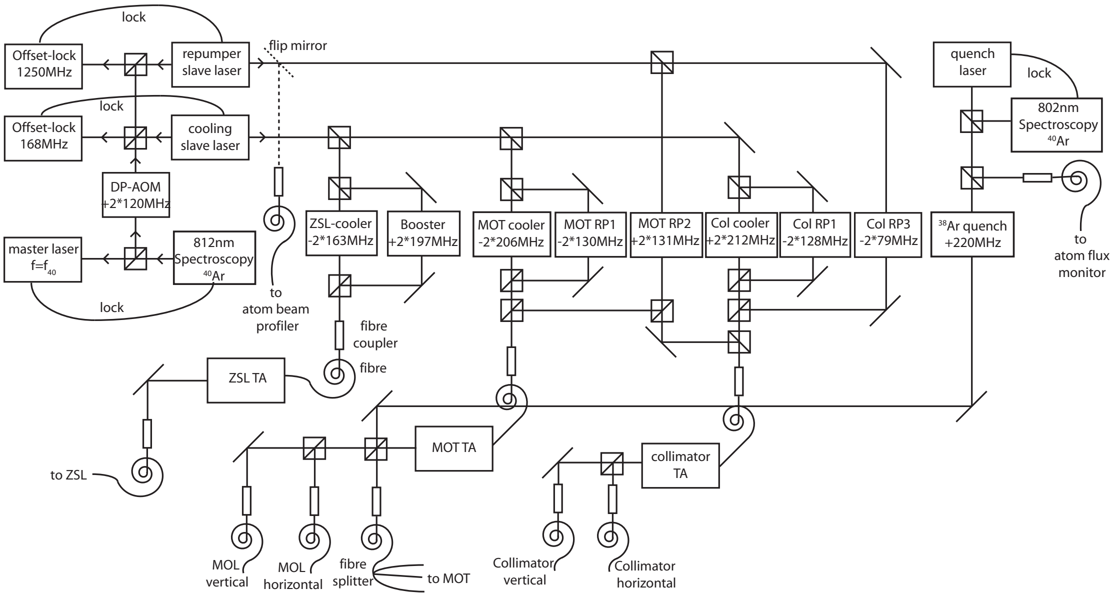

Figure 3.40: Simplified scheme of the laser system

Power ratios between cooler and repumper frequencies of the incoming seed can be adjusted and monitored by a photodiode in the homebuilt TA. For ^{39}Ar measurements these ratios are always adjusted to the same values. The output of the TA's are monitored with a Fabry-Pérot resonator to ensure that all frequencies are amplified as desired (3.41).

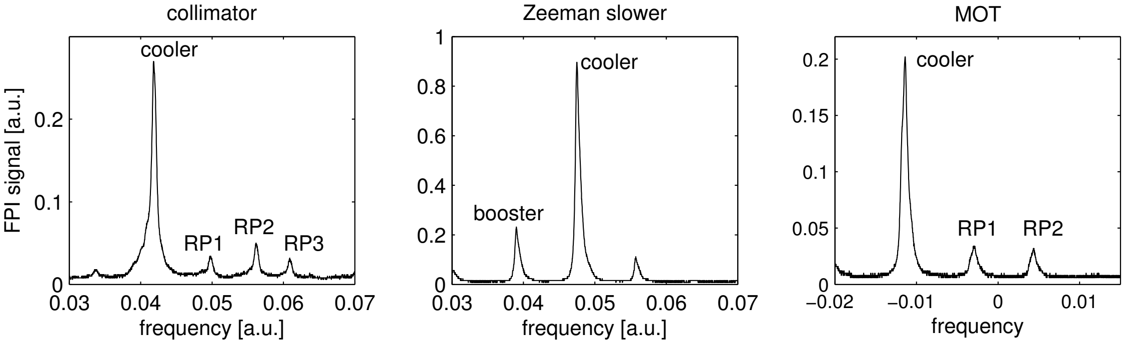

Figure 3.41: Fabry-Pérot images of the TA outputs. The cooling frequencies as well as the repumpers are visible. Interestingly, the booster signal also appears mirrored at the cooling peak as a small feature. The same is observed for the MOT and the collimator but is not visible in the shown plots. It is not clear yet, whether this is merely a feature of the Fabry-Pérot or whether this is in fact a feature of the laser light.

An interesting but open question is, to which extent the overlapping laser beams create an optical beating and whether this could harm the laser cooling processes.

The light for the atom beam profiler is diverged from the repumper-slave laser with a flip mirror and is also guided to the apparatus through an optical fibre.

The 802 nm quench light is produced with a seperate home built ECDL and is stabilized onto a second ^{40}Ar-spectroscopy cell. Part of its light is directly coupled into a fibre for the atom flux monitoring while a fraction is frequency-shifted by an AOM on ^{38}Ar resonance and overlapped into the MOT-fibre for quenching the MOT.

All fibres in the laser setup are polarization maintaining and coupled such that the polarization of the incoming light matches either the slow or the fast axis of the fibre. This is important to assure a stable operation, not just of the MOT or the ZSL, but also of the collimator, which exhibits a dependence on the incoming polarization. The offset lock and the Tapered Amplifier are described in [76].

4 Single atom statististics

^{39}Ar measurements rely on an unambiguous and efficient identification of single ^{39}Ar atoms in the MOT. The detection optics for collecting a maximum fraction of photons from a captured atom while supressing as much stray light as possible is described in the first section[1]. In the section thereafter, a decision rule based on conditioned probabilities is derived for identifying an atom with high confidence under the condition that only a minimum number of trapped atoms is omitted.

4.1 Detection setup

The trapped atoms in the MOT are approximately located in a circular region with a diameter of around 200 µm for ^{39}Ar and 110 µm for ^{40}Ar [10]. This region is imaged 1:1 onto a multimode fibre with a core of 200 µm diameter which is connected to an avalanche photodiode (APD) (see figure 4.1).

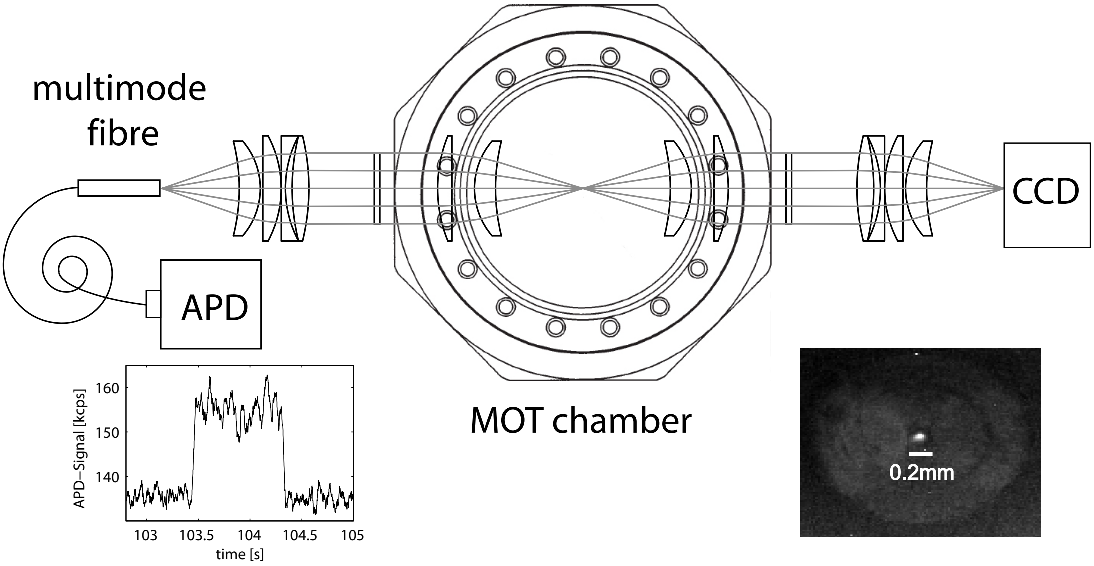

Figure 4.1: Schematic of the imaging system for single atom detection. Due to the imaging geometry a 1:1 image of the fibre head is visible on the CCD camera. The bright outer region originates from the fibre cladding and the dark inner region from the fibre core. The inside of the vacuum chamber is coated with high absorptivity paint and the objectives are enclosed in black tubes for stray light suppression.

---

[1] Further experimental details can be found in [10, 75].

On the opposite side the fluorescence of the trapped atoms is imaged with an identical objective onto a CCD-camera, which provides spatial resolution for the detection of a single atom. Due to the given imaging geometry, a 1:1 image of the fibre head is visible on the CCD camera. The objective has a numerical aperture of $NA = 0.25$, corresponding to around 1.6 % of all emitted photons being collected. Including other losses, such as the quantum efficiency of 0.5 of the APD and the reflective losses at the lenses yield a total photon detection efficiency of 0.0043 for ^{40}Ar and 0.0023 for ^{39}Ar, corresponding to a count rate of ~30 kcps for ^{40}Ar and ~16 kcps for ^{39}Ar, respectively. These estimates are actually close to the measured count rates, which come on top of the background count rate currently being around 180 kcps. The background count rate mainly originates from reflections of the MOT beams on the vacuum windows and to about 20 % on stray light from the Zeeman slower beam. The laser power of each MOT beam is 11 mW which corresponds to a saturation parameter of $s = 1.8$ with a beam waist of 16.5 mm and if the saturation intensity I_s =14.4 W/m^2 for σ-polarization is used. The chosen laser power is a compromise between maximizing the loading rate and keeping the background at tolerable levels. Distinguishing a single atom from background noise with high confidence without omitting too many captured atoms is the subject of the following section.

4.2 Single atom identification

A typical signal of a single atom with a lifetime of 800 ms is depicted in figure 4.1. In general, the probability that a single atom stays captured in the MOT for the time t is governed by collisions with background atoms and can be described by

$$p(t) = \frac{1}{\tau} e^{-t/\tau} \tag{4.1}$$

where τ is the mean lifetime of a single atom in the MOT, that was already introduced for the MOT loading rate in section 3.4. Without leakage due to inefficient repumping, the mean lifetime mainly depends on the pressure in the MOT chamber. For the current experimental parameters, the mean lifetime has been determined to be $\tau = 520$ ms with an ^{39}Ar enriched sample by measuring the lifetime of almost thirty thousand atoms (figure 4.2).

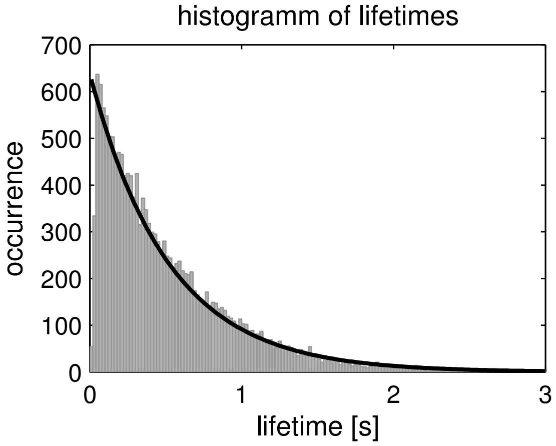

Figure 4.2: Histogram with a binning of 20 ms over the lifetimes of 29 488 ^{39}Ar atoms measured with an enriched sample. The fitted curve based on (4.1) yields a mean lifetime of $\tau = 520\,\mathrm{ms}$. For atoms with a lifetime below 40 ms the histogram decreases, because the fidelity for atom detection decreases.

The probability for k atoms in the MOT exhibits a Poissonian character and can be expressed as [86]

$$P_{\mathrm{at}}(k) = \frac{\bar{k}^k}{k!} e^{-\bar{k}} \tag{4.2}$$

with the mean number of atoms in the trap

$$\bar{k} = R \cdot \tau \tag{4.3}$$

that includes the ^{39}Ar loading rate R. The following considerations are restricted to atmospheric measurements for which a count rate of $R_0 = 3.6\,\mathrm{atoms/h}$ has been determined, as will be described later[2]. Together with the mean lifetime this yields a mean atom number in the MOT of

$$\bar{k} = 0.001\ . \tag{4.4}$$

In atmospheric ^{39}Ar measurements, the probability for more than one atom in the MOT can be neglected, such that only

$$P_{\mathrm{at}}(0) = e^{-\bar{k}} \quad \text{and} \quad P_{\mathrm{at}}(1) = \bar{k} e^{-\bar{k}} \tag{4.5}$$

have to be taken into account.

---

[2] It is somewhat sloppy to introduce the count rate already at this point, although it is theoretically determined with the threshold criterion derived hereafter. However, the error made in doing so is negligible. Moreover, it has to be pointed out, that for samples with a lower count rate the threshold criterium also changes. Again, the error made by this is small such that the following considerations remain valid for samples with a different count rate as well.

Threshold for atoms with a fixed lifetime

As visible in figure 4.1, the APD-signal consists of a background signal and a single atom signal. The probability that n photons are detected in a detection time T if no atom is trapped is

$$P(n|0) = \frac{\bar{n}^n}{n!} e^{-\bar{n}} \approx \frac{1}{\sqrt{2\pi n_0}} e^{\frac{-(n-n_0)^2}{2n_0}} \;, \tag{4.6}$$

where the Poisson distribution has been approximated by a normal distribution with continuous mean and variance n_0.
Likewise, the probability that n photons are detected in a detection time T if an atom with a lifetime longer than T is trapped becomes

$$P(n|1) = \frac{1}{\sqrt{2\pi}\sigma_1} e^{\frac{-(n-n_1)^2}{2\sigma_1^2}} \;. \tag{4.7}$$

The mean number of detected photons if an atom is trapped

$$n_1 = n_0 + \Delta n \tag{4.8}$$

includes the mean photon contribution Δn from the single atom. Since the noise of the background and the single atom signal are uncorrelated, the standard deviation for the single atom signal becomes

$$\sigma_1 = \sqrt{n_0 + \Delta n} \;. \tag{4.9}$$

The probability $P(n|1)$ in expression (4.7) is only true for atoms with a lifetime equal to the detection time T. For this paragraph, it is assumed that this is the case for all atoms. Based on the expressions derived within that assumption, the general case will be treated thereafter.

The probability $P(n)$ that n photons are detected is comprised by the probability $P(n|0)$ that n photons are detected when no atom is in the trap and of the probability $P(n|1)$ that n photons are detected if one atom is in the trap. These two probabilities have to be weighted with the probabilities $P_{\text{at}}(0)$ and $P_{\text{at}}(1)$ that no atom or one atom is in the trap respectively, yielding

$$P(n) = P(n|0)P_{\text{at}}(0) + P(n|1)P_{\text{at}}(1) \;. \tag{4.10}$$

This formula conforms with the atmospheric ^{39}Ar measurement shown in figure 4.3 for a detection time of $T = 40\,\text{ms}$.

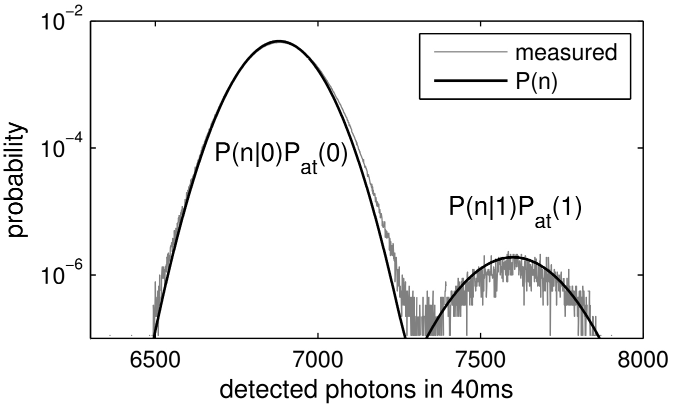

Figure 4.3: Histogram of detected photons for a 3 h atmospheric ^{39}Ar measurement with a detection time of 40 ms. The measured histogram is only marginally broader than the profile calculated with expression (4.10). The mean number of background photons is $n_0 = 6880$ and the mean number of photons if a single atom is trapped is $n_1 = 7600$.

The following considerations are aimed at finding a threshold $\hat{n}$ for the number of detected photons, to decide whether a photon signal originates from an atom or not. The threshold has to assure a high confidence in order not to count background noise as an atom. The probability that an atom is in the trap when n photons have been detected can be derived from equation 4.10 as[3]

$$P(1|n) = \frac{P(n|1)P_{\text{at}}(1)}{P(n)} \tag{4.11}$$

which in general form is known as *Bayes' theorem* .
Correspondingly, the probability that no atom is in the trap if n photons have been detected is

$$P(0|n) = \frac{P(n|0)P_{\text{at}}(0)}{P(n)} = 1 - P(1|n) \; . \tag{4.12}$$

In order to find an **optimum threshold** $\hat{n}$, a compromise has to be found between

- $P(1|\hat{n})$ = minimum probability that a counted atom is really an atom.
- $P(0| > \hat{n})$ = probability to count background noise as an atom.
- $P(< \hat{n}|1)$ = fraction of atoms that is not counted because not enough photons are detected.

---

[3] The term $P(a|b)$ is denoted in terms of conditioned probability, meaning $P(a|b)$ *is the probability for a under the condition of b.*

These terms can be calculated using the expressions given above. The probability that an atom is in the trap when $\hat{n}$ photons have been detected becomes

$$P(1|\hat{n}) = \frac{\bar{k}\sqrt{n_0}\; e^{\frac{-(\hat{n}-n_1)^2}{2\sigma_1^2}}}{\sigma_1 e^{\frac{-(\hat{n}-n_0)^2}{2n_0}} + \bar{k}\sqrt{n_0}\; e^{\frac{-(\hat{n}-n_1)^2}{2\sigma_1^2}}} \ . \tag{4.13}$$

The probability $P(0| > \hat{n})$ that no atom is in the trap if more than $\hat{n}$ photons have been detected is obtained by integration

$$\begin{aligned} P(0| > \hat{n}) &= \frac{P_{\mathrm{at}}(0) \cdot P(> \hat{n}|0)}{P(> \hat{n})} = \frac{P_{\mathrm{at}}(0) \cdot \int_{\hat{n}}^{\infty} P(n|0)dn}{\int_{\hat{n}}^{\infty} P(n)dn} \\ &= \frac{\mathrm{erfc}\left(\frac{\hat{n}-n_0}{\sqrt{2n_0}}\right)}{\mathrm{erfc}\left(\frac{\hat{n}-n_0}{\sqrt{2n_0}}\right) + \bar{k}\ \mathrm{erfc}\left(\frac{\hat{n}-n_1}{\sqrt{2n_0}}\right)} \ . \end{aligned} \tag{4.14}$$

Likewise, the probability $P(< \hat{n}|1)$ that less than $\hat{n}$ photons are detected if one atom is in the trap becomes

$$P(< \hat{n}|1) = \int_{-\infty}^{\hat{n}} P(n|1)dn = \frac{1}{2}\mathrm{erfc}\left(\frac{n_1 - \hat{n}}{\sqrt{2}\,\sigma_1}\right) \ . \tag{4.15}$$

A schematic illustration of the probabilities entering into the foregoing calculations is given in figure 4.4.

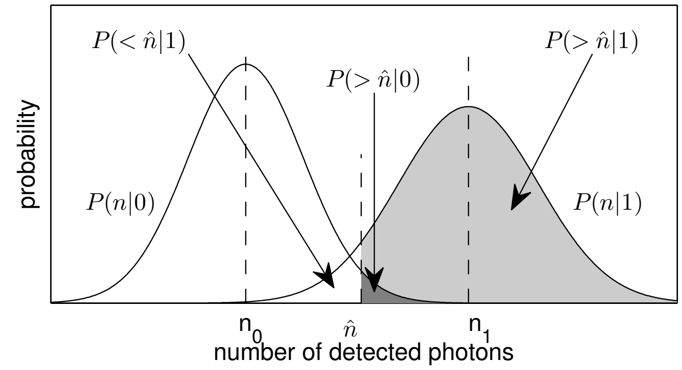

Figure 4.4: Sketch of the different probabilites entering into the single atom identification. The two normal distributions are drawn close to each other for illustrative reasons and do not correspond to figure 4.3.

$P(1|\hat{n})$, $P(0| > \hat{n})$ and $P(< \hat{n}|1)$ are plotted in figure 4.5 for different thresholds, that are expressed with respect to the standard deviation of the background, i. e.

$$\hat{x} = \frac{\hat{n} - n_0}{\sqrt{n_0}} \ . \tag{4.16}$$

A sharp increase for $P(1|\hat{n})$ occurs around a threshold of $5\sigma_0$. While for a threshold of $4\sigma_0$ the confidence that a signal with $\hat{n}$ photons is really an atom is almost zero, it is already bigger than 99.9 % for a threshold of $6\sigma_0$. The total fraction of falsely counted atoms $P(0| > \hat{n})$ is already going down for smaller thresholds reflecting that although the minimum probability $P(1|\hat{n})$ for a signal to be an atom might be low, the entire fraction of false atoms can still be small. The fraction of omitted atoms $P(< \hat{n}|1)$ starts to become significant for thresholds bigger than $6\sigma_0$.

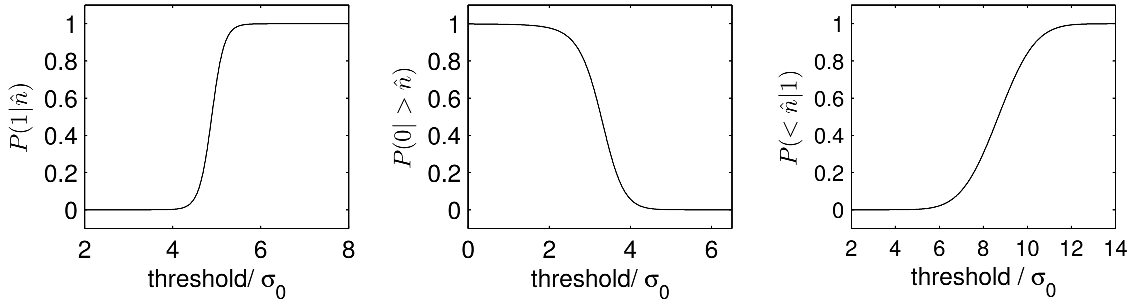

Figure 4.5: Probabilites $P(1|\hat{n})$, $P(0| > \hat{n})$ and $P(< \hat{n}|1)$ calculated as a function of the threshold. The threshold is expressed in terms of the standard deviation σ_0 of the background.

Based on the explicit values given in table 4.1, a threshold of $6\sigma_0$ seems a reasonable choice, for which only two atoms out of a million are false and only 2 % of the trapped atoms are not counted.

Table 4.1: Probabilities for single atom identification with an integration time of 40 ms.

threshold $\hat{x}$	$P(1\|\hat{n})$	$P(0\| > \hat{n})$	$P(< \hat{n}\|1)$
1	$3.16 \cdot 10^{-11}$	0.997	$3.25 \cdot 10^{-9}$
3	$3.54 \cdot 10^{-6}$	0.722	$8.86 \cdot 10^{-6}$
5	0.69	0.17	$5.5 \cdot 10^{-4}$
6	0.9997	$1.9 \cdot 10^{-6}$	0.02
7	$1 - 1.3 \cdot 10^{-7}$	$2.74 \cdot 10^{-9}$	0.10
8	$1 - 3.67 \cdot 10^{-11}$	$1.72 \cdot 10^{-12}$	0.3

However, the foregoing considerations were explicitly made for a detection time of 40 ms. Strictly speaking, the derived threshold criterion only applies to atoms with a lifetime of 40 ms. For shorter-lived atoms not as many photons are detected. If they are included for a $6\sigma_0$ threshold, $P(0| > \hat{n})$ stays roughly the same but the fraction of omitted atoms becomes $P(< \hat{n}|1) = 0.057$, which is more than twice the above value although still acceptably small.

For atoms with a longer lifetime, the reduction to a detection time of 40 ms is too restrictive. A higher fidelity can be achieved if the detection time is as long as the atom's lifetime, such that all detected photons from the atom are taken into account. The probability that a total of Δn photons from a single trapped atom is obtained by weighting expression (4.7) with the distribution of the lifetimes given in (4.1) yielding

$$\frac{1}{\tau}\frac{1}{\sqrt{2\pi\Delta n_1(t)}}\int_0^\infty e^{\frac{-[\Delta n-\Delta n_1(t)]^2}{2\Delta n_1(t)}}\cdot e^{-t/\tau}dt \tag{4.17}$$

which is plotted in figure 4.6. The detected mean number of photons from one atom

$$\Delta n_1 = \Delta\gamma_1 \cdot t \tag{4.18}$$

is expressed as a function of time with the rate

$$\Delta\gamma_1 = \gamma_1 - \gamma_0 = \frac{7600\,\mathrm{photons}}{40\,\mathrm{ms}} - \frac{6880\,\mathrm{photons}}{40\,\mathrm{ms}} = 18\,\frac{\mathrm{kcounts}}{\mathrm{s}} \tag{4.19}$$

obtained from figure 4.3.

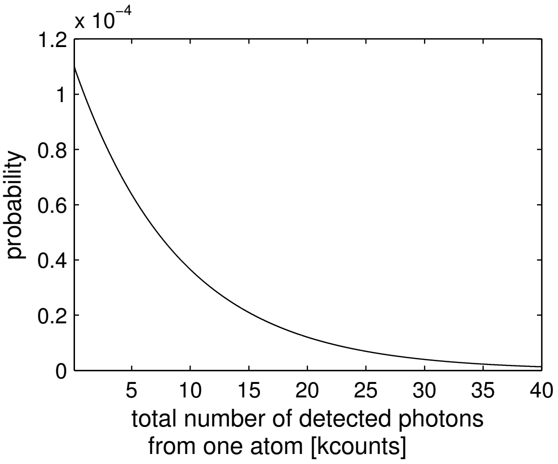

Figure 4.6: Probability of detecting a total of Δn photons from a single atom is trapped including the lifetime distribution. The mean number of detected photons amounts to 8424.

In order to obtain maximum statistics, a threshold criterion has to take into account all detected photons from a single atom. Depending on the number of detected photons, i. e. depending on the lifetime of the single atom, the threshold has to adapt, in order to reach the same confidence level for all counted atoms. Such an adaptive threshold as a function of the lifetime is derived in the following.

Threshold adapted to the lifetime

In order to obtain the optimum threshold as a function of the lifetime for a given minimum confidence, the upper expressions for the probabilities are written in terms of the relative deviation from the background according to the transformation

$$x(t) = \frac{n(t) - n_0(t)}{\sqrt{n_0(t)}} \ . \tag{4.20}$$

In that frame, the mean number of background counts $n_0(t)$ becomes

$$x_0 = 0 \tag{4.21}$$

while the mean number of counts $n_1(t)$ if an atom is trapped transforms to

$$x_1(t) = \frac{n_1(t) - n_0(t)}{\sqrt{n_0(t)}} \ . \tag{4.22}$$

The corresponding standard deviations likewise change to

$$s_0 = 1 \quad , \quad s_1 = \frac{\sigma_1}{\sigma_0} = 1 + \sqrt{\frac{\gamma_1 - \gamma_0}{\gamma_0}} \ . \tag{4.23}$$

Furthermore, the detection time is chosen equal to the lifetime of the atom, such that all photons are taken into account. In this framework, the probability that $n_0 + x\sigma_0$ photons are detected if no atom is trapped becomes

$$P(x|0) = \frac{1}{\sqrt{2\pi}} e^{\frac{-x^2}{2}} \ . \tag{4.24}$$

Likewise, the now time-dependent probability that $n_0 + x\sigma_0$ photons are detected if an atom with lifetime t is trapped is

$$P(x|1,t) = \frac{1}{\sqrt{2\pi}\, s_1} e^{\frac{-[x - x_1(t)]^2}{2s_1^2}} \ . \tag{4.25}$$

For the probability that no atom is trapped if $n_0 + x\sigma_0$ photons are detected, the time-independent expression

$$P(0|x) = \frac{e^{\frac{-x^2}{2}}}{e^{\frac{-x^2}{2}} + \frac{\bar{k}}{\tau s_1} \int_0^\infty e^{\frac{-[x - x_1(t)]^2}{2s_1^2}} e^{-t/\tau} dt} \tag{4.26}$$

is obtained. The probability that an atom is trapped if $n_0 + x\sigma_0$ photons are detected and if the considered lifetime is t becomes

$$\begin{aligned} P(1|x,t) &= \frac{P(x|1,t) \cdot P_{\text{at}}(1)}{P(x|0) \cdot P_{\text{at}}(0) + P(x|1,t) \cdot P_{\text{at}}(1)} \\ &= \frac{\bar{k}\, e^{\frac{-[x - x_1(t)]^2}{2s_1^2}}}{s_1 e^{\frac{-x^2}{2}} + \bar{k}\, e^{\frac{-[x - x_1(t)]^2}{2s_1^2}}} \ . \end{aligned}$$

For a given threshold $\hat{x}$, the probability that no atom is in the trap if more than $n_0 + \hat{x}\sigma_0$ photons have been detected reads

$$P(0| > \hat{x}) = \frac{\operatorname{erfc}\left(\frac{\hat{x}}{\sqrt{2}}\right)}{\operatorname{erfc}\left(\frac{\hat{x}}{\sqrt{2}}\right) + \frac{\bar{k}}{\tau s_1}\int_0^\infty \operatorname{erfc}\left(\frac{\hat{x}-x_1(t)}{\sqrt{2}}\right) e^{-t/\tau} dt} \tag{4.27}$$

where it has been integrated over all lifetimes.
The probability that less than $n_0+\hat{x}\sigma_0$ photons are detected if one atom with lifetime t is in the trap becomes

$$P(< \hat{x}|1,t) = \frac{1}{2}\operatorname{erfc}\left(\frac{x_1(t) - \hat{x}}{\sqrt{2}\, s_1}\right) \ . \tag{4.28}$$

From this, the total fraction of uncounted atoms, i. e. the probability that less than $n_0 + \hat{x}\sigma_0$ photons are detected if an atom is trapped, can be calculated from the integral

$$\frac{1}{\tau}\int_0^\infty P(< \hat{x}|1,t)\ e^{-t/\tau} dt \ . \tag{4.29}$$

The different probabilities are plotted versus lifetime in figure 4.7 for a threshold of $6\sigma_0$. The confidence $P(1|\hat{x},t)$ for identifying an individual atom is rather constant for atoms with a lifetime of 5–60 ms. For longer living atoms, the threshold is actually too low, for their mean number of detected photons is way higher than the background. The fraction of lost atoms $P(< \hat{x}|1,t)$ becomes significant already for atoms below a lifetime of 30 ms. The fraction of falsely detected atoms computes to $P(0| > \hat{x}) = 1.97 \cdot 10^{-6}$.

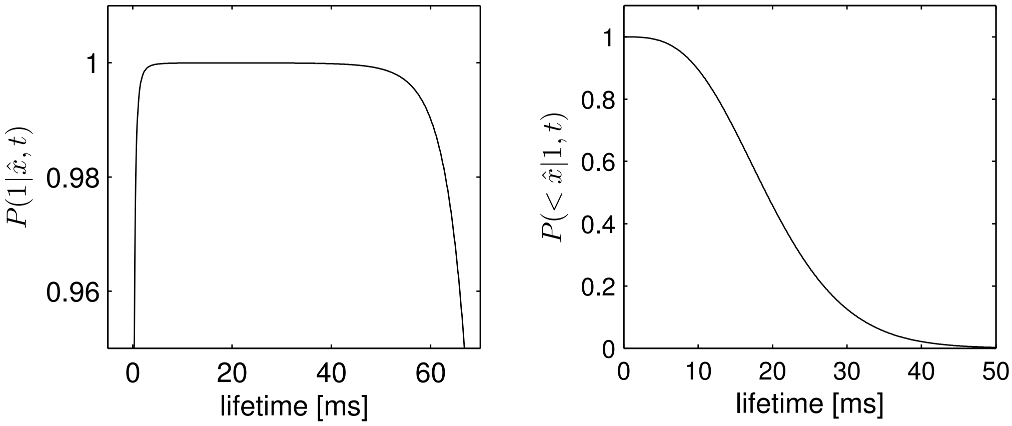

Figure 4.7: Figure of probabilities vs. lifetime for a threshold of $6\sigma_0$.

In order to assure the same confidence $P(1|\hat{x},t)$ for each individual atom while keeping the lost fraction of atoms $P(< \hat{x}|1,t)$ at a minimum, the threshold has to be adapted to the lifetime. The time-dependent threshold $\hat{x}(t)$ calculated under the conditions that $P(1|\hat{x}(t),t) \geq 99.9\%\ \forall t \in (0,\infty)$ and that $P(<\hat{x}(t)|1,t)$ is minimal, is plotted in figure 4.8.

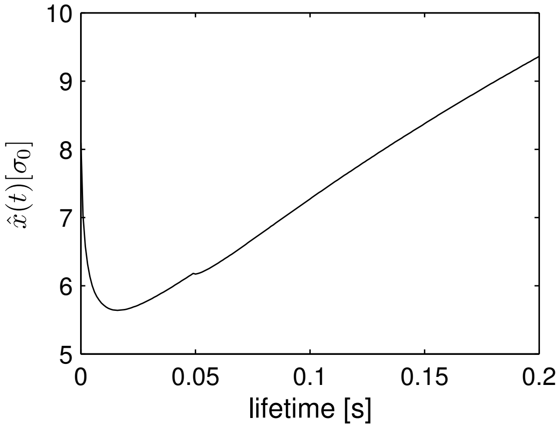

Figure 4.8: Adaptive threshold $\hat{x}(t)$ vs. lifetime of the atom, calculated under the condition that $P(1|\hat{x}(t),t) \geq 99.9\%$ and that $P(<\hat{x}(t)|1,t)$ is minimal. For a lifetime of 16 ms the threshold becomes equal to the mean signal if a single atom is trapped, i. e. $\hat{x} = x_1$, such that the threshold has to increase again to maintain the confidence level. The little kink results from the discrete numerical calculation of the threshold.

Above a lifetime of 16 ms, where $\hat{x} = x_1$, the threshold increases for longer lifetimes since the mean number of detected photons $n_1(t)$ is increasing.
The probabilities resulting from the lifetime-dependent threshold are depicted in figure 4.9.

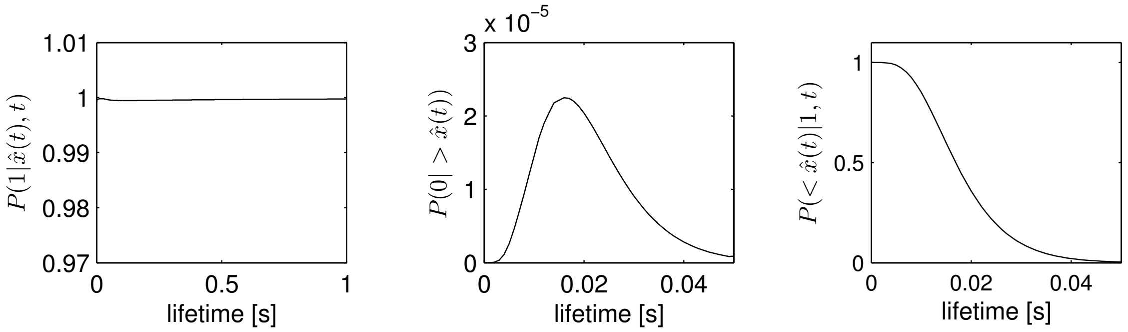

Figure 4.9: Probabilities vs. lifetime for the adaptive threshold $\hat{x}(t)$. $P(1|\hat{x}(t),t) > 99.9\%$ for all lifetimes as required (left). The fraction of false counts $P(0|>\hat{x}(t))$ is below $3 \cdot 10^{-5}$ for all lifetimes but exhibits a maximum for atoms with a lifetime of around 16 ms, coinciding with the minimum of $\hat{x}(t)$ in figure 4.8.

The minimum of the threshold at a lifetime of 16 ms is also manifest in the fraction of falsely counted atoms $P(0|>\hat{x}(t))$, where $\hat{x}(t)$ enters as the lower integration limit

of the background distribution.
The fraction of captured atoms, that is not counted since not enough photons are detected from them is

$$\frac{1}{\tau}\int_0^\infty P(<\hat{x}(t)|1,t)e^{-t/\tau}dt = 0.037 \tag{4.30}$$

The total fraction of falsely counted atoms accordingly amounts to

$$\frac{1}{\tau}\int_0^\infty P(0|>\hat{x}(t))e^{-t/\tau}dt = 9.11\cdot 10^{-7} \tag{4.31}$$

These values are a little better than the ones obtained for a fixed threshold of $6\sigma_0$ at a fixed detection time of 40 ms, that were already quite satisfactory. Still, for atoms with short lifetimes, the adaptive threshold can contribute significantly to the confidence level.
The derived formalism implies the following **decision rule for the identification of an atom:**

> If for any detection time t the number of detected photons is bigger than the time dependent threshold, i. e. $x > \hat{x}(t)$, then the signal is counted as an atom.

Practically, this decision rule is implemented as a running average filtering a time frame of ten minutes as a function of the averaging time. For each averaging time t a signal that is higher than $\hat{x}$ is counted as an atom. As an example, figure 4.10 illustrates this algorithm for a typical atom.

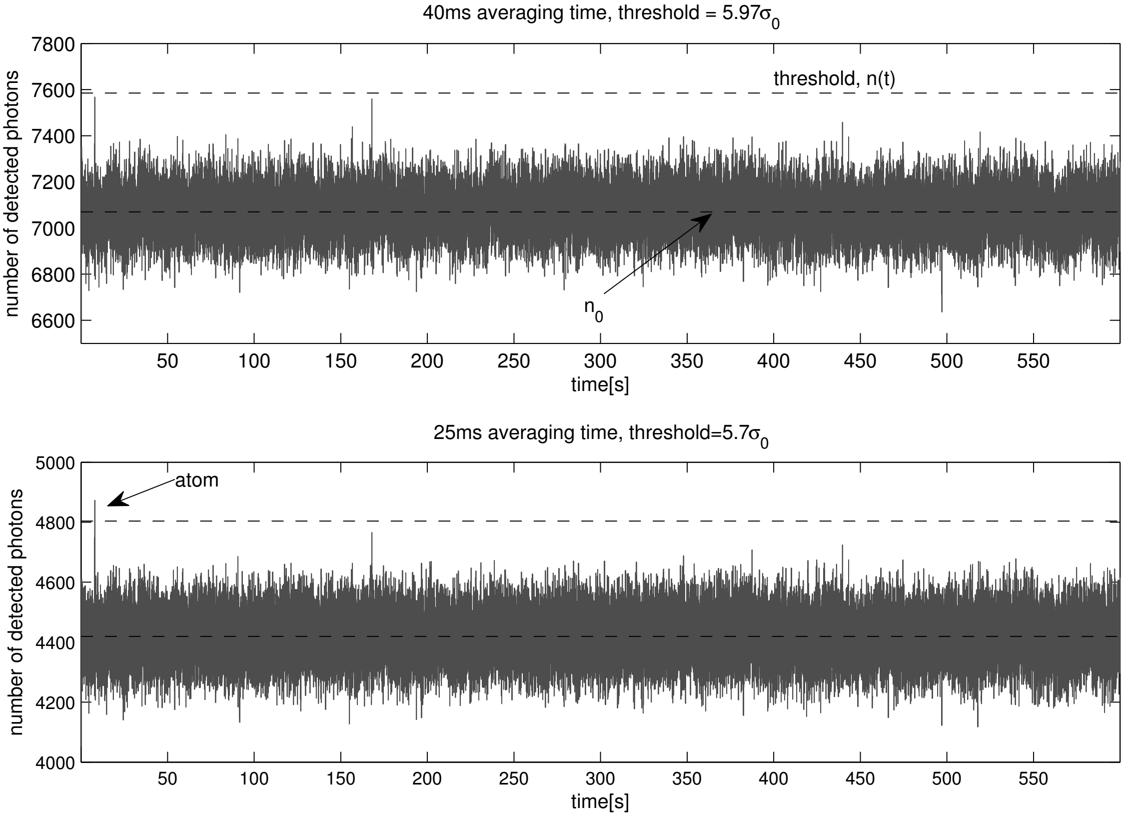

Figure 4.10: An example of single atom identification: For an averaging time of 40 ms and the corresponding threshold $\hat{x}(40\,\mathrm{ms}) = 5.97\sigma_0$, no atom is counted (upper plot). For an averaging time of 25 ms and a threshold $\hat{x}(25\,\mathrm{ms}) = 5.7\sigma_0$, one atom is counted (lower plot). The second peak instead is not higher than the threshold for any averaging time.

The presented atom identification algorithm with the APD is satisfactory, in that less than 4 % of the atoms are not counted and only one atom out of a million is false. However, a different type of fake atoms can be produced for example by spikes on the laser power of the MOT beams, by a spike on the frequency of the ^{40}Ar-quench or by cosmic muons impinging on the APD. Such events are not covered by the derived statistics and are in general difficult to identify with the APD. Moreover, if the center of the MOT was shifted out of the APD focus during a measurement the atoms could not be detected. Due to these reasons, the CCD-camera providing spatial resolution is additionally employed to exclude fake signals and to monitor the single atom position.

A typical image for a single atom signal on the CCD is shown in figure 4.1. Continuously recording the camera signal would lead to gigantic amounts of data considering that one ^{39}Ar measurement takes 10–30 h. Therefore, the camera only stores data to the memory when it is triggered by the APD. Otherwise, it continuously overwrites the temporary memory with the images recorded during the last 4 s.

In this way, a video for each single atom candidate is recorded. In order to obtain videos for all possible candidates, the APD threshold for triggering the camera is lower than the threshold for atom identification.

The camera can identify whether an atom-like signal on the APD originates for example from a spike in laser intensity, which is visible not only in the MOT center but also everywhere else. However, the camera does not significantly increase the already high fidelity for single atom detection reached with the APD. For atoms with short lifetimes less than 40 ms, where the APD would benefit from assistance, the camera does not help since its repetition rate is limited to about 10 Hz at the sensitivity needed for single atom detection.

The background offset due to ^{40}Ar atoms that scatter light on their transit through the MOT could be reduced with the ^{40}Ar quench that transfers the metastable ^{40}Ar atoms out of their metastable state behind the MOL (figure 4.11).

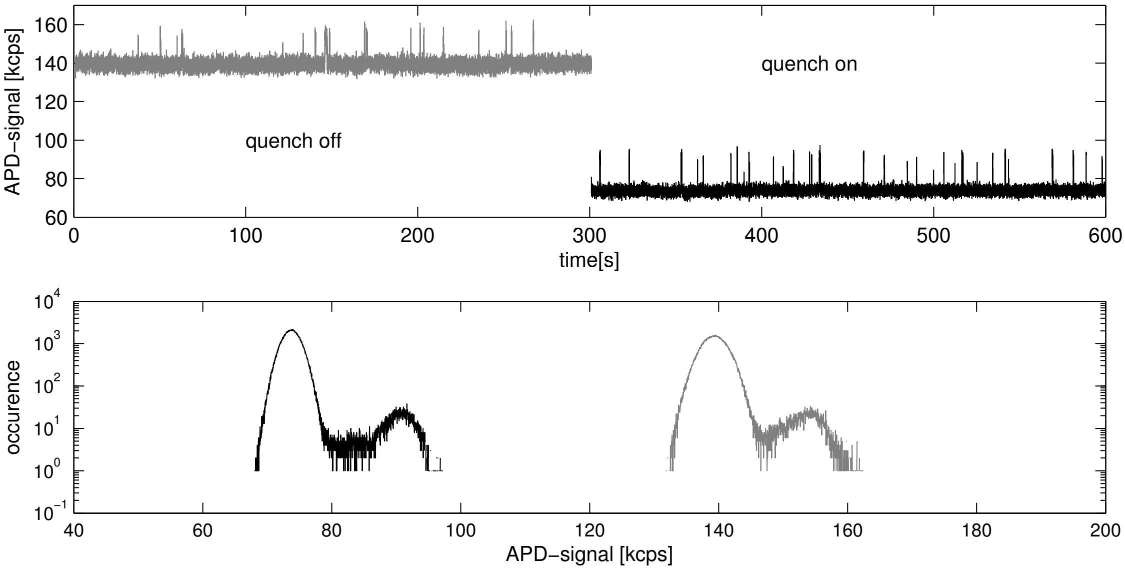

Figure 4.11: Suppression of the ^{40}Ar background with the ^{40}Ar quench. Top) Time trace of the APD-signal with (black) and without (gray) quench. Bottom) The better seperation of the single atom from the background peak due to the background reduction becomes apparent in the histogram.

The biggest potential in further increasing the single atom detection fidelity lies in reducing the background stray light, for example by replacing the partly stained windows of the MOT chamber by new ones with a special AR coating centered around 812 nm.

5 Dating of groundwater with ^{39}Ar-ATTA

The experimental developments and optimizations in the presented ^{39}Ar-ATTA setup led to an improvement in the ^{39}Ar count rate which allows for dating of groundwater. The crucial question when it comes to dating of water with ^{39}Ar-ATTA is, how to translate the measured ^{39}Ar count rate for a sample into an age. Extensive experimental efforts were necessary to not only reach a high but also stable ^{39}Ar count rate. Based on that, deducing the ^{39}Ar concentration from a measured ^{39}Ar count rate was feasible and allowed for validating the apparatus with samples of known concentrations. This in turn allowed for dating of groundwater samples, two of which could be compared to an LLC measurement while the third had an unknown ^{39}Ar concentration.

5.1 Dating with ^{39}Ar

In order to date water with ^{39}Ar, the number of detected ^{39}Ar atoms have to be translated into an age. In section 2.1 it was stated, that if the number of ^{39}Ar atoms $N(t)$ in a water sample of age t is measured then the age can be determined from the natural decay law as

$$t = \tau \cdot \ln\left[\frac{N_0}{N(t)}\right] \tag{5.1}$$

where N_0 denotes the initial number of atoms in the water sample and τ the mean lifetime of ^{39}Ar. Deducing the age directly from the atom number is difficult, because counting all ^{39}Ar atoms in the water sample is not feasible with ATTA. Moreover, the initial number of ^{39}Ar atoms N_0 is hard to calculate precisely, since it depends on the solubility which in turn depends on temperature and salinity of the water sample at the time of it being last exposed to the atmosphere.

A better quantity for dating a water sample is therefore the concentration

$$c(t) = \frac{N(^{39}\mathrm{Ar})(t)}{N(\mathrm{Ar})} \tag{5.2}$$

between the number of ^{39}Ar atoms and the total number of argon atoms in the water sample. Given the atmospheric concentration $c_0 = 8.23 \cdot 10^{-16}$ (see section 2.3), the age t of the water sample can be deduced from the measured concentration $c(t)$ by

$$t = \tau \cdot \ln\left[\frac{c_0}{c(t)}\right] \ . \tag{5.3}$$

Practically, the concentration $c(t)$ for ^{39}Ar could be determined with the current setup by forming the ratio between the ^{39}Ar count rate and the ^{38}Ar MOT loading rate. However, ^{38}Ar can behave differently in the apparatus compared to ^{39}Ar since it does not have a hyperfine structure and therefore does not undergo changes related to repumping or magnetic fields that might alter the ^{39}Ar count rate.

Krypton has the advantage of possessing the abundant odd isotope ^{83}Kr which has hyperfine structure. It therefore, behaves like the rare radioisotopes ^{81}Kr and ^{85}Kr also regarding features related to the hyperfine structure. The concentration of ^{81}Kr and ^{85}Kr can therefore be determined by calculating the ratio of the ^{81}Kr single atom count rate and the ^{83}Kr MOT loading rate.

The only potential control isotope for ^{39}Ar would be ^{37}Ar. However, ^{37}Ar has a half-life of only 35 d, which hampers a reliable spiking of an argon sample, apart from the fact that its spectroscopic properties are not at all known and would have to be determined first. Moreover, it has a nuclear spin of $I = 3/2$ compared to the nuclear spin of $I = 7/2$ of ^{39}Ar, which curtails its aptitude as a control isotope[1].

Due to the lack of a control isotope, a different strategy for calibrating the measured ^{39}Ar count rate has been chosen in this experiment:
If the apparatus is sufficiently stable in that it always has the same efficiency for detecting ^{39}Ar atoms, then the count rate measured for a groundwater sample can simply be divided by the count rate measured for an atmospheric sample to obtain the concentration.
In other words, if $R(t)$ denotes the ^{39}Ar count rate for a water sample of age t and R_0 the ^{39}Ar count rate for an atmospheric sample, then the ^{39}Ar concentration in the water sample in terms of the atmospheric concentration is

$$c(t) = \frac{R(t)}{R_0} \text{ \% modern} . \tag{5.4}$$

The corresponding age is then obtained as

$$t = \tau \cdot \ln\left[\frac{c_0}{c(t)}\right] = \tau \cdot \ln\left[\frac{R_0}{R(t)}\right] . \tag{5.5}$$

The crucial and experimentally challenging point in this way of determining the ^{39}Ar concentration lies in achieving an ^{39}Ar detection efficiency, that is stable and reproducible on the timescale of a measuring campaign. The ^{39}Ar count rate measured in an enriched sample proved to be stable in terms of Poissonian statistics over a typical measurement time of 12 h. A near-Poissonian behavior was also obtained for the atmospheric ^{39}Ar count rate over a period of three months (discussed later). However, over the measurement period of three months a drift of about 15 % in the atmospheric ^{39}Ar was observed. The drift could be identified to originate from the source, which allowed for correcting the measured ^{39}Ar count rates with the signal from the atom beam profiler.

Although in this work minor corrections have to be made for the ^{39}Ar count rate, it seems possible to obtain a stable count rate with an improved source design that is

---

[1] This is in fact also the case for ^{81}Kr and ^{83}Kr, that have nuclear spins of 7/2 and 9/2, respectively.

not subject to degradation on the timescale of weeks. This would allow for directly implementing the calibration method stated above.

Before discussing the stability of the system as well as the measures required for online-monitoring of the system's performance, expressions for the dating precision will be derived.

5.2 Dating precision

When the error for the age obtained with the natural decay law in expression (5.1) is calculated by error propagation, it is typically assumed, that the natural decay law provides an exact expression. However, the number of atoms $N(t)$ that is still left after time t is in fact the mean value from a binomial distribution with the probability $p = e^{-t/\tau}$ for an atom to have decayed after the time t. The standard deviation for this mean value is

$$(\Delta N)_{\mathrm{rad}} = \sqrt{N_0 \cdot p(1-p)} = \sqrt{N_0}\sqrt{e^{-t/\tau} - e^{-2t/\tau}} \ . \tag{5.6}$$

Assuming that the inital number of atoms N_0 is exactly known, the absolute and relative error for the age t due only to radioactivity statistics becomes

$$(\Delta t)_{\mathrm{rad}} = (\Delta N)_{\mathrm{rad}} \cdot \left|\frac{dt}{dN}\right| = \frac{\tau}{\sqrt{N_0}}\sqrt{e^{t/\tau} - 1} \qquad \frac{(\Delta t)_{\mathrm{rad}}}{t} = \frac{\tau}{t\sqrt{N_0}}\sqrt{e^{t/\tau} - 1} \ . \tag{5.7}$$

As shown in figure 5.1 for $t = 500\,\mathrm{a}$, this error becomes relevant for inital atom numbers N_0 below 1000 corresponding to about 100 ml of water. This sample size can be regarded as the absolute lower limit for dating water with ^{39}Ar.

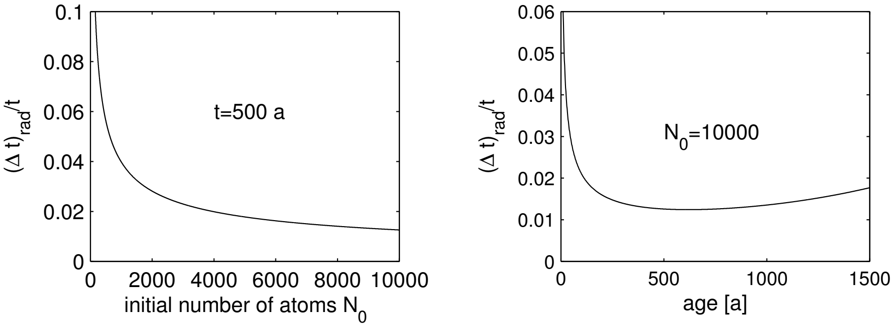

Figure 5.1: Dating precision due to the statistics of radioactivity. Left) Relative error of the derived age t versus the initial number of atoms N_0 for $t = 500\,\mathrm{a}$. Right) Relative error of the derived age t versus the age for a fixed initial atom number of $N_0 = 10\,000$.

For a fixed initial atom number $N_0 = 10\,000$, the relative age error shows a minimum for an age of about 500 a. For typical sample sizes of several liters of water, the error due to the radioactive statistics can safely be neglected. It has to be pointed out, that for an initial atom number of less than one thousand, the statistical distribution of the atoms in the sampled groundwater also starts to play a role.

If $R := R(t)$ denotes the measured ^{39}Ar count rate of a sample, then the error for the ^{39}Ar concentration (5.4) can be calculated to

$$\Delta c = \frac{1}{R_0} \cdot \sqrt{\frac{R^2}{R_0^2} \cdot \Delta^2 R_0 + \Delta^2 R} \tag{5.8}$$

where ΔR_0 and ΔR denote the corresponding errors of the ^{39}Ar count rates. The error for the age in expression (5.5) is accordingly obtained as

$$\Delta t = \tau \cdot \sqrt{\frac{\Delta^2 R_0}{R_0^2} + \frac{\Delta^2 R}{R^2}} \; . \tag{5.9}$$

These expressions provide the base for the error calculation in the following sections.

5.3 Monitoring and stability

As discussed above, the chosen method for determining the ^{39}Ar concentration out of a measured ^{39}Ar count rate relies on a stable detection efficiency during a measurement as well as from one measurement to another. Before and after each measurement, the performance of the apparatus for the stable argon isotopes is measured with the atom beam profiler as well as with the MOT loading rate. If the assigned detection efficiency is obtained for the stable argon isotopes, then only effects specific to ^{39}Ar can alter the ^{39}Ar count rate. In order to exclude ^{39}Ar specific changes which are not visible for the stable isotopes, all experimental parameters especially the ones particularly relevant for ^{39}Ar are always adjusted to the same setting. Moreover, these parameters are monitored during an entire ^{39}Ar measurement, to ensure that they only change within a range that does not affect the ^{39}Ar count rate. Among others, the monitored parameters include laser power, laser frequencies, laser stabilization signals, power ratios of repumpers with respect to the cooler and the atom flux monitoring described in section 3.2. Moreover, the power of the MOT and the Zeeman slower beams at the apparatus is actively stabilized. An impression of the monitoring system is depicted in figure 5.2.

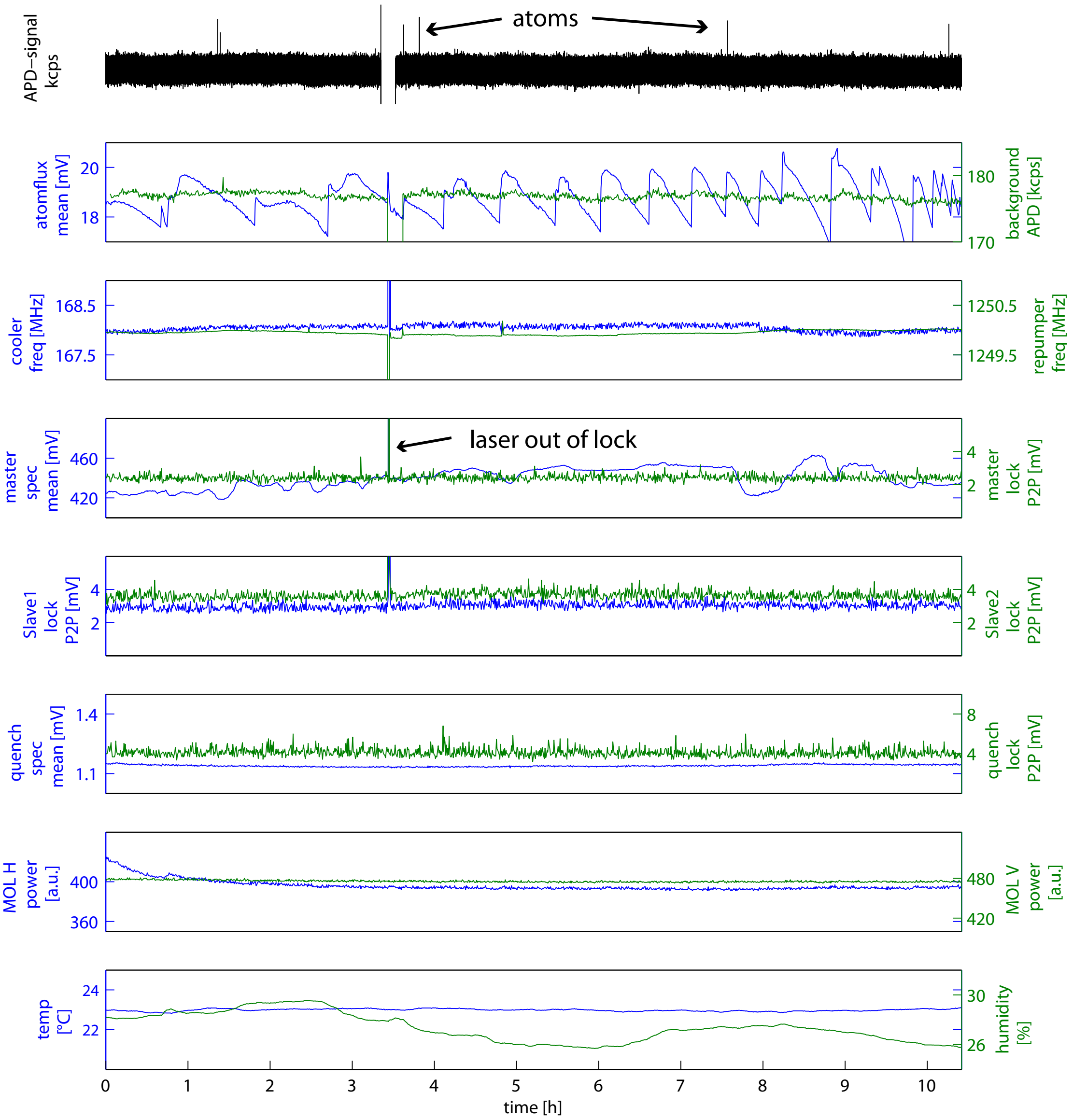

Figure 5.2: Impression of the monitoring system for a 10 h measurement of a water sample from the Great Artesian Basin in Australia. The first row shows the APD signal where the atoms are visible. In the second row the atom flux is plotted which reflects the pressure regulation for introducing the sample into the vacuum chamber. The monitoring system of the experiment was developed in [5].

In order to verify, whether the measures taken are sufficient to achieve a stable source performance at least for the even argon isotopes, a longterm measurement has been performed with the atom beam profiler (figure 5.3). Even the minor amplitude modulation of the measured signal of less than 2 % would average out over the 10 h measurement time.

This result indicates that the performance of the setup excluding MOT and Zeeman slower can be operated on a stable performance with negligible fluctuations.

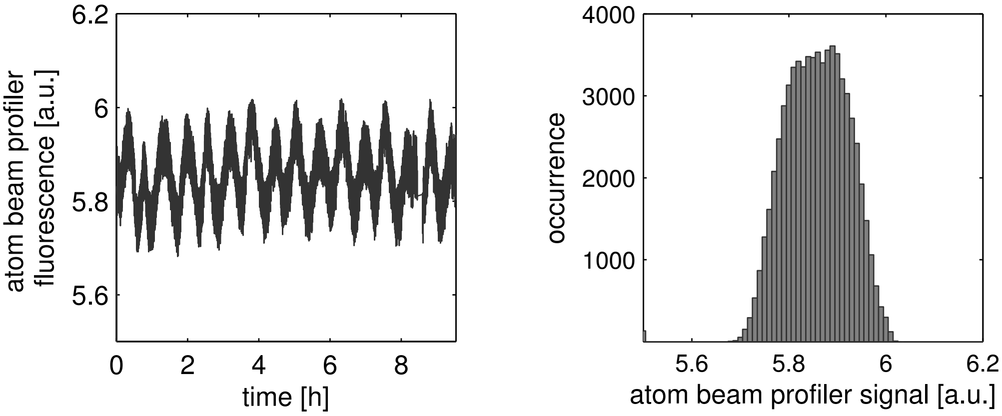

Figure 5.3: Measurement of the signal from the atom beam profiler over almost 10 h (left). The signal exhibits a continuous modulation of unclear origin with a period of 40 min and an amplitude of less than 2 % relative to the mean value. The histogram (right) reflects the 4.5 % standard deviation of the signal from the atom beam profiler.

To ensure that also the MOT and the Zeeman slower exhibit a similar stability, a longterm measurement of the loading rate has to be recorded, which will be done as soon as the improved setup for measuring the MOT loading rate has been implemented.

In order to verify that the detection efficiency is stable over the timescale of a measurement not only for ^{40}Ar but also for ^{39}Ar, the ^{39}Ar MOT fluorescence has been measured for 5 h in an enriched sample with an ^{39}Ar concentration of about 10^{-9} (left plot in figure 5.4). The histogram of the MOT fluorescence shows a large standard deviation, but the mean stayed constant within 5 %. The MOT fluorescence of the ^{39}Ar MOT depends on the single atom signal which in turn can change due to fluctuations of the magnetic field or the laser light. Moreover, it is not proportional to the ^{39}Ar loading rate since already collisions among metastable atoms become relevant (section 3.4).

To exclude these effects, the single atom count rate of ^{39}Ar has been measured in a sample with lower enrichment for 12 h which is the time-scale of a typical ^{39}Ar measurement (right plot in figure 5.4). The histogram exhibits a Poissonian-like distribution, which indicates that within the given statistics no significant drifts in the mean count rate have occurred during the measurement.

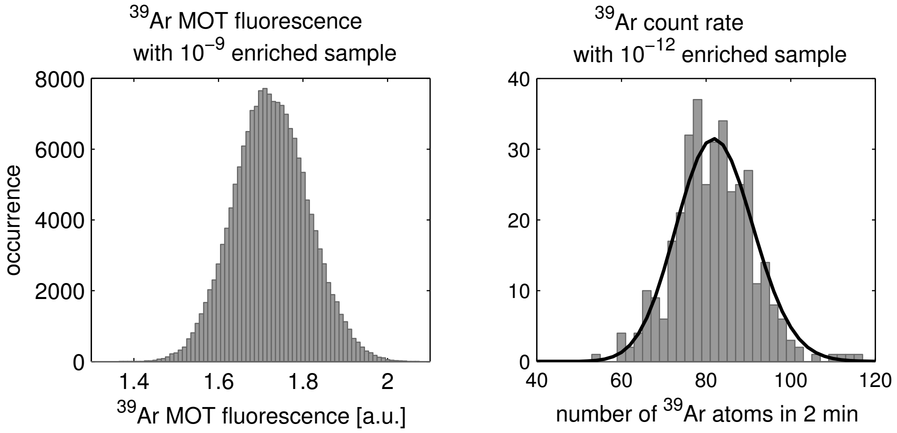

Figure 5.4: Stability of the detection efficiency for ^{39}Ar. Left) 5 h measurement of the ^{39}Ar MOT fluorescence with 10^{-9} enriched sample. Right) 12 h measurement of the ^{39}Ar counts in 2 min in an enriched sample with 10^{-12} abundance.

These measurements indicate that it is possible to maintain a stable detection efficiency for ^{39}Ar over the timescale of a typical ^{39}Ar measurement. However, the detection efficiency for ^{39}Ar also has to be reproducible from one measurement to another. The degree of reproducibility for the ^{39}Ar count rate measured over a period of almost three months in atmospheric argon is the subject of the following section.

5.4 Atmospheric ^{39}Ar count rate

The atmospheric ^{39}Ar measurements shown in figure 5.5 were conducted during a period of almost three months. The experimental parameters were always adjusted to the same settings and monitored during the entire measurement, which on average lasts about 10 h. The histogram over all measurements combined in 2 h frames can be described with a Poissonian distribution, which represents the absolute theoretical limit of atom counting statistics. The variance of the single measurements is even slightly lower than the mean value of the fitted Poissonian distribution, which indicates that a Poissonian nature is underlying the dataset. However, due to the sparse statistics, the histogram can actually be misleading. From the experimental behavior, an aging process of the source was suspected, due to the difficulty in ignition and instabilities observed on the atom flux monitor. This deterioration process is not visible on the data in 5.5 by bare eye. However, if three subsequent measurements are grouped together, a decline in the ^{39}Ar count rate becomes clearly visible between two rising slopes at the beginning and the end. The same trend is apparent in the binned values of the atom beam profiler, that have been recorded for each

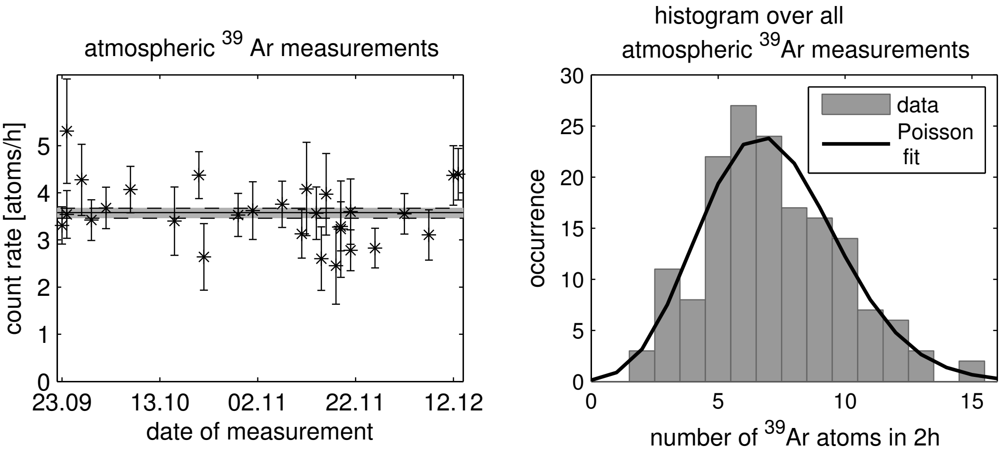

Figure 5.5: Compilation of all twenty-eight ^{39}Ar measurements in atmospheric argon each lasting between 3–21 h. Left) The error bars plotted for each measurement correspond to a 1σ confidence level given by the number of detected atoms. The shaded area in the center corresponds to the 1σ environment of the mean value, which is derived from the standard deviation of the total number of counted atoms. Right) The histogram of the data in 2 h frames reveals a Poissonian character.

measurement[2]. This correlation confirms the suspicion, that the source deteriorated during the measuring period, especially in the consistently higher values in both the ^{39}Ar measurement and the atom beam profiler after the replacement of the source. The ^{39}Ar count rates from the atmospheric measurements have therefore been scaled with the normalized values from the atom beam profiler (right plot of figure 5.5) which significantly mitigates the drift. With the corrected measurements the mean atmospheric ^{39}Ar count rate is obtained to[3]

$$R_0' = 3.6(1)\,\text{atoms/h}\ . \tag{5.10}$$

For the ^{39}Ar measurements presented in the following, no correction with the atom beam profiler was necessary, since the apparatus was operating on mean performance.

The measured ^{39}Ar atmospheric count rate R_0' is preliminarily written with a prime, since it has to be corrected for the contamination present in the current setup.

---

[2] More precisely, values from the atom beam profiler are recorded before and after each measurement. The mean value of the two is shown in figure 5.6.

[3] Here and also in the following, always the 1σ error will be stated. However, it is stressed that only 68 % of the measured ^{39}Ar count rates lie within the 1σ confidence interval.

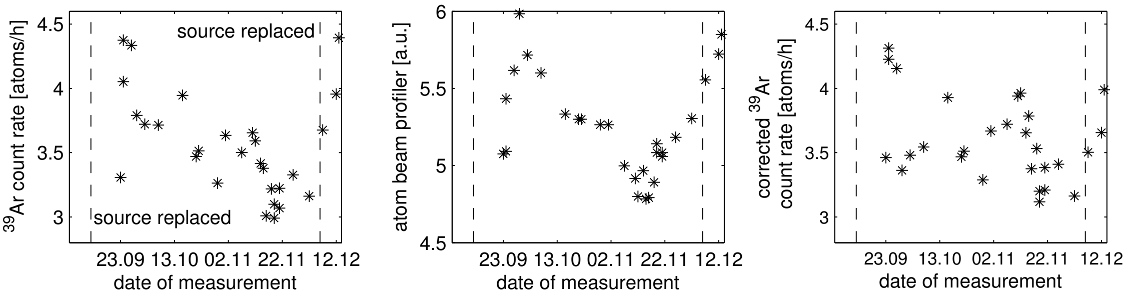

Figure 5.6: Correction of the atmospheric ^{39}Ar count rate. Left) Each atmospheric ^{39}Ar measurement of figure 5.5 is averaged together with its adjacent measurements. A clear drift becomes visible between the dates of the source replacements. Middle) The atom beam profiler exhibits the same behavior which confirms that the drift originates from a deterioration of the source. Right) The drift in the atmospheric ^{39}Ar count rate can be mitigated by correcting the atmospheric ^{39}Ar measurement with the normalized values from the atom beam profiler.

5.5 Contamination

The apparatus has mainly been optimized on the stable argon atoms with the atom beam profiler and the MOT loading rate. However, the optimum settings for the Zeeman slower and the MOT are expected to be different for ^{39}Ar than for the even isotopes. The effect and the settings of the repumpers also had to be found out for an optimum and stable operation. Therefore, enriched samples up to an ^{39}Ar abundance of 10^{-9} have been used to optimize the experimental settings for ^{39}Ar.

Introducing enriched samples into the apparatus came at the cost of contaminating the vacuum chamber with ^{39}Ar. When the apparatus is operated in recycling mode, the ^{39}Ar contamination outgassing from the vacuum chamber accumulates. If the source is turned off during recycling, the ^{39}Ar count rate is still on the atmospheric level after ignition of the source. This is a clear hint, that the contamination originates from the vacuum parts that are exposed to the plasma. Replacing most of these parts lowered the contamination measured in recycling, whereas flushing for about ten hours with xenon and krypton only had a marginal effect. After all measures have been taken, the ^{39}Ar count rate after one hour of recycling was still ten times higher than the atmospheric count rate. More precisely, in recycling operation the ^{39}Ar count rate increases with a rate of about $50\,\mathrm{atoms/h^2}$ due to contamination. Considering that a typical ^{39}Ar measurement lasts for more than ten hours, measuring in recycling is precluded by the ^{39}Ar contamination from the vacuum chamber.

For the first measuring campaign, it has therefore been decided not to measure in recycling but in throughput mode. If one very conservatively assumes, that measuring in throughput corresponds to a recycling time of a second, then the contamination should not contribute more than 0.01 atoms/h. Another simple estimate for the contamination can be obtained from the amount of argon gas that outgasses when a measurement with krypton is performed. In such a case, the ^{40}Ar MOT fluorescence is roughly half as high as the ^{38}Ar MOT fluorescence. Recalling that the ratio of the two isotopes is ^{40}Ar/^{38}Ar$\approx$ 1600, the contribution from argon outgassing from the vacuum chamber relative to the introduced gas is about $3 \cdot 10^{-4}$. In order to significantly contribute to the ^{39}Ar count rate, the ^{39}Ar abundance in the outgassing argon would have to be higher than 10^{-13}.

Nevertheless, the only reliable method to determine the degree of contamination is to measure the ^{39}Ar count rate in an ^{39}Ar-free sample. Since initially such a sample was not available, krypton was used as an ^{39}Ar-free sample. In order to verify, that the outgassed argon is equally excited in the source with krypton as with argon, the signal from the atom beam profiler and the atom flux monitoring was measured as a function of krypton admixture (figure 5.7).

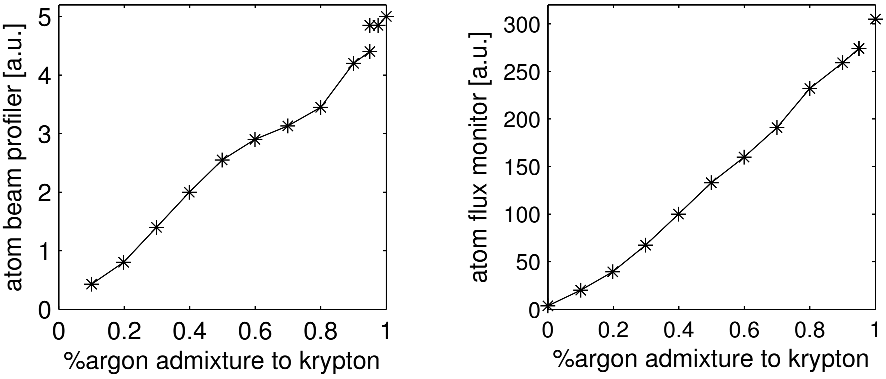

Figure 5.7: Signal of the atom beam profiler (left) and the atom flux monitor (right) versus the argon concentration in the mixture with krypton.

Apparently, the krypton admixture only dilutes the argon concentration as desired. An increase in the excitation efficiency as reported in [87] could not be observed. This measurement indicates, that krypton can actually be used as an ^{39}Ar free sample in order to monitor the contamination. This finding is confirmed by recirculation measurements, which yielded the same ^{39}Ar count rates for argon and krypton. No ^{39}Ar atoms were observed during a five hour measurement with krypton in throughput mode, which implies, that the ^{39}Ar contamination is with 90 % below 0.5 atoms/h.

Although the krypton measurements infer a non-significant contamination, an ^{39}Ar-free sample has been measured to exclude any effects that might result from using krypton instead of argon. The sample was extracted from groundwater in the Great Artesian Basin (GAB), Australia. Its ^{39}Ar concentration was measured by LLC at the University of Bern to be lower than the detection limit of 5 % modern. A total of 8 atoms in 17.5 h corresponding to a count rate of 0.46(16) atoms/h was measured with ^{39}Ar-ATTA. Given the stated detection limit of the LLC measurement, the ^{39}Ar count rate due to contamination of the apparatus ranges between 0.3–0.46 atoms/h. In the following the mean value[4]

$$R_c = 0.38(18)\,\text{atoms/h} \tag{5.11}$$

will be used for correcting the obtained ^{39}Ar count rates.

This implies, that the krypton measurement was either statistically not significant enough, or that krypton can not be used as an ^{39}Ar-free sample. With the measured ^{39}Ar count rate due to the contamination, the probability that no atoms are detected in a five hours measurement of a ^{39}Ar-free sample is around 15 %. In other words, in every seventh 5 h-measurement with an ^{39}Ar-free sample, it is expected not to observe an ^{39}Ar atom. The result obtained for krypton is therefore not very unlikely. Further clarification would require a longer ^{39}Ar measurement with krypton. However, before that happened the ^{39}Ar-free sample was already provided by the University in Bern. Furthermore, large quantities of ^{39}Ar-free argon will also be available from the DarkSide-collaboration soon. Moreover, important monitoring and control mechanisms as provided by the atom flux monitor and the atom beam profiler are not available in ^{39}Ar measurements with krypton, so that the results would not be of quantitative use in a strict sense. Therefore, the measurements with krypton are not pursued.

If the mean value for the contamination is included into the analysis of the ^{39}Ar count rate, then the atmospheric value becomes

$$R_0 = 3.22(21)\,\text{atoms/h} \qquad \text{atmospheric } ^{39}\text{Ar count rate} \;. \tag{5.12}$$

5.6 Calibration

The foregoing sections show, that the atmospheric ^{39}Ar count rate over a time span of three months is nearly Poissonian and that a contamination of 12 % modern is present in the current setup.

In order to verify, that the presented ^{39}Ar counting can be used for dating groundwater samples, a calibration curve with prepared ^{39}Ar concentrations was measured. In the ideal case, the samples with defined concentration are prepared from an ^{39}Ar-free sample and atmospheric argon. In order to obtain sufficient statistics, a large quantity of ^{39}Ar-free argon is required for preparing the samples, which was not available at that time. Therefore, the argon extracted from the oldest known groundwater easily available in big quantities at that time was chosen for the calibration measurements. This groundwater stems from the deep Glatt Valley aquifer [88] situated about 100 m below ground level (figure 5.8). The ^{39}Ar concentration in the aquifer was measured in 1998 by LLC in Bern to be 9(5) % modern, which is only marginally higher than the detection threshold of 5 %.

---

[4] The error has been calculated by quadratically adding the statistical error of the measurement and the error due to taking the mean value of the contamination. Also in the following the errors will be calculated taking the square root of the quadratic sum.

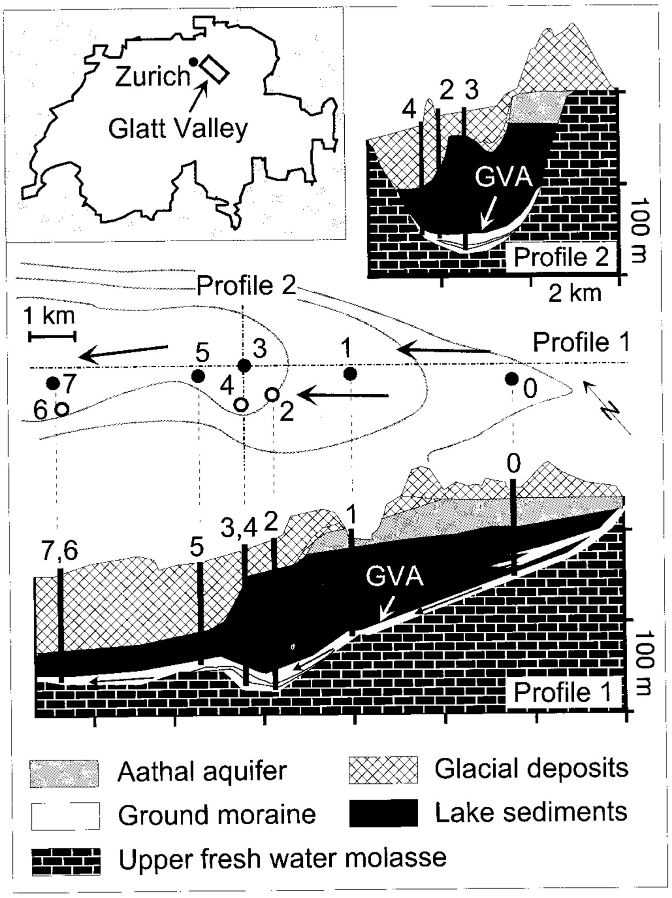

Figure 5.8: Hydrological schematic of the Glatt Valley aquifer, that was sampled for obtaining argon with low ^{39}Ar concentration. Top left) Map showing the Glatt Valley near Zurich in Switzerland. Center) Location of the different boreholes in the aquifer system. The ^{39}Ar concentration of the water in borehole 1 was measured to be 9(5) % modern by LLC at Bern in 1998. The water from Borehole 1 was chosen for the calibration measurements with ^{39}Ar-ATTA (from [88]).

The borehole that was probed is located in the district of Uster near the city of Zurich in Switzerland (figure 5.8). In the course of a field trip, the water was sampled with the degassing system described in [89], which was developed by the group of Werner Aeschbach-Hertig at the environmental institute for physics in Heidelberg. There, also an extraction system for seperating argon from air based on gas-chromatography was developed in the course of the presented ^{39}Ar-ATTA project. The gas extracted from the sampled groundwater could be purified with the implemented system. A total of around 51 argon gas was obtained from the sampling campaign, which is sufficient for the intended calibration measurements. Further details on the sampling campaign can be found in [90].

For the Uster-sample, a total of sixteen ^{39}Ar atoms was counted in almost twenty hours, which corresponds to an ^{39}Ar count rate of 0.82(20) atoms/h.

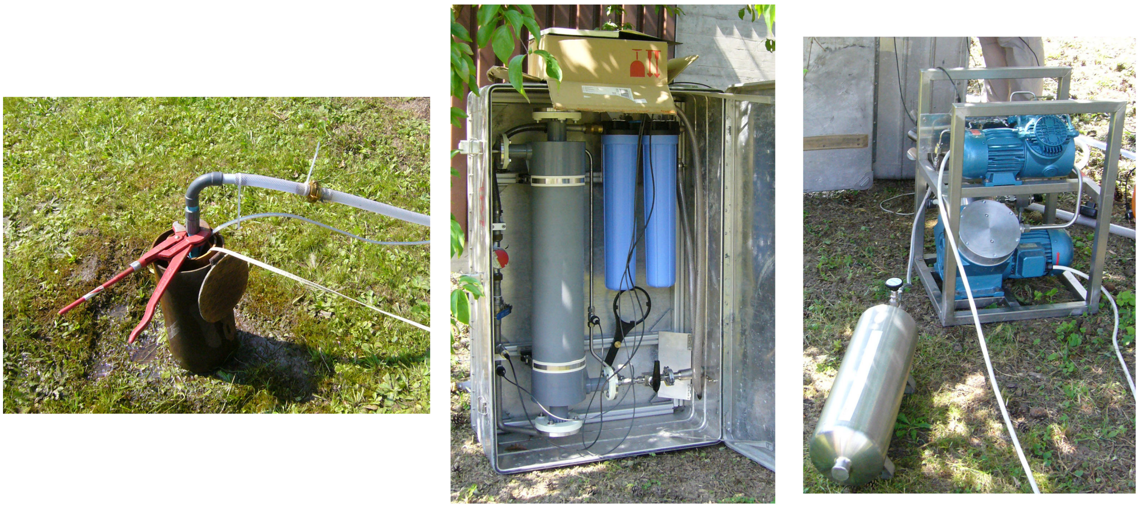

Figure 5.9: Pictures of sampling groundwater from the Glatt Valley aquifer near the city of Zurich in collaboration with the institute for environmental physics in Heidelberg. Left) Outlet of the 100 m deep borehole. The groundwater table is higher than the surface leading to water pouring out. Middle) Apparatus for degassing the groundwater. Right) Compression of the extracted gas into a 9 l sample cylinder at 7 bar. Further details on the degassing system and the sampling can be found in [89, 90].

Correcting for the ^{39}Ar background count rate R_c yields an ^{39}Ar count rate, concentration and age for the Uster sample of

$$R_{\text{Uster}} = 0.44(27)\,\text{atoms/h} \quad c_{\text{Uster}} = 14(9)\,\%\ \text{modern} \quad t_{\text{Uster}} = 771(241)\,\text{a}\ .$$

The corrected value is in agreement with the LLC measurement on the 1σ confidence level.

With the argon extracted from the Glatt valley aquifer and commercial argon (extracted from air), samples with different concentrations have been prepared in order to check, whether the measured ^{39}Ar count rate scales linearly with the prepared concentration. The samples were mixed in a vacuum container with a volume of about 1 l attached to a high precision pressure gauge (Keller, LEX1). The desired ^{39}Ar concentration was adjusted by filling the volume with Uster and atmospheric sample to the corresponding pressure ratio. Given the ^{39}Ar concentration of the Uster sample measured by LLC to be 9(5) % modern, the samples with concentrations shown in table 5.1 have been measured. Since the value for the ^{39}Ar concentration of the Uster-sample measured by LLC is used for mixing the samples, the ^{39}Ar concentration measured by ATTA represents one of the calibration points[5].

---

[5] For the measured concentrations, no corrections with the atom beam profiler were necessary, since the apparatus was operating on the mean performance

Table 5.1: ^{39}Ar concentrations of prepared samples measured with ATTA.

concentration mixed % modern	measuring time [h]	counted ^{39}Ar atoms	^{39}Ar concentration measured with ATTA % modern
9(5)	19.5	16(4)	14(9)
46(6)	9.23	21(5)	59(17)
73(3)	14	42(6)	81(16)

The results are plotted in figure 5.10. The measured ^{39}Ar concentrations are in agreement with the ideal calibration line defined by the atmospheric ^{39}Ar count rate, although it is striking that all measured ^{39}Ar concentrations lie above it.

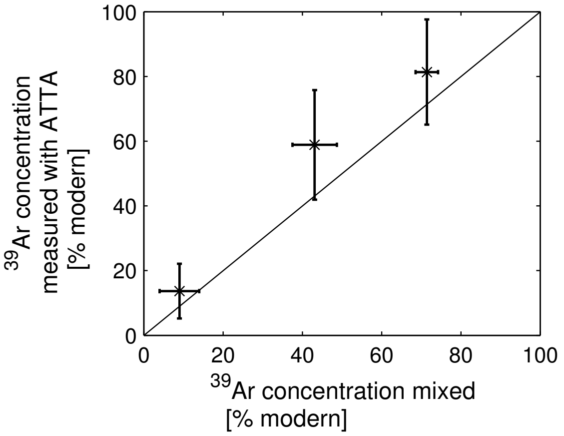

Figure 5.10: ^{39}Ar concentrations measured with ATTA versus the ^{39}Ar concentration obtained by mixing the atmospheric standard with argon from the Uster sample. The line illustrates the ideal calibration case, defined by the atmospheric ^{39}Ar count rate.

5.7 Groundwater samples

Having confirmed with the calibration curve, that dating of groundwater with ^{39}Ar-ATTA is possible, further groundwater samples from different aquifer systems have been measured.

Two study sites close to the city of Heidelberg have been chosen, one being the Schwetzinger Hardt and the other being the Hessian Ried. The groundwater sampling and the argon extraction were carried out by the collaborating group at the institute of environmental physics. Details on groundwater systems, sampling and argon extraction can be found in [89, 90]. For an intercomparison between the ^{39}Ar measurements with LLC in Bern and with ^{39}Ar-ATTA in Heidelberg, the group from the University of Bern also extracted water from the Schwetzinger Hardt for ^{39}Ar analysis.

During the measurement period presented in this work, two groundwater samples were measured. The ^{39}Ar-ATTA counting results for the sample F18/2 from the Schwetzinger Hardt and the sample HR544259 from the Hessian Ried are printed in table 5.2.

Table 5.2: Groundwater samples measured with ^{39}Ar-ATTA.

sample	measuring time [h]	number of ^{39}Ar atoms	concentration [% modern]	^{39}Ar age [a]
F18/2	9.67	31(6)	88(20)	51(87)
HR 544259	8.85	4(2)	2(15)	> 830

Both samples were measured for almost ten hours. The sample F18/2 was determined to be very young which is in agreement with the high ^{3}H and ^{14}C content. Moreover, the measured value is in good agreement with the value measured by LLC in Bern (table 5.3).

The sample HR544259 from the Hessische Ried exhibits an ^{39}Ar count rate which is below the actual detection limit of the apparatus given by the contamination. The corrected concentration is therefore next to zero. With the given contamination, the water is consequently older than 830 a. This finding is in agreement with the very low ^{3}H and ^{14}C concentrations, leading to a ^{14}C age of 24 395 a. Moreover, the temperature of the water sample at its last contact with the atmosphere as derived from the noble gas solubilities (NGT) is very low, indicating that the sample originates from the last glacial period which ended about 15 000 a ago. The agreement of the ^{39}Ar-ATTA results with the LLC measurements as well as with the other isotope data show that dating of groundwater with the presented ^{39}Ar-ATTA setup is feasible.

Table 5.3: Groundwater samples measured with ^{39}Ar-ATTA in comparison with complementary isotope data.

sample	depth [m]	NGT °C	^{3}H [TU]	^{14}C [pmC]	^{39}Ar LLC [% mod]	^{39}Ar ATTA [% mod]	^{39}Ar age LLC [a]	^{39}Ar age ATTA [a]
F18/2	65-73	7.8(0.6)	7.5	84	87(10)	88(20)	54(44)	51(87)
HR 544259	79-128	4.3(1.1)	0.6(9)	0.025(20)	-	2(15)	-	> 830

6 Conclusion and outlook

In the good tradition of the theses handed in from the presented ^{39}Ar-ATTA project, a summary of the current apparatus' fidelity is provided in order to obtain an estimate of the expected atmospheric ^{39}Ar count rate. Comparing the estimated with the measured ^{39}Ar count rate yields information concerning whether the current apparatus exploits its full potential. Moreover, the analysis of the performance allows for identifying potential improvements of the setup.

6.1 Performance of the apparatus

From the experimental analysis provided in the foregoing chapters, the ^{39}Ar count rate for an atmospheric sample can be estimated as

$$R_0^{\text{est}} = q \cdot c_0 \cdot \eta_{\text{geom}} \cdot \eta_{\text{coll}} \cdot \eta_{\text{mol}} \cdot \eta_{\text{zsl}} \cdot \eta_{\text{mot}} \cdot \eta_{\text{ident}} \cdot \eta_{\text{hfs}} \ . \tag{6.1}$$

In the above expression

$$q = 2 \cdot 10^{14} \ \frac{\text{atoms}}{\text{s sr}} \tag{6.2}$$

is the metastable flux measured in section 3.2 with the atom flux monitoring, which has to be multiplied with the atmospheric abundance of ^{39}Ar

$$c_0 = 8.23 \cdot 10^{-16} \tag{6.3}$$

to obtain the metastable ^{39}Ar flux. Given the measured velocity distribution and the geometry of the apparatus, a fraction of

$$\eta_{\text{geom}} = 2 \cdot 10^{-4} \tag{6.4}$$

reaches the MOT. The collimation gain for ^{39}Ar was measured with enriched samples to be (section 3.7)

$$\eta_{\text{coll}} = 87 \ . \tag{6.5}$$

The MOL was measured to increase the ^{39}Ar count rate by a factor of (section 3.8)

$$\eta_{\text{mol}} = 1.4 \ . \tag{6.6}$$

Given the capture velocity of the Zeeman slower of $600\,\mathrm{m/s}$ and a mean longitudinal velocity of the atom beam of $283\,\mathrm{m/s}$, the efficiency of the Zeeman slower is theoretically

$$\eta_{\text{zsl}} \approx 0.99 \ . \tag{6.7}$$

In [10] a Zeeman slower efficiency of 29 % was measured for ^{40}Ar without the MOL and with different settings for the magnetic field as well as for the detunings. The Zeeman slower efficiency increased thereafter as a result of systematic optimization but the current value has not been measured yet. Therefore, the theoretical efficiency as stated above is used while emphasizing, that this value may even be half the theoretical value.

The considerations in section 3.10 indicate that the MOT only captures half of the slowed atoms, due to the limited capture radius in the vertical dimension along the magnetic coils. The MOT efficiency is therefore assumed to be around

$$\eta_{\mathrm{mot}} = 0.5 \ . \tag{6.8}$$

If an atom is captured in the MOT, it can still happen that the atom is not identified by the detection system. The fraction of identified atoms with the adaptive threshold described in section 4 was caclulated to be

$$\eta_{\mathrm{ident}} = 0.96 \ . \tag{6.9}$$

Three out of four sidebands of the ^{39}Ar hyperfine states are covered in the collimator, which theoretically yields a factor of

$$\eta_{\mathrm{hfs}} = 0.92 \tag{6.10}$$

where only the 8 % of the fifth hyperfine state are missing. Potential hyperfine losses due to inefficient repumping in the collimator would already be included in the measured collimation gain. Inefficient repumping in the MOT would become apparent in the single atom signal and can be excluded since this is not observed for the chosen experimental parameters. The losses due to the hyperfine structure should therefore not be far from the value stated above.

Merging all numbers together, the estimated atmospheric ^{39}Ar count rate becomes

$$R_0^{\mathrm{est}} = 6.3 \, \frac{\mathrm{atoms}}{\mathrm{h}} \quad . \tag{6.11}$$

The main uncertainty in this value is attributed to the uncertainty in the atom flux derived from the measurement as well as to the uncertainty in the Zeeman slower and MOT efficiency that have not yet been measured. Still, the estimated value lies in the range of the measured ^{39}Ar count rate $R_0 = 3.22(21)$ atoms/h.

The considerations of section 3.7 indicate that a direct improvement of the ^{39}Ar count rate in the existing setup can be achieved by reoptimizing the collimator, which could potentially double the ^{39}Ar count rate.

Another factor 1.5–2 can be obtained by increasing the capture range of the MOT as discussed in section 3.10. This would require a redesign of the magnetic field configuration and a second MOT frequency introduced in the MOT laser beams. Both improvements could already lead to an atmospheric ^{39}Ar count rate close to 10 atoms/h.

However, the biggest potential for increasing the ^{39}Ar count rate by atom optical means lies in the transverse cooling of the atom beam emerging from the source. Only a small percentage of the atoms reach the MOT due to their transverse velocity and even if the collimator was ideal, this fraction could only be increased to about 10 % in the current setup. If the source exit could be brought closer to the collimator the fraction could be increased to about 25 % but this would very likely come at the cost of excitation efficiency. The optimum compromise between excitation and collimation efficiency has to be further investigated experimentally.

The maximum fraction of atoms that can be collimated is limited by the maximum force F_{max}, that can be reached with radiative laser cooling. In order to slow down atoms with a higher transverse velocity than the capture velocity v_{rc} of the collimator, a more efficient laser cooling that reaches a higher maximum force is necessary. A force exceeding the maximum force given from radiative cooling by an order of magnitude can practically be realized by the technique known as *bichromatic cooling* [91, 92, 93, 94]. Simply speaking, bichromatic cooling is not based on absorption-spontaneous emission cycles as with radiative cooling but on absorption-stimulated emission cycles. These cycles require synchronized and counterpropagating pulse trains for the absorption and the stimulated emission respectively (figure 6.1).

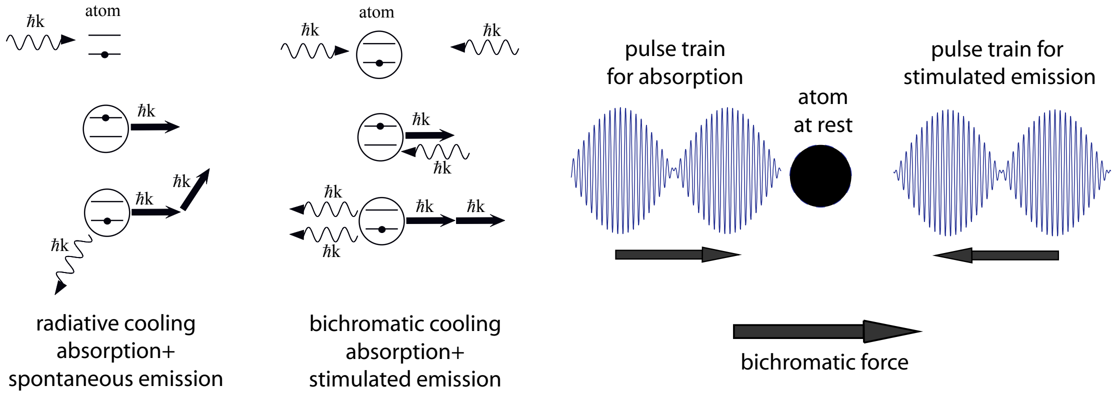

Figure 6.1: Principle of bichromatic cooling. Left) Simplified picture of bichromatic cooling as compared to radiative cooling. Bichromatic cooling can reach a much higher repetition rate for absorption-emission cycles since it is not limited by the spontaneous decay rate. Right) The absorption-stimulated emission cycles require synchronized and counterpropagating pulse trains (adapted from [95]).

In this way, the repetition rate is not limited by the spontaneous decay rate of the transition but by the Rabi frequency which the transition is driven with. The Rabi frequency can in principle be made arbitrarily high and is only limited by the available laser power. An additional benefit of bichromatic cooling is the large velocity capture range. For argon, a bichromatic force $F_{\mathrm{bc}} \approx 10 \cdot F_{\mathrm{max}}$ and a capture range of about 50 $\mathrm{m/s}$ can be achieved with reasonable laser power requirements.

A possible scheme for pre-collimating atoms with a transverse velocity higher than the capture velocity of the collimator for the current setup is depicted in figure 6.2.

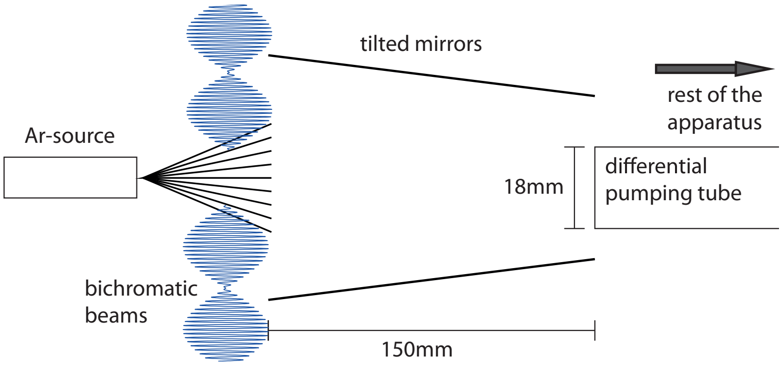

Figure 6.2: Schematic of a possible pre-collimation scheme with bichromatic cooling in the current setup (adapted from [95]).

Assuming a cooling length of 1 cm and the bichromatic force F_{bc} stated above, the maximum transverse velocity that can be collimated as a function of the longitudinal velocity is significantly higher than for the collimator alone (figure 6.3).

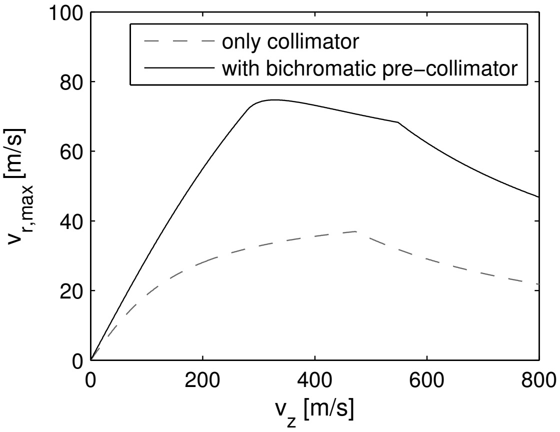

Figure 6.3: Maximum transverse velocity that can be collimated as a function of the longitudinal velocity with and without bichromatic pre-collimation. The curve with bichromatic pre-collimation is calculated in a similar way to that in section 3.7. The curve without bichromatic pre-collimation is the same as in figure 3.14 calculated for an acceleration of $a_{\max}/2$.

The atom fraction of about 6 % collimated without bichromatic pre-collimation increases by a factor four with bichromatic pre-collimation, yielding almost 25 % of the atoms being captured. This factor changes depending on how close the exit of the source tube is located to the collimator but in general a factor of more than two in the fraction of collimated atoms can be gained with bichromatic pre-cooling.

Initial preparatory work has been carried out towards the realization of a bichromatic pre-collimation [95], in which an amplified optical beating with a homebuilt Tapered Amplifier could be realized. If the bichromatic cooling proves applicable in the setup, one may even replace the current collimator with a bichromatic collimator.

The biggest potential for improving the ^{39}Ar count rate lies in the source, recalling that the excitation efficiency is on the order of 10^{-4}-10^{-3}. Future developments will include a more efficient cooling of the source tube, different geometries of the RF coil and an optimized positioning of the source tube relative to the RF-coil.

An increase in the ^{39}Ar count rate can moreover be achieved by reducing the deexcitations in the source chamber caused by collisions with the background gas, which could for example be realized with an additional pumping stage right behind the source. Moreover, deexcitations occur in the atom beam on the way to the MOT, as has been observed by comparing the pressure dependence of the atom flux monitor and the atom beam profiler. This loss could for example be mitigated with a tilted source, such that metastable atoms are selectively transported to the MOT.

6.2 Dating of groundwater

With the presented apparatus an ^{39}Ar count rate allowing for dating of groundwater has been achieved. An ^{39}Ar contamination corresponding to 12(6) % modern has been measured with a sample, whose ^{39}Ar concentration was measured to be $<$ 5 % modern by LLC. If the corresponding ^{39}Ar background count rate of 0.38(18) atoms/h is used for correction, the apparatus achieves an atmospheric ^{39}Ar count rate of 3.22(21) atoms/h.

The ^{39}Ar contamination presently hampers measurements in the recycling mode, which would allow for ^{39}Ar analysis in water samples down to a liter of water. Due to the contamination, the measurements have to be performed in throughput mode, which requires a sample size of 0.5–1 l argon gas, which corresponds to 2–4 t of water. For this reason, the ^{39}Ar measurements are currently restricted to groundwater samples. However, removing the contamination from the apparatus is only a matter of replacing vacuum parts, which can be done as soon as measurements with enriched samples are no longer necessary.

Based on controlled mixtures of atmospheric argon and the sample from the Glatt Valley aquifer with known ^{39}Ar concentration of 9(5) % modern, the application of the presented system to dating of water could be validated.

An improvement in the uncertainty of the measured ^{39}Ar concentration can be achieved by further stabilizing the apparatus. The source has been identified as a main cause for short as well as for long term fluctuations. A more robust source design is therefore essential for a stable ^{39}Ar count rate. But even if the apparatus proves to be stable, the techniques for permanent monitoring of the apparatus' performance need further development. The atom flux monitoring already provided a signal very sensitive to changes in the metastable flux. However, since it does not exhibit the same pressure dependence as the atom beam profiler and the MOT loading rate, it does not yield absolute information about the metastable flux.

A new atom flux monitoring will therefore have to be implemented in the future, for example by measuring the quench light of ^{40}Ar in the MOT. A different strategy would be to cure the deexcitations in the atom beam that occur on the way from the atom flux monitor to the MOT. If this can be achieved, the signal from the implemented atom flux monitoring would represent a sensitive and direct measure for the metastable argon flux in the MOT.

A systematic difference between atmospheric and groundwater measurements arises from the different foreline pressures of the argon gas in a sample container and in the commercial gas bottle. The manual pressure regulation for inserting argon gas from a sample container into the vacuum chamber introduces an additional systematic difference, which can technically be avoided by an automatic system. However, this systematic difference will vanish as soon as it can be measured in recycling mode.

Still, the present stability of the apparatus is sufficient for the dating of groundwater samples. Two water samples could be dated that were in agreement with the comparison results obtained by LLC in Bern. The ^{39}Ar concentration obtained for a groundwater sample with unknown ^{39}Ar concentration from the Hessian Ried proved to be in agreement with the complementary isotope data, which indicate a glacial origin of the groundwater.

By way of a summary and a conclusion to this thesis, all the measured ^{39}Ar concentrations for the groundwater samples as well as for the calibration samples are compiled in figure 6.4.

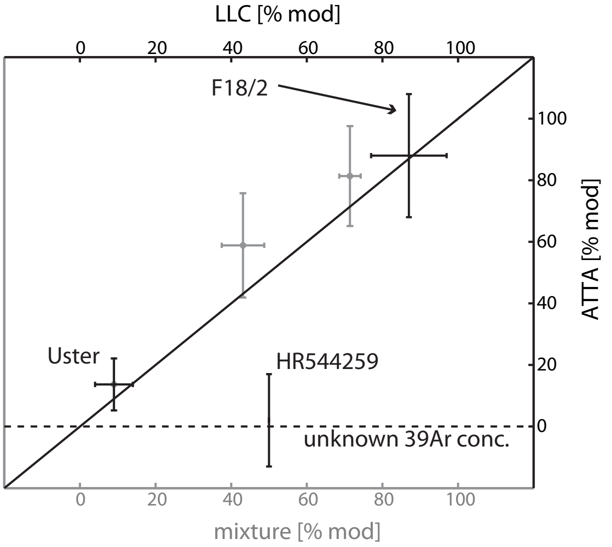

Figure 6.4: Compilation of the ^{39}Ar measurements performed with ^{39}Ar-ATTA. The data plotted in gray correspond to the calibration measurements with prepared samples, plotted with respect to the lower x-axis. The Uster sample and the F18/2 sample were measured in intercomparison with LLC, plotted with respect to the upper x-axis. The single off-diagonal point corresponds to the measurement of the Hessian Ried sample, which has an unknown ^{39}Ar concentration.

Bibliography

[1] World Water Assessment Programme. 3rd United Nations World Water Development Report: Water in a Changing World. Technical report, UNESCO, 2003.

[2] Werner Aeschbach-Hertig and Tom Gleeson. Regional strategies for the accelerating global problem of groundwater depletion. *nature geoscience*, 5:853, 2012.

[3] Roland Purtschert. Passing in review of radio-noble-gas measurements by low level counting at university of bern. Talk, given at the TANGR 2012 workshop.

[4] Joachim Welte. Atom Trap Trace Analysis of ^{39}Ar. Talk, given at the institute for environmental physics at the University of Heidelberg.

[5] Sven Ebser. Optimierung und Stabilisierung von ^{39}Ar-ATTA bis hin zur erstmaligen Anwendung auf die Datierung natürlicher Wasserproben. Master's thesis, University of Heidelberg, 2012.

[6] H.H. Loosli. A dating method with ^{39}Ar. *Earth and Planetary Science Letters*, 63(1):51 – 62, 1983.

[7] W. Jiang, K. Bailey, Z.-T. Lu, P. Mueller, T.P. O Connor, C.-F. Cheng, S.-M. Hu, R. Purtschert, N.C. Sturchio, Y.R. Sun, W.D. Williams, and G.-M. Yang. An atom counter for measuring ^{81}Kr and ^{85}Kr in environmental samples. *Geochimica et Cosmochimica Acta*, 91(0):1 – 6, 2012.

[8] W. Jiang, W. Williams, K. Bailey, A. M. Davis, S.-M. Hu, Z.-T. Lu, T. P. O'Connor, R. Purtschert, N. C. Sturchio, Y. R. Sun, and P. Mueller. ^{39}Ar Detection at the 10^{-16} Isotopic Abundance Level with Atom Trap Trace Analysis. *Phys. Rev. Lett.*, 106(10):103001, Mar 2011.

[9] Dr. Fritz Kahn. *Das Atom - endlich verständlich.* Albert Müller Verlag, 1949.

[10] J. Welte. *Atom Trap Trace Analysis of* ^{39}*Ar.* PhD thesis, Faculty of Physics and Astronomy, University of Heidelberg, www.matterwave.de, 2011.

[11] IAEA. Environmental isotopes in the hydrological cycle. *Water resources Programme*, 1, 2000.

[12] Hydroisotop gmbh. Isotope of the month - krypton85. *Company release*, may, 2013.

[13] H.H. Loosli and H. Oeschger. ^{39}Ar, ^{14}C and ^{85}Kr measurements in groundwater samples. *IAEA Vienna: Isotope Hydrology*, 2:931, 1978.

[14] H.H. Loosli, B.E. Lehmann, and W.M. Jr. Smethie. Noble gas radioisotopes: ^{37}Ar, ^{85}Kr, ^{39}Ar, ^{81}Kr. *Environmental Tracers in Subsurface Hydrology*, pages 379–396, 2000.

[15] K.Rozanski. ^{85}Kr in the atmosphere 1950-1977: a data review. *Environment International*, 2(3):139 – 143, 1979.

[16] W.G. Mook. Environmental isotopes in the hydrological cycle: Principles and applications. Technical report, Centre for Isotope Research, Groningen, 2001.

[17] Abdelhamid Guendouz and Jean-Luc Michelot. Chlorine-36 dating of deep groundwater from northern sahara. *Journal of Hydrology*, 328:572 – 580, 2006.

[18] David Elmore and Fred M. Phillips. Accelerator mass spectrometry for measurement of long-lived radioisotopes. *Science*, 236(4801):543–550, 1987.

[19] M. Geyh. An overview of ^{14}C analysis in the study of groundwater. *Radiocarbon*, 42:99–114, 2000.

[20] P. Collon, W. Kutschera, and Z.-T. Lu. Tracing noble gas radionuclides in the environment. *Annual Review of Nuclear and Particle Science*, 54(1):39–67, 2004.

[21] Lord Rayleigh and W. Ramsay. Argon, a new constituent of the atmosphere. *Proc. R. Soc. Lond.*, 57(6):265–287, 1894.

[22] Rene Rausch. www.periodensystem-online.de, 2013.

[23] M.Killen. Source and maintenance of the argon atmospheres of mercury and the moon. *Meteoritics & planetary science*, 37:1223–1231, 2002.

[24] Paul R. Mahaffy, Christopher R. Webster, Sushil K. Atreya, Heather Franz, Michael Wong, Pamela G. Conrad, Dan Harpold, John J. Jones, Laurie A. Leshin, Heidi Manning, Tobias Owen, Robert O. Pepin, Steven Squyres, Melissa Trainer, and MSL Science Team. Abundance and isotopic composition of gases in the martian atmosphere from the curiosity rover. *Science*, 341(6143):263–266, 2013.

[25] J. H. Hoffman, R. R. Hodges, M. B. Mcelroy, T. M. Donahue, and M. Kolpin. Composition and structure of the venus atmosphere: Results from pioneer venus. *Science*, 205(4401):49–52, 1979.

[26] Philippe Sarda, Thomas Staudacher, and Claude J. Allègre. ^{40}Ar^{36}Ar in MORB glasses: constraints on atmosphere and mantle evolution. *Earth and Planetary Science Letters*, 72(4):357 – 375, 1985.

[27] Bernard Marty and Franck Humbert. Nitrogen and argon isotopes in oceanic basalts. *Earth and Planetary Science Letters*, 152(1–4):101 – 112, 1997.

[28] R.F. Weiss. The solubility of nitrogen, oxygen and argon in water and seawater. *Deep Sea Research and Oceanographic Abstracts*, 17(4):721 – 735, 1970.

[29] A. R. Brosi, H. Zeldes, and B. H. Ketelle. ^{39}Ar beta-spectrum. *Phys. Rev.*, 79:902–902, Sep 1950.

[30] H.H. Loosli and H. Oeschger. Detection of ^{39}Ar in atmospheric argon. *Earth and Planetary Science Letters*, 5:191 – 198, 1968.

[31] H.Oeschger et al. ^{39}Ar-dating of groundwater. *Proc. Conf. Isotope Techniques in Groundwater Hydrology , Vienna, IAEA*, pages 179–90, 1974.

[32] D.-M. Mei, Z.-B. Yin, J. Spaans, M. Koppang, A. Hime, C. Keller, and V. M. Gehman. Prediction of underground argon content for dark matter experiments. *Phys. Rev. C*, 81:055802, May 2010.

[33] H.H. Loosli, B.E. Lehmann, and W. Balderer. ^{39}Ar, ^{37}Ar and ^{85}Kr isotopes in Stripa groundwaters. *Geochimica et Cosmochimica Acta*, 53(8):1825 – 1829, 1989.

[34] J.N. Andrews, T. Florkowski, B.E. Lehmann, and H.H. Loosli. Underground production of radionuclides in the Milk River aquifer, Alberta, Canada. *Applied Geochemistry*, 6(4):425 – 434, 1991.

[35] Reika Yokochi, Neil C. Sturchio, and Roland Purtschert. Determination of crustal fluid residence times using nucleogenic. *Geochimica et Cosmochimica Acta*, 88(0):19 – 26, 2012.

[36] R. Yokochi, N.C. Sturchio, R. Purtschert, W. Jiang, Z.-T. Lu, P. Mueller, G.-M. Yang, B.M. Kennedy, and Y. Kharaka. Noble gas radionuclides in yellowstone geothermal gas emissions: A reconnaissance. *Chemical Geology*, 339(0):43 – 51, 2013.

[37] E. Nolte, W. Rühm, H.H. Loosli, I. Tolstikhin, K. Kato, T.C. Huber, and S.D. Egbert. Measurements of fast neutrons in Hiroshima by use of ^{39}Ar. *Radiat. Environ. Biophys.*, 44:261, 2006.

[38] P. Benetti, F. Calaprice, E. Calligarich, M. Cambiaghi, F. Carbonara, F. Cavanna, A.G. Cocco, F. Di Pompeo, N. Ferrari, G. Fiorillo, C. Galbiati, L. Grandi, G. Mangano, C. Montanari, L. Pandola, A. Rappoldi, G.L. Raselli, M. Roncadelli, M. Rossella, C. Rubbia, R. Santorelli, A.M. Szelc, C. Vignoli, and Y. Zhao. Measurement of the specific activity of ^{39}Ar in natural argon. *Nuclear Instruments and Methods in Physics Research Section A: Accelerators, Spectrometers, Detectors and Associated Equipment*, 574(1):83 – 88, 2007.

[39] O. A. Schaeffer R. W. Stoenner and S. Katcoff. Half-lives of ^{37}Ar, ^{39}Ar, and ^{42}Ar. *Science*, 148:1325–1328, 1965.

[40] H. Oeschger W. Berner, P. Bucher and B. Stauffer. Analysis and interpretation of gas content and composition in natural ice. *Proceedings of the International Symposium on Isotopes and Impurities in Snow and Ice. Grenoble, 1975*, IAHS-Publication No. 118:p.272–84., 1977.

[41] Jingke Xu. *Study of Argon from Underground Sources for Direct Dark Matter Detection.* PhD thesis, Princeton University, 2013.

[42] H.H. Loosli, M. Möll, H. Oeschger, and U. Schotterer. Ten years low-level counting in the underground laboratory in Bern, Switzerland. *Nuclear Instruments and Methods in Physics Research Section B: Beam Interactions with Materials and Atoms*, 17(5-6):402 – 405, 1986.

[43] H Loosli, Martin Heimann, and Hans Oeschger. Low-level gas proportional counting in an underground laboratory. *Radiocarbon*, 22(2):461–469, 1980.

[44] Peter Schlosser, Gerhard Bönisch, Bernd Kromer, H.Hugo Loosli, Renedikt Bühler, Reinhold Bayer, Georges Bonani, and Klaus Peter Koltermann. Mid-1980s distribution of tritium, ^{3}He, ^{14}C and ^{39}Ar in the Greenland/Norwegian Seas and the Nansen Basin of the Arctic Ocean. *Progress in Oceanography*, 35(1):1 – 28, 1995.

[45] P. Schlosser, B. Kromer, R. Weppernig, H. H. Loosli, R. Bayer, G. Bonani, and M. Suter. The distribution of 14c and 39ar in the weddell sea. *Journal of Geophysical Research: Oceans*, 99(C5):10275–10287, 1994.

[46] W. Kutschera, M. Paul, I. Ahmad, T.A. Antaya, P.J. Billquist, B.G. Glagola, R. Harkewicz, M. Hellstrom, D.J. Morrissey, R.C. Pardo, K.E. Rehm, B.M. Sherrill, and M. Steiner. Long-lived noble gas radionuclides. *Nuclear Instruments and Methods in Physics Research Section B: Beam Interactions with Materials and Atoms*, 92(1-4):241 – 248, 1994.

[47] Michael Paul, Bruce G. Glagola, Walter Henning, Jörg G. Keller, Walter Kutschera, Zenhao Liu, Karl Ernst Rehm, Bernhard Schneck, and Rolf H. Siemssen. Heavy ion separation with a gas-filled magnetic spectrograph. *Nuclear Instruments and Methods in Physics Research Section A: Accelerators, Spectrometers, Detectors and Associated Equipment*, 277(2–3):418 – 430, 1989.

[48] Ph. Collon, M. Bichler, J. Caggiano, L. Dewayne Cecil, Y. El Masri, R. Golser, C. L. Jiang, A. Heinz, D. Henderson, W. Kutschera, B. E. Lehmann, P. Leleux, H. H. Loosli, R. C. Pardo, M. Paul, K. E. Rehm, P. Schlosser, R. H. Scott, W. M. Smethie, and R. Vondrasek. Development of an AMS method to study oceanic circulation characteristics using cosmogenic ^{39}Ar. *Nuclear Instruments and Methods in Physics Research Section B: Beam Interactions with Materials and*

Atoms, 223:428 – 434, 2004. Proceedings of the Ninth International Conference on Accelerator Mass Spectrometry.

[49] P. Collon, M. Bowers, F. Calaprice, C. Galbiati, D. Henderson, T. Hohman, C.L. Jiang, W. Kutschera, H.Y. Lee, B. Loer, R.C. Pardo, M. Paul, E. Rehm, D. Robertson, C. Schmitt, R. Scott, and R. Vondrasek. Reducing potassium contamination for AMS detection of ^{39}Ar with an electron-cyclotron-resonance ion source. *Nuclear Instruments and Methods in Physics Research Section B: Beam Interactions with Materials and Atoms*, 283(0):77 – 83, 2012.

[50] P. Benetti, R. Acciarri, F. Adamo, B. Baibussinov, M. Baldo-Ceolin, M. Belluco, F. Calaprice, E. Calligarich, M. Cambiaghi, F. Carbonara, F. Cavanna, S. Centro, A.G. Cocco, F. Di Pompeo, N. Ferrari, G. Fiorillo, C. Galbiati, V. Gallo, L. Grandi, A. Ianni, G. Mangano, G. Meng, C. Montanari, O. Palamara, L. Pandola, F. Pietropaolo, G.L. Raselli, M. Rossella, C. Rubbia, A.M. Szelc, S. Ventura, and C. Vignoli. First results from a dark matter search with liquid argon at 87K in the gran sasso underground laboratory. *Astroparticle Physics*, 28(6):495 – 507, 2008.

[51] J. Xu, F. Calaprice, C. Galbiati, A. Goretti, G. Guray, T. Hohman, D. Holtz, A. Ianni, M. Laubenstein, B. Loer, C. Love, C. J. Martoff, D. Montanari, S. Mukhopadhyay, A. Nelson, S. D. Rountree, R. B. Vogelaar, and A. Wright. A Study of the Residual 39Ar Content in Argon from Underground Sources. *ArXiv e-prints*, April 2012.

[52] D. Acosta-Kane et al. Discovery of underground argon with low level of radioactive ^{39}Ar and possible applications to WIMP dark matter detectors. *Nuclear Instruments and Methods in Physics Research A*, 587:46, 2008.

[53] H. O. Back, F. Calaprice, C. Condon, E. de Haas, R. Ford, C. Galbiati, et al. First Large Scale Production of Low Radioactivity Argon From Underground Sources. *arXiv*, 2012.

[54] H. O. Back, T. Alexander, A. Alton, C. Condon, E. de Haas, C. Galbiati, et al. First Commissioning of a Cryogenic Distillation Column for Low Radioactivity Underground Argon. *arXiv*, 2012.

[55] C. Y. Chen, Y. M. Li, K. Bailey, T. P. O'Connor, L. Young, and Z.-T. Lu. Ultrasensitive Isotope Trace Analyses with a Magneto-Optical Trap. *Science*, 286(5442):1139–1141, 1999.

[56] N. C. Sturchio, X. Du, R. Purtschert, B.E. Lehmann, M. Sultan, L. J. Patterson, Z. T. Lu, P. Mueller, T. Bigler, K. Bailey, T. P. O'Connor, L. Young, R. Lorenzo, R. Becker, Z. El Alfy, B. El Kaliouby, Y. Dawood, and A. M. A. Abdallah. One million year old groundwater in the Sahara revealed by ^{81}Kr and ^{36}Cl. *Geophys. Res. Lett.*, 31:L05503, 2004.

[57] S. Hoekstra, A. K. Mollema, R. Morgenstern, H. W. Wilschut, and R. Hoekstra. Single-atom detection of calcium isotopes by atom-trap trace analysis. *Phys. Rev. A*, 71(2):023409, Feb 2005.

[58] I. D. Moore, K. Bailey, J. Greene, Z.-T. Lu, P. Müller, T. P. O'Connor, Ch. Geppert, K. D. A. Wendt, and L. Young. Counting Individual ^{41}Ca Atoms with a Magneto-Optical Trap. *Phys. Rev. Lett.*, 92(15):153002, 2004.

[59] Martin B. Kalinowski, Heiner Daerr, and Markus Kohler. Measurements of ^{85}Kr to detect clandestine plutonium production. *INESAP Information Bulletin*, 27:9–12, 2006.

[60] E. Aprile, T. Yoon, A. Loose, L. W. Goetzke, and T. Zelevinsky. An atom trap trace analysis system for measuring krypton contamination in xenon dark matter detectors. *Review of Scientific Instruments*, 84(9):–, 2013.

[61] G. M. Yang. Analysis of ^{85}Kr: a comparison at the 10^{-14} level using micro-liter samples. *Scientific reports*, 3:1596, 2013.

[62] Giulio Racah. On a new type of vector coupling in complex spectra. *Phys. Rev.*, 61:537–537, Apr 1942.

[63] F. Ritterbusch. Realization of a collimated beam of metastable atoms for ATTA of ^{39}Ar. Master's thesis, Faculty of Physics and Astronomy, University of Heidelberg, 2009.

[64] J. Welte, I. Steinke, M. Henrich, F. Ritterbusch, M. K. Oberthaler, W. Aeschbach-Hertig, W. H. Schwarz, and M. Trieloff. Hyperfine spectroscopy of the $1s_5 - 2p_9$ transition of ^{39}Ar. *Review of Scientific Instruments*, 80(11):113109, 2009.

[65] W. Williams, Z.-T. Lu, K. Rudinger, C.-Y. Xu, R. Yokochi, and P. Müller. Spectroscopic study of the cycling transition 4s$[3/2]_2$–4p$[5/2]_3$ at 811.8 nm in ^{39}Ar: Hyperfine structure and isotope shift. *Phys. Rev. A*, 83:012512, 2011.

[66] H. J. Metcalf and P. van der Straten. *Laser cooling and trapping.* Springer, New York ; Berlin ; Heidelberg [u.a.], 1999.

[67] D. A. Steck. Rubidium 87 D Line Data. Technical report, Oregon Center for Optics and Department of Physics, University of Oregon, 2001.

[68] Rodney Loudon. *The quantum theory of light.* Oxford Univ. Press, Oxford [u.a.], 2008.

[69] I. Sobel'man. *Introduction to the theory of atomic spectra.* Number 40 in International series of monographs in natural philosophy ; 40 ; International series of monographs in natural philosophy. Pergamon Press, Oxford ; Braunschweig [u.a.], 1. ed. edition, 1972.

[70] H Abu Safia, J P Grandin, and X Husson. g factor measurements for Ne, Ar and Kr. *Journal of Physics B: Atomic and Molecular Physics*, 14(18):3363, 1981.

[71] J. R. Brandenberger. Landé g_J values in atomic argon: A measurement of the ratio $g_J(2p_9)/g_J(1s_5)$ by saturation spectroscopy. *Phys. Rev. A*, 60:1336–1340, Aug 1999.

[72] H. Kopfermann. *Kernmomente*. Akadem. Verl.-Ges., Frankfurt am Main, 1956.

[73] A. Klein, B.A. Brown, U. Georg, M. Keim, E Lievens, R. Neugart, M. Neuroth, R.E. Silverans, L. Vermeeren, and the ISOLDE Collaboration. Moments and mean square charge radii of short-lived argon isotopes. *Nuclear Physics A*, 607(7):1–22, 1996.

[74] C. J. Foot. *Atomic physics*. Number 7 : Atomic, optical, and laser physics in Oxford master series in physics ; 7 : Atomic, optical, and laser physics ; Oxford master series in physics. Oxford University Press, Oxford [u.a.], 1. publ. edition, 2005.

[75] C. Kaup. Single-Atom Detection of ^{39}Ar. Master's thesis, Faculty of Physics and Astronomy, University of Heidelberg, 2011.

[76] M. Henrich. Design and Realization of a Laser System for ATTA of ^{39}Ar. Master's thesis, Faculty of Physics and Astronomy, University of Heidelberg, 2010.

[77] N A Surplice and R J D'Arcy. Reduction in the work function of stainless steel by electric fields. *Journal of Physics F: Metal Physics*, 2(1):L8, 1972.

[78] Hamamatsu Photonics, editor. *Photomultiplier Tubes - Basics and Application*. Hamamatsu, 2007.

[79] B.C. Jacquot, Steve P. Monacos, Michael E. Hoenk, Frank Greer, T.J. Jones, and S. Nikzad. A system and methodologies for absolute quantum efficiency measurements from the vacuum ultraviolet through the near infrared. *Review of Scientific Instruments*, 82(4):043102–043102–10, 2011.

[80] S. Schohl, D. Klar, T. Kraft, H. A. J. Meijer, M.-W. Ruf, U. Schmitz, S. J. Smith, and H. Hotop. Absolute detection of metastable rare gas atoms by a cw laser photoionization method. *Zeitschrift fur Physik D Atoms, Molecules and Clusters*, 21:25 – 39, Jan-03-1991 1991.

[81] J. Weiner, V.S. Bagnato, S. Zilio, and P.S. Julienne. Experiments and theory in cold and ultracold collisions. *Reviews of Modern Physics*, 71(1):1–85, 1999.

[82] A. Bogaerts and R. Gijbels. Modeling of metastable argon atoms in a direct-current glow discharge. *Physical Review A*, 52:3743, 1995.

[83] Z. Feng. Implementierung einer Atomflussüberwachung für ^{39}Ar ATTA. Bachelor's thesis, Faculty of Physics and Astronomy, University of Heidelberg, 2012, www.matterwave.de, 2012.

[84] M. D. Hoogerland, J. P. J. Driessen, E. J. D. Vrcdenbregt, H. J. L. Megens, M. P. Schuwer, H. C. W. Beijerinck, and K. A. H. van Leeuwen. Bright thermal atomic beams by laser cooling: A 1400-fold gain in beam flux. *Applied Physics B: Lasers and Optics*, Volume 62(4):323–327, 1996.

[85] A. Aspect, N. Vansteenkiste, and R. Kaiser. Preparation of a pure intense beam of metastable helium by laser cooling. *Chemical Physics*, 145:307–315, 1990.

[86] F. Ruschewitz, D. Bettermann, J. L. Peng, and W. Ertmer. Statistical investigations on single trapped neutral atoms. *EPL (Europhysics Letters)*, 34(9):651, 1996.

[87] K. Rudinger, Z.-T. Lu, and P. Mueller. The role of carrier gases in the production of metastable argon atoms in a rf discharge. *Review of Scientific Instruments*, 80(3):036105, 2009.

[88] Urs Beyerle, Roland Purtschert, Werner Aeschbach-Hertig, Dieter M. Imboden, Heinz H. Loosli, Rainer Wieler, and Rolf Kipfer. Climate and groundwater recharge during the last glaciation in an ice-covered region. *Science*, 282(5389):731–734, 1998.

[89] Thomas Reichelt. *Groundwater Degassing and Separation of Argon from Air for ^{39}Ar Dating with ATTA*. PhD thesis, University of Heidelberg, 2013.

[90] Arne Kersting. A new method of krypton purification for groundwater dating with atom trap trace analysis. Master's thesis, Universtiy of Heidelberg, 2013.

[91] A. M. Negriiko V. S. Voitsekhovich, M. V. Danileiko and V. I. Romanenko. Stimulated light pressure on atoms in counterpropagating amplitude-modulated waves. *Zh. Eksp. Teor. Fiz.*, 99:393–410, 1991.

[92] J. Söding, R. Grimm, Yu. B. Ovchinnikov, Ph. Bouyer, and Ch. Salomon. Short-distance atomic beam deceleration with a stimulated light force. *Phys. Rev. Lett.*, 78:1420–1423, Feb 1997.

[93] M. Cashen and H. Metcalf. Optical forces on atoms in nonmonochromatic light. *J. Opt. Soc. Am. B*, 20(5):915–924, May 2003.

[94] Leonid Yatsenko and Harold Metcalf. Dressed-atom description of the bichromatic force. *Phys. Rev. A*, 70:063402, Dec 2004.

[95] A. Mil. Realization of an amplified optical beating for bichromatic cooling of metastable argon. Bachelor's thesis, Faculty of Physics and Astronomy, University of Heidelberg, 2013, www.matterwave.de, 2013.

Acknowledgments

Many people contributed in one or the other way to the presented PhD-thesis.
I want to thank

- Markus Oberthaler for supervising this PhD-thesis, for giving me the opportunity to continue with the ATTA experiment in his group after my diploma thesis and for initiating this wonderful project as well as having the perseverance to keep it going
- Werner Aeschbach-Hertig for initiating the project and very reliably caring for the environmental physics part, for plenty of hydrologic input and for proofreading parts of this thesis
- Norbert Frank for kindly agreeing to grade this thesis, which hopefully broadens the ^{39}Ar-ATTA community at the institute for environmental physics
- Special thanks go to my PhD collegues, that I have spent uncountable hours in the lab with. In chronological order
    - Joachim Welte for splendid and productive three years on the ATTA project together with him, starting off from an empty lab. The results presented here would certainly not have been possible without his untiring efforts in setting up the experiment. Moreover, I want to thank for finding the time to proofread this thesis and being steadily available for issues related to ATTA
    - Sven Ebser for so far two very pleasant and fruitful years on the ATTA experiment, including enjoyable field trips to Zurich and Grundremmingen. Of course the results presented here are the product of an extensive team effort und were only possible as such. I am moreover grateful for finding subtle errors in my thesis upon proofreading it and extra support during the last weeks
- Zhongyi Feng for support with some of the shown measurements and preventing my eyes from being destroyed by a bad computer monitor setting
- All former ATTA team members for contributing to the experiment and to a good spirit in the ATTA lab, namely Isabelle Steinke, Matthias Henrich, Christoph Kaup, Gong Cheng, Alexander Mil and Max Prüfer
- Thomas Reichelt and Arne Kersting for degassing tons of water and extracting many liters of argon for the ATTA project. Moreover, for a very pleasant working together and the fun of sampling groundwater

- Philippe Bräunig for good neighborship, argonautic solidarity and always being ready to lend a hand
- David B. Hume for taking the time to proofread the single atom chapter and being always open to questions
- Jiří Tomkovič for computer and matlab support as well as always taking the time to help
- Arno Trautmann for excellent LaTeX support
- All other matterwavers for still waving matters and being a very helpful team
- The mechanical workshop, especially Werner Lamade for plenty design support and coordination, Julia Bing and Sascha Braun for the collimator project, Siegfried Spiegel for support on the vacuum pumps and many other mechanical problems, Helmut Maier especially for the noise insulation boxes and Christian Herdt for plenty of welding work
- Jürgen Schölles for electronic as well as physiotherapeutic support and Alexander Leonhardt for not getting tired of repairing our power supplies
- Dagmar Hufnagel and Christiane Jäger for excellent and very enlivening organisational support
- Roland Purtschert for providing us many groundwater samples, especially the crucial ^{39}Ar-free samples, as well as for the intercomparison measurements
- Hydroisotop GmbH for being very cooperative during our search for ^{39}Ar-free samples
- The *Studienstiftung des deutschen Volkes* for uncomplicated financial support, which allowed me to concentrate on the PhD-thesis while not having to give up all non-academic activities
- Jon Smale for linguistic and orthographic proofreading of this thesis
- Erika and Martin Schindler for supporting me throughout my whole life
- Daniel Ritterbusch for steady brotherly culinary support
- Karl Ritterbusch for supporting me as long as he could